GNSS data processing strategies and antenna phase-center calibration techniques

Evaluating different calibration methods and their impact on atmospheric monitoring and climate research

Master's thesis in Physics and Communication Engineering

FRIDA JOHANSSON

MEAAD ABDALLA

DEPARTMENT OF SPACE, EARTH AND ENVIRONMENT

CHALMERS UNIVERSITY OF TECHNOLOGY
Gothenburg, Sweden 2022
www.chalmers.se

Master's thesis 2022

GNSS data processing strategies and antenna phase-center calibration techniques

Evaluating different calibration methods and their impacts on atmospheric monitoring and climate research

FRIDA JOHANSSON

MEAAD ABDALLA

Department of Space, Earth and Environment
Division of Geoscience and Remote Sensing
Space Geodesy and Geodynamics
Chalmers University of Technology
Gothenburg, Sweden 2022

GNSS data processing strategies and antenna phase-center calibration techniques
Evaluating different calibration methods and their impacts on atmospheric monitoring and climate research
FRIDA JOHANSSON
MEAAD ABDALLA

Supervisor: Jan Johansson, Department of Space, Earth and Environment
Examiner: Jan Johansson, Department of Space, Earth and Environment

Master's Thesis 2022
Department of Space, Earth and Environment
Division of Geoscience and Remote Sensing
Space Geodesy and Geodynamics
Chalmers University of Technology
SE-412 96 Gothenburg
Telephone +46 31 772 1000

Cover: ONSA, the main international GNSS station at Onsala Space Observatory.

Typeset in LaTeX
Printed by Chalmers Reproservice
Gothenburg, Sweden 2022

GNSS data processing strategies and antenna phase-center calibration techniques
Evaluating different calibration methods and their impacts on atmospheric monitoring and climate research

FRIDA JOHANSSON
MEAAD ABDALLA
Department of Space, Earth and Environment
Chalmers University of Technology

Abstract

GNSS-related applications have increased dramatically in recent decades, raising the need for more precise results. Thus, enhancements for GNSS's different segments are vital to achieving higher accuracy. The receiver-related biases are prominent errors that affect GNSS measurements and results, particularly errors associated with the antennas and their phase-center. In addition, identifying the correct antenna measuring point is difficult since phase-centers are electrical characteristics that change with frequency, elevation, and azimuth angles. Therefore, antenna calibration is indispensable to mitigate phase-center-related errors. Multiple approaches are currently employed to calibrate GNSS antennas, specifically model-specific and antenna-specific. Although these techniques have considerably contributed to GNSS accuracy, they face limitations related to the respective site specifications.

Using the internationally available (ONSA & ONS1) and regional (OTT 1 through 6) GNSS stations at the Onsala Space Observatory (OSO), the impact of different calibration methods on GNSS accuracy has been investigated. Station-specific corrections were also considered in the study. Various constraints and cut-off elevation angles were examined and modified to reduce the influence of other error sources. Data from 2019 -2021 for GPS, Galileo, and GLONASS constellations, were collected and processed using the GipsyX v.1.7 software, which uses the Precise Point Positioning technique. During the processing, a period of 30 hours, instead of the typical 24 hours, of observations was used to guarantee higher stability for the Kalman filter. In addition to the coordinate estimations, the analysis included the tropospheric zenith delay (ZTD) and tropospheric gradients. The estimated delay parameters were verified and compared with estimations from other measurement techniques such as Very Long Baseline Interferometry (VLBI) and water vapor radiometer (WVR). Temporary stations were established at four accurate geodetic checkpoints from March-May 2022 to be used to derive a station-specific calibration matrix for the international stations at OSO. It was found that supported by other measurement techniques, the examined constraints and elevation cut-off values impact the accuracy of GNSS results. Model-specific calibration values were compared with VLBI & WVR results. However, minor differences were detected when comparing model and antenna-specific calibration methods.

Keywords: GNSS, Zenith Total Delay, Tropospheric Gradients, Antenna Phase-Center, GipsyX , GPS, Precise Point Positioning, Onsala Space Observatory

Acknowledgements

We thank our supervisor Jan Johansson for his assistance and guidance throughout our work and for feedback that greatly improved this thesis. We would also like to thank T. Ning for his technical help with implementing the change of matrices within GipsyX for part of our research.

We would furthermore like to show our gratitude to the Onsala Space Observatory and the people who work there for not only welcoming us and helping us throughout our field studies at the observatory but also for sharing their knowledge and providing us with data making this project possible.

Frida Johansson & Meaad Abdalla, Gothenburg, June 2022

List of Acronyms

Below is the list of acronyms that have been used throughout this thesis listed in alphabetical order:

AFS	Atomic Frequency Standards
ARP	Antenna Reference Point
AUT	Antenna Under Test
CATR	Compact Antenna Test Ranges
CDMA	Code Division Multiple Access
CRF	Celestial Reference Frame
DOP	Dilution Of Precision
DSP	Digital Signal Processor
EM	Electromagnetic
EOP	Earth Orientation Parameter
FDMA	Frequency Division Multiple Access
GEO	Geostationary Earth Orbit
GLONASS	GLObal NAvigation Satellite System
GNSS	Global Navigation Satellite Systems
GPS	Global Positioning System
IF	Intermediate Frequency
IGS	The International GNSS Service for Geodynamics
IRNSS	Indian Regional Navigational Satellite System
ITU	The International Telecommunication Union
JPL	Jet Propulsion Laboratory
LEO	Low Earth Orbit
LHCP	Left Hand Circularly Polarized
LNA	Low Noise Amplifier
LSE	Least Squares Estimation
MEO	Medium Earth Orbit
NAVSTAR	NAVigation System with Timing And Ranging
NF – FF	Near-Field Far-Field
NGS	National Geodetic Survey
NNSS	Navy Navigation Satellite System
NWP	Numerical Weather Prediction
OSO	Onsala Space Observatory
PCO	Phase-Center Offset
PCV	Phase-Center Variation
PPP	Precise Point Positioning
PRN	Pseudo Random Noise

QPSK	Quadrature Phase Shift Keying
QZSS	Quasi-Zenith Satellite System
RHCP	Right Hand Circularly Polarized
RINEX	Receiver-Independent Exchange Format
RMS	Root Mean Square
RO	Radio Occultation
SWEPOS	The Swedish Permanent Network of GNSS Stations
TRF	Terrestrial Reference Frame
VLBI	Very Long Baseline Interferometry
WVR	Water Vapor Radiometer
ZHD	Zenith Hydrostatic Delay
ZTD	Zenith Tropospheric Delay
ZWD	Zenith Wet Delay

Nomenclature

Below is the nomenclature of indices, parameters, and variables that have been used throughout this thesis.

Indices

k	Indices for the tracking receiver
s	Index for the tracked satellite
o	Index for the initial guess
i	Index for the time step

Parameters

e	eccentricity
a	Semi-major axis
ω	Argument of perigee
Ω	Right Ascension of ascending node
c	The speed of light in a vacuum
ΔX	Correction term for variable X
λ_o	The nominal wavelength
f_o	The fundamental frequency
φ_o	The nominal phase
ν	Propagation velocity
epoch	Time of perigee passing

Variables

LI	GPS frequencies (I = 1,2, or 5)
GI	GLONASS frequencies (I = 1 or 2)
n	Number of stage registers
P_k^s	Code pseudo-range between receiver k and satellite s
t_k	Clock time for receiver k

t^s	Transmitting time for satellite s
ρ_k^s	The true geometric range for satellite s tracked by receiver k
τ_k	Synchronized (true) time for receiver k
τ^s	Synchronized (true) time for satellite s
I_k^s	Ionospheric delay for receiver k and satellite s
T_k^s	Tropospheric delay for receiver k and satellite s
x^s, y^s, z^s	The (x, y, and z) coordinates for satellite s
x_k, y_k, z_k	The (x,y,and z) coordinates for receiver k
$P_{Computed}$ or C	The computed initial guess
$P_{Observed}$ or O	The observed ionospheric-free combination
φ_B	Carrier beat phase
φ^s	Signal phase transmitted by satellite s
φ_k	Signal phase generated by receiver k
Φ	Carrier phase measurement
N_k^s	Phase ambiguity parameter for satellite s tracked by receiver k
f_{L1}	GPS frequency of the first carrier
f_{L2}	GPS frequency of the second carrier
L_k^s	Carrier phase pseudo-range between receiver k and satellite s
B_k^s	Carrier phase bias between receiver k and satellite s
$L3$ or Lc	Ionospheric-free carrier phase observables
$P3$ or Pc	Ionospheric-free code observables
n	Reflective index
D, E, F1, and F2	Ionosphere layers
p	Pressure in hectopascal
h	height in meter
ϕ	Latitude

Contents

List of Figures

List of Tables

1
Introduction

Global Navigation satellite systems (GNSS), is the collective name for systems utilizing artificial satellites as positioning, timekeeping, and navigation tools. Currently, the available GNSS constellations around the world are GPS (USA), Galileo (EU), GLONASS (Russia), COMPASS/Beidou (China), QZSS (Japan), and Navic/IRNSS (India). In this project, GPS, Galileo, and GLONASS have been used. The reason is that by combining multiple systems, availability, coverage, and the obtained results are significantly improved.

GNSS supports a multitude of applications. Although the initial purposes of GPS were military applications, when the development started in 1973 by the US department of defense, GNSS today is a valuable tool for many fields; civil, scientific, industrial, and construction, to name a few. Some specific areas of application are modern smart devices, making portable navigation accessible for the everyday consumer. In addition, geodesy and geodynamics utilize GNSS extensively in their research. Studies of the shape of Earth and its change with time provides greater understanding of our planet, however, it can also be detrimental in predicting disasters such as earthquakes and volcanic eruptions. GNSS can moreover be used in meteorology to accurately monitor climate change and perform numerical weather predictions.

The International GNSS Service for Geodynamics (IGS), supported by a network of GNSS stations available globally, offers constant access to high precision data, making these studies possible. Furthermore, many countries have established local networks of GNSS stations to support different applications. For example, in Sweden, controlled by Lantmäteriet, the Swedish permanent network of GNSS stations (SWEPOS) contains over 500 stations distributed around the country. They aim to continuously improve the operations of existing and new GNSS stations throughout Sweden.

GNSS measurements are susceptible to many error sources. Therefore, it is crucial to account for these biases to ensure accurate results. One example is hardware-related effects caused by antennas, receivers, and other equipment. In addition, the local environment around GNSS stations will affect the received electromagnetic signals and hence the measurements. Causes for such errors include signal blockage by surrounding buildings and foliage as well as multi-path effects. Antennas are one of the main elements that require a proper phase-center calibration. The direct influence of signal blockage and multi-path results in poor accuracy of measurements and estimations.

The main purpose of this project is to evaluate GNSS antenna-dependent and station-dependent calibration values and assess different antenna phase-center corrections, namely, model-specific, antenna-specific, and site-specific. The processing will include the zenith tropospheric delay (ZTD) and tropospheric gradients. The estimated wet tropospheric delay (ZWD) parameters will be verified and compared with estimations from different measurement techniques such as the Very Long Baseline Interferometry (VLBI) and Water Vapor Radiometer (WVR). Thus, identify the optimal calibration and antenna phase-center correction method.

It should be noted that, similar to GNSS, neither WVR nor VLBI provide perfect results, and both contain many error sources. The WVR is particularly sensitive to rain. The resulting effects are difficult to calculate, making any results obtained during rainfall unreliable. Likewise, both GNSS and VLBI measure the total zenith delay, a sum of the wet and hydrostatic delay. In this report the zenith wet delay is of most interest, necessitating the integration of pressure data to estimate then eliminate the zenith hydrostatic delay (ZHD). Consequently, another source of error is introduced. Neither GNSS, WVR or VLBI provide the definite truth, but their results will be compared with the intention of improving GNSS calibrations and results.

The project aims to eventually arrive at station-specific calibrations, ensuring the best possible results for the stations at Onsala Space Observatory. Note that due to lack of time these final station-specific calibrations were not completed. Two of these stations, ONSA (also known as ONS0) and ONS1 are IGS stations. The six remaining stations, named OTT 1 through 6, are SWEPOS local stations at the observatory. Data will be collected from these stations and processed using GipsyX version 1.7 and the Precise Point Positioning (PPP) technique.

Experimenting with various gradient constraints in the GipsyX software, different elevation cut-off angles, and antenna calibration matrices, the objective is to establish the optimal values to achieve accurate results. The principal part of the project will be to investigate the significance of employing different calibration methods, namely, the model-specific calibration relying on the predetermined benchmarks for the GNSS antennas, the choke-ring antenna, and the antenna-specific calibration using the calculated phase-center values for the particular antenna, an antenna matrix. Furthermore, the projects last and most important method is station-specific calibration. As opposed to the antenna-specific, this method uses values that are evaluated for the individual station including mount, altitude, and the surrounding environment. To further evaluate, the proper station-specific calibration, measurements are carried out at OSO during the processing and calibration phase of the project utilizing a temporary network of four accurately measured geodetic checkpoints.

2
Theory

For a long time, accurate positioning was confined to highly skilled navigators owning expensive navigation systems [1]. However, GNSS innovation has allowed access to precise positioning for many users [1].

GNSS are satellite-based systems that send globally available, continuous signals to provide navigation information on Earth and near space [2]. The navigation data determine an objects position, velocity, orientation, and time [1]. At least four navigation satellites communicate with distinctive receivers [2]. GNSS's unique software then processes the received signals to provide precise navigation characteristics [1].

Initially, the U.S. Military developed the Navy Navigation Satellite System (NNSS) to provide military services [1]. Even though civilians were authorized to use the system later, NNSS suffered significant weaknesses [3]. However, with the evolution of space-based atomic clocks [2], the U.S. Department of Defense developed the navigation system with timing and ranging (NAVSTAR) Global Positioning System (GPS) that overcame the shortcomings of its predecessor system [3]. Furthermore, GNSS attributes, techniques, and software advancement facilitated other military, commercial, and scientific applications [4] beyond their originally envisioned intention [1].

The basic idea behind global positioning is to determine the unknown, fixed or moving point, position, i.e., latitude, longitude, and height, using distances to three comprehended coordinates. This process is known as trilateration [5]. Satellite-based positioning, however, requires an additional known point to account for clock bias [4].

GNSS receivers compare the received signals with their locally generated replica to estimate the different unknowns [4]. It is worth noting that ranges to satellites are different from the geometric distances due to the time offset between the satellites and the receivers [3]. Therefore, these ranges are known as pseudo-ranges [2]. Pseudo-ranges represent the geometric ranges plus range corrections [5]. The following subsections introduce GNSS in more detail.

2.1 GNSS Segments

GNSS has a well defined structure consisting of three segments to offer continuous global positioning services [4]. Mainly space segment, control segment, and user segment [3].

2.1.1 Space Segment

The primary function of the space segment is to transmit continuous signals toward the Earth [5]. Therefore, satellite constellation design is connected to service availability, coverage, satellite geometry, launching, maintenance, and replenishment costs [3].

For instance, considering launching costs, coverage, transmitted power, and attenuation, the Medium Earth Orbit (MEO) was selected for GNSS satellites [4]. Another essential factor is the number of satellites in a constellation and orbital plane. Each constellation must have enough satellites such that at least four satellites are simultaneously visible at each location [3].

Nowadays, four international GNSS constellations and several regional systems are available [2]. However, the most widely known operational GNSS is GPS, developed by the U.S. Department of Defense to offer global coverage [1]. Another mature international system is the Russian system known as the GLObal NAvigation Satellite System, GLONASS [2]. Furthermore, China and the European Union proceed with their GNSS systems, Beidou, and Galileo [1]. These Global coverage constellations utilize the same principle with minor differences.

On the other hand, some countries like India and Japan have developed regional systems, i.e., the Indian Regional Navigational Satellite System (IRNSS) and the Quasi-Zenith Satellite System (QZSS), to support and augment the existing space-based navigation systems [4].

2.1.2 Control Segment

The control segment, alternatively the ground segment, is essential for GNSS operation [3]. Several monitoring stations, i.e., tracking networks and telemetry tele-command antennas spreading worldwide, support the central control hub to coordinate, track, monitor, and connect GNSS satellites [4]. The primary functions of this segment are signal tracking, estimating the clock parameters, maintaining orbital elements, evaluating satellite conditions, and satellite geometry optimization [5], among others.

The American systems (GPS) master control center is based in Colorado Springs and has several monitoring stations around the globe [5]. Furthermore, all parts of the control segment of GLONASS, the Russian system, are located within the Russian Federation's borders, where the primary control unit is in Moscow [4].

2.1.3 User Segment

The user segment comprises GNSS hardware, receivers, and software [5]. The prominent role of the user segment is to receive and process the signals and serve navigation, positioning, and timing applications [4]. There are currently many types of GNSS receivers varying in their ability to receive different observables and pseudo-ranges and track specific frequencies [3].

In addition to the aforementioned receiver-type users, the International GNSS Service for Geodynamics (IGS) developed a network of stations , forming another type of users, to provide more precise satellite information, particularly satellite orbits and clock data [4].

2.2 Satellites Orbits and clocks

Artificial satellite motion is governed by Kepler's laws of planetary motions and is supported by Newton's gravitational theory [6]. Therefore, orbits design ensures quality performance in accuracy, availability, and coverage [1]. Six elements, namely the eccentricity (e), semi-major axis (a), inclination (i), the time of perigee passing (epoch), Argument of perigee (ω), and Right Ascension of ascending node (Ω), known as the Keplerian set, define satellite orbits [5]. Each element holds essential information about the orbit shape and satellite position in orbit, orientation, or position related to Earth [6].

All GNSS utilizes MEO satellites about 20,000 - 30,000 km above the Earth's surface [4], with some exceptions. For instance, in addition to the MEO satellites, the Chinese system, Beidou, is supported by five geostationary satellites (GEO) [4]. According to Kepler's first law, the orbits have an elliptical shape [6]. However, in the original design (GPS), due to the small eccentricity value ($e = 0.02$) for the orbital ellipse, GPS orbits are almost circular [5]. More details regarding the orbital elements for different GNSS constellations are summarized in table 2.1.

Table 2.1: Brief summary of the orbital elements for the international GNSS systems [2,3,5]

System (Constellation)	Number of Satellites	Orbits	Number of Orbital planes	Inclination	Channel access
GPS	24 operational (2020)	MEO (20,200km)	6	55	CDMA
GLONASS	24 operational (2020)	MEO (19,140 km)	3	64.8	FDMA
GALILEO	30 when fully deployed	MEO (23,222 km)	3	55	CDMA
BEIDOU	35 when fully deployed	GEO and MEO (21,550 km)	6	55	CDMA

The sophisticated orbital design guarantees the availability of at least four satellites, with suitable geometry, anytime and everywhere [5]. Apart from the orbital elements, the number of satellites in an orbital plane is also important. [3].

Although the keplerian parameters provide a detailed description, various phenomena like solar radiation, non-homogeneous mass distribution of the Earth, and other celestial bodies cause variations in these parameters leading to perturbation of the satellite's motion [6]. Therefore, the control segment continuously tracks and monitors the satellites and controls the maintenance maneuvers to adjust for any changes [3].

In addition to the basic subsystems, all GNSS are equipped with atomic clocks [4]. Based on the Atomic Frequency Standards (AFS), their primary role is precisely controlling the system's signals and frequencies [3].

Before launching, the oscillator is set with an offset of about 39,000 nanoseconds/day to compensate for potential and average velocity changes after the launching process [7]. Different atomic clocks vary in terms of stability. On the one hand, quartz and rubidium and hydrogen maser are suitable for short-term performance, whereas cesium offer better long-term stability [4]. It is worth noting that clock stability is vital for the accuracy of GNSS measurements and results [3]. It is equally essential to acquire error-free satellite coordinates, orbital elements, and clock parameters [7].

2.3 GNSS Signals and Frequencies

GNSS constellations transmit weak navigation signals, utilizing the spread spectrum concept, i.e., the occupied bandwidth is larger than the data rate, making it ideal for hiding the signals in a background noise [8].

GNSS signals must reach an infinite number of users without impairment, e.g., interference with other satellites or systems [3]. However, since all satellites in a constellation share the same frequency, a unique binary sequence that behaves like a random noise called the Pseudo Random Noise (PRN) number is used to identify each satellite and make it recognizable to the receivers [4].

Another significant contribution of the onboard atomic clocks is to drive the transmitted signal [5]. GNSS signal structure is identical for all systems, and it comprises the following main parts, the carrier, ranging codes, and the navigation message [7]. The codes are then categorized into coarse acquisition and precise [5]. The American system (GPS configuration) will mainly be used to further describe GNSS concept and signals.

2.3.1 The Carriers

The International Telecommunication Union (ITU) allocated two frequency bands for radio navigation satellite systems. The lower and upper bands both utilize the L-band [7]. However, the selection of this band for satellite navigation services is not random and highly connected to the system requirements, technical specifications, and propagation effects[4]. Hence, all GNSS operate in the L-band and overlap, increasing the robustness of carrier phase–based positioning [1]. GPS signals are coherently driven from the same 10.23 MHz crystal[5]. Multiples of this fundamental frequency are then used to generate different carriers[5]. Currently, GPS broadcasts in three frequencies, L1, L2, and L5[4]. Initially, the second frequency was intended to offer redundancy and to account for the dispersive atmosphere (ionosphere) delay[5]. Table 2.2 below summarizes the carriers for legacy GNSS constellations.

Table 2.2: The used carriers for the earliest GNSS systems [4, 5]

GNSS System	Frequency 1 [MHz]	Frequency 2 [MHz]	Frequency 3 [MHz]
GPS	L1 = 1575.4	L2 = 1227,6	L5 = 1176.5
GLONASS	G1 = 1602 to 1615	G2 = 1246 to 1256	-

2.3.2 Ranging Codes

Consisting of Coarse Acquisition/Civil code (C/A code), Precise code (P code), and Anti-Spoofing code (P(Y) code) [4, 5], GPS ranging codes occupy the carriers enabling the receivers to compute the propagation delays and hence calculate user's ranges to satellites [4]. It is worth mentioning that the P(Y) code is an encrypted version of the P code by the so-called W code [4]. The Anti-Spoofing code is available for military applications only and restricted from civil use [5]. Previously, the US. Department of Defense enforced degradation to the signals to prevent civilian use, using a process known as selective Availability (S/A) [1, 5]. This is however, no longer the case.

The codes digitally modulate the carrier phase utilizing the Quadrature Phase Shift Keying (QPSK) method [3]. Nowadays, both carriers L1 and L2, are modulated by both codes [5]. The latest frequency, L5, is intended to support civil applications only [1]. Ranging codes are generated employing a prescribed algorithm [4] using Modulo 2 addition (the exclusive OR (XOR) operation) along with linear feedback registers [3]. The length of each code depends on the register size according to equation (2.1), then it repeats [5]. The receivers use the correlation between the transmitted signal and the locally generated copy to calculate the delay [1]. Benefiting from the code division multiple access (CDMA) technique, these codes are orthogonal, i.e., zero correlation [4], allowing the receivers to receive signals from several satellites simultaneously [1].

$$L(n) = 2^n - 1 \tag{2.1}$$

The C/A code is a 10-stages register sequence; hence using equation (2.1), the C/A code is 1023 bits long, transmitted every 1 ms [5], and modulates the in-phase part of L1 at a rate of 1.023 MHz (multiple of the fundamental frequency) [4]. On the other hand, the Precise code modulates the quadrature component of both carriers and has a frequency of 10.23 MHz [8]. A new P code is transmitted every week and contains 2×10^14 bits (37 weeks long) [5]. More details about the specifications of both GPS codes are shown in table 2.3.

Table 2.3: Original GPS ranging codes characteristics [3, 4, 5]

Code	C/A code on L1	P code on L1 and L2
Frequency [MHz]	1.023	10.23
Chip rate [MBPS]	1.023	10.23
Chip length [m]	300	30
Type	37 unique codes	37 one week segments
Repetition rate	Millisecond	7 days
Modulation scheme	Bi-phase	Bi-phase quadrature
Additional properties	Easy to acquire, used by all users for acquisition of P(Y) code	More accurate but used by authorized users only

2.3.3 The Navigation Message

An integral part of GNSS signals is the navigation or data message. Despite its low rate, 50 bits per second, [5] it holds crucial information for positioning. The navigation message contains the ephemeris of the tracked satellite, i.e., information about orbital elements with terms to account for solar radiation and gravity perturbations and the satellite clock, which enable the user to locate the satellite at the time of transmission [3]. In addition, the data message includes information about the satellite health status, signal propagation error corrections [7], and the almanac data, which contains information about the status of all satellites in the constellation [5]. This part of the signal encompasses 25 frames of 1500 bits each. Hence it takes 12.5 minutes to be fully transmitted[5].

Moreover, each frame is divided into five subframes of ten 30-bits words [7]. Apart from the broadcast ephemeris message, as mentioned earlier, a more precise ephemeris is also computed and made freely available for all users [3]. The international network developed by IGS provides such accurate information [4].

2.4 Data Acquisition and Observables

Based on the correlation technique, the primary principle of GNSS is to deduce what is known as the observables by comparing the transmitted signal with its self-generated replication in the receiver [3]. The direct outcome of this process is the time or phase offset between the transmission and reception [4]. However, the acquired ranges differ from the actual geometric ranges since they account for the clock errors and other factors mentioned in subsequent sections, Hence the name pseudo-range observations [5]. GNSS employs two different techniques to obtain these observations. Depending on the calculated differences, GNSS results based on ranging codes are called Code Pseudo-ranges [3, 5], whereas carrier phase dependent measurements are called the carrier phase observables [3, 4, 5]. This section demonstrates both techniques in more detail.

2.4.1 Code Pseudo-ranges

Depending on the ranging codes and navigation message, the system can estimate the time difference between the satellite and receiver clocks [3]. A simplified model is obtained for the code pseudo-ranges, accounting for the absence of time synchronization between the space and ground elements and the speed of light in a vacuum [5]. Equation (2.2) below defines such pseudo-range.

$$P_k^s = (t^s - t_k) \cdot c \tag{2.2}$$

P_k^s is the pseudo-range between receiver (k) and satellite (s), and t_k and t^s are the receiver's clock time and satellite transmitting time, respectively, and c is the speed of light in a vacuum [4]. Finally, the actual range is calculated, ensuring that the clock errors are accounted for on both sides, leading to the following equation (2.3)

$$P_k^s = \rho_k^s(\tau^s, \tau_k) + (\Delta t^s - \Delta t_k) \cdot c \tag{2.3}$$

Where ρ_k^s is the true geometric range considering the true clocks time τ_k τ^s, and $(\Delta t^s - \Delta t_k)$ is the clock correction term.

Another less apparent error is connected to the electromagnetic wave's properties and the propagation medium [4]. Because the refractivity index (n) of the propagation media is different from one, GNSS signals encounter several delays during their travel from space [9]. These delays are connected to the dispersive, i.e., ionosphere, and non-dispersive, i.e., troposphere, components of the Earth's atmosphere [3] and will be further described in forthcoming sections. Accounting for such delays resulted in a more sophisticated model for the code pseudo-range, as shown in the following equation (2.4).

$$P_k^s = \rho_k^s(\tau^s, \tau_k) + (\Delta t^s - \Delta t_k) \cdot c + I_k^s + T_k^s \tag{2.4}$$

Noting that I_k^s is the ionospheric contribution (delay), and T_k^s is the tropospheric delay.

The observed data is incorporated with initial guesses ($P_{Computed}$) to calculate the residual observations using the taylor approximation [3]. Thus, the pseudo ranges will be converted into positions [5]. Then, from the pythagorean theorem, the actual range can be written in terms of position as follows (equation (2.5).

$$\rho_k^s(\tau^s, \tau_k) = \sqrt{(x^s - x_k)^2 + (y^s - y_k)^2 + (z^s - z_k)^2} \tag{2.5}$$

The satellite coordinates (x^s, y^s, z^s) and clock bias (τ^s) are easily accessible using the navigation message and precise ephemeris [3, 5]. Therefore, tracking at least four different satellites is necessary to identify the remaining four unknowns, i.e., the receiver's coordinates (x_k, y_k, z_k) and clock bias (τ_k), in equation (2.5) above.

It is worth mentioning that the accuracy of the resulting positions is highly affected by the pseudo-ranges accuracy and, most importantly, the geometry of which the receiver sees the tracked satellites at a specific epoch [3, 5]. This phenomenon is known as the dilution of precision (DOP) [4] and will be detailed afterward.

2.4.2 Phase Pseudo-ranges

More meticulous measurements can be achieved operating the same concept, signals correlation, [5]. However, instead of using ranging codes, these methods utilize a comparison between the carrier phase of the transmitted and its locally generated replica [3, 5].

Furthermore, the carrier beat signal, i.e., the difference in phase between the satellite signal and the local replica, is generated after mixing the two signals and filtering the high-frequency components [5], as shown in equation (2.6) below

$$\varphi_B(t) = \varphi^s(t) - \varphi_k(t) \tag{2.6}$$

where $\varphi_B(t)$ is the carrier beat phase, $\varphi^s(t)$ is phase of the transmitted signal, and $\varphi_k(t)$ is the reference phase.

Phase pseudo-ranges accuracy is significantly affected by the absence of a clear indicator of the real difference between the phases of the signals [3, 5]. Therefore, a compensation mechanism is to introduce an integer value to represent the misalignment between phase cycles of each source [5]. This value is known as the Phase Ambiguity parameter [3, 5]. As long as the receiver continuously tracks a specific satellite without disturbance, this number is constant. However, losing a satellite signal requires re-estimation for the phase ambiguity number [3, 5]. This discontinuity of the tracked signal is known as a 'cycle slip" [5]. Therefore, subtracting the phase ambiguity parameter from the estimated beat phase yields the actual carrier phase observable [3, 5]. Equation (2.7) below introduces this result.

$$\Phi(t) = \varphi^s(t) - \varphi_k(t) - N^s \tag{2.7}$$

$\Phi(t)$ is the true phase measurement estimated at time (t) and N^s is the phase ambiguity parameter for satellite (s).

Similarly, these observations can easily represent the range of the satellite by multiplying the phase measurement by the nominal wavelength (λ_o) after expressing the transmitting time and the reception time in terms of the reference frequency (f_o) and nominal phase (φ_o) [5] as in equation (2.8).

$$T(t) = \frac{\varphi(t) - \varphi_o}{f_o} \tag{2.8}$$

Consequently, the range can be written as follows in equation (2.9)

$$L_k^s(t_k) = \lambda_o f_o(t^s - t_k) - \lambda_o(\varphi_o^s - \varphi_{ok} - N_k^s) \tag{2.9}$$

The last three terms in equation (2.9) are all constants where φ_o^s is designed to be the same for all satellites and can be combined to form the so-called carrier phase bias B_k^s [5].

Therefore, the resulting model is formulated by accounting for the propagation delays (I_k^s, T_k^s) and replacing the system's time $((t^s, t_k))$ with the actual time and the time correction parameters [5] introduced in equation (2.3), considering that $\lambda_o f_o$ is equals to c, the speed of light in a vacuum.

$$L_k^s(t_k) = \rho_k^s(\tau_k, \tau^s) \; + \; (\Delta t_k - \Delta t^s) \cdot c \; - \; I_k^s \; + \; T_k^s \; + \; B_k^s \tag{2.10}$$

Note that, from equation (2.10), the dispersive atmosphere affects the carrier phase pseudo ranges with increased phase velocity, unlike the code pseudo ranges [5, 7]. Furthermore, the residual observations can be obtained by incorporating an initial guess ($P_{Computed}$) and using the taylor approximation [3]. This concept will be discussed in the following sections.

2.5 GNSS Receiver Building Block

GNSS are one-way communication systems where users are receive-only devices, i.e., passive systems [1]. The receiving system includes different parts, starting with antennas and radio front-end, the Digital Signal processor (DSP), the navigation processor, and GNSS software [10]. The following section describes the primary and central parts of the users' receiving system. Figure 2.1 below illustrates the main receiving components.

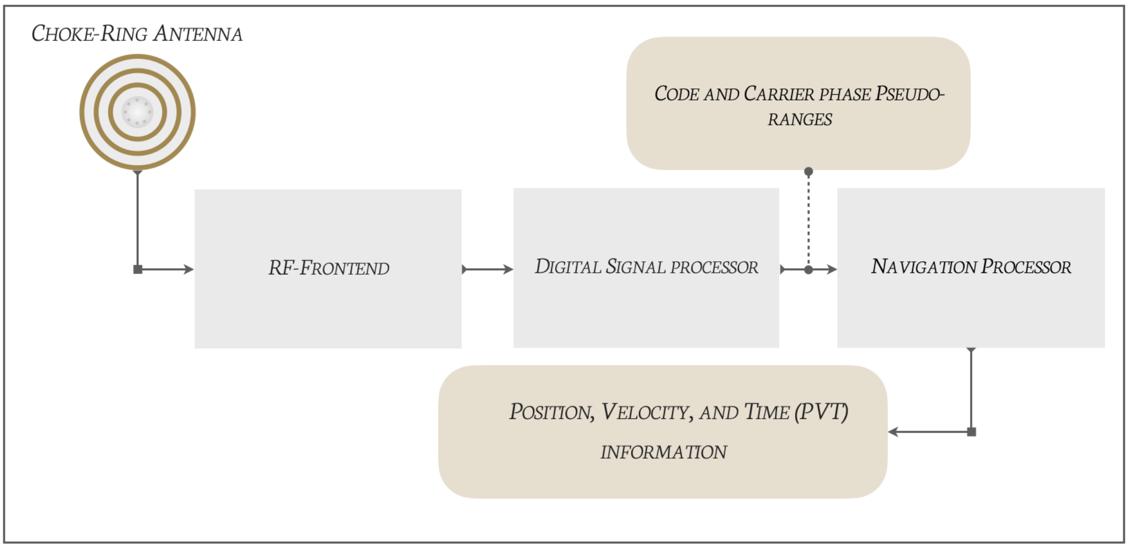

Figure 2.1: Main components of a GNSS receiver

2.5.1 Antennas

Antennas transmit or receive electromagnetic (EM) waves [11]. Antennas convert the energy from the received electromagnetic signals into electric current easily accessible by electronic devices [3]. Therefore, it is evident that antennas form an essential part of any receiving system [11]. However, for GNSS, the importance extends beyond this fact since it highly affects the accuracy of the results [3, 5]. Therefore, the critical role of GNSS antennas as the first step of the reception procedure requires special attention to specific performance requirements [10].

GNSS antennas are designed to obey several prerequisites to guarantee quality performance in terms of accuracy and availability [3]. Additional to the previous function of typical antennas, the unique GNSS antenna design ensures rejection of a high percentage of interference, multi-path, and reflections [10].

Tracking moving satellites require a uniform gain pattern. This is achieved by using omnidirectional antennas [1], meaning that the antenna has a broad beam [10] and have an identical gain pattern in all directions [3]. However, those antennas are coupled with a ground plane to restrict the radiation pattern to above the horizon and eliminate reflections [3, 10]. Another necessary characteristic, besides the gain pattern, is the antenna polarization [4], i.e., the direction in which the electric component of the electromagnetic waves propagates [11].

In general, GNSS antennas are cross-dipole types [10]. Consequently, they are Right Hand Circularly Polarized (RHCP) antennas [4]. Hence, they are purposely designed to have low gain for the orthogonal (cross-polar) component, which is the Left Hand Circularly Polarized (LHCP) signals [11] that might result from signal reflection [3, 4, 10]. This type of polarization is preferred over linear polarization due to its stability while traveling through the ionosphere [10]. Furthermore, using the so called choke-rings ground plane helps reduce the cross-polar components and back-lobes, hence the reflections [10], thus enhancing the axial ratios [10]. Another advantage of these rings is suppressing multi-path and reducing diffraction effects from the edges of the ground plane [10]. A choke-ring antennas can be seen in figure 2.2 below.

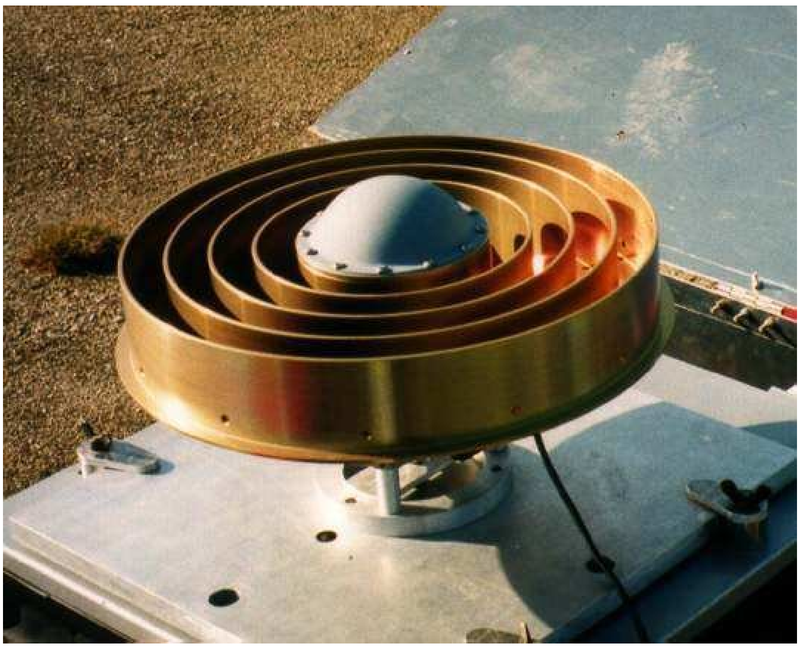

Figure 2.2: Typical GNSS receiver antenna [12]

In antenna theory, the size, and wavelength are directly connected to the radiation pattern and gain [11]. Since GNSS receiving antennas are used to continuously track moving satellites at approximately 4 km/second [7], it is necessary to have a gain pattern that facilitates tracking in different elevation angels, particularly low elevation angels (5° to 10°) [10]. Therefore, GNSS antennas should have uniform gain covering the upper hemisphere above the zenith and have a small size compared to the signal wavelength[4, 10] to satisfy this requirement.

The last and most crucial characteristic of GNSS antennas is the phase-center. The antenna phase-center is the point of measurement in which the antenna collects the radiated electromagnetic signals [10]. This point acts as a reference for the antennas. Its geometrical representation is known as the Antenna Reference Point (ARP) [3]. Although there is an ideal definition for these reference points depending on the geometrical properties of the antennas, these points are unanticipated [3]. The reason is that the ARP behavior mainly depends on the phase contour, azimuth, and elevation angles [3, 10]. Since the parameters above are not ideal and cannot be controlled, the antenna phase-center cannot be identified physically [3, 10].

On the other hand, the unknown electrical phase-center value is frequency-dependent, but this can be corrected by adding error correction terms called Phase-Center Offset (PCO) [10], representing the offset between the ARP and the mean electrical phase-center [3].

Another dependency that should be compensated for in addition to frequency is azimuth and elevation dependencies [3]. This can be corrected by considering phase-center variation for each carrier individually, the so-called antenna Phase-Center Variations (PCV) [3, 10]. The total correction is then a combination of both values [3, 10]. Computing the correct phase-center requires calibration [3, 10]. Several calibration models can be considered to estimate the correct phase-center point [3].GNSS antennas calibration methods include lab or field calibration, each method having its pros and cons [3, 10]. The following subsections present a brief description of those calibration criteria. More details can be found in [10].

2.5.1.1 Lab Calibration

In this method, a microwave anechoic chamber is used [3, 10]. In a controlled setting, the chamber mimics the line-of-sight environment and far-field radiation during the transmission and reception [11]. The calibration process includes a reference antenna with known parameters, e.g., phase-center, gain, radiation pattern, and the Antenna Under Test (AUT)[11, 10]. In addition, the chamber is equipped with EM radiation absorbing materials to eliminate the multi-path effect [11, 10]. Measuring the far field region is vital for this method [11], hence, the two antennas must be adequately separated [10]. The reference antenna transmits the signal toward the AUT, and special software is then used to estimate different parameters [11].

A primary advantage of this method is the availability of the EM signals using the reference antenna without the need to track satellites [10]. In addition, this availability allows an absolute calibration for all GNSS frequencies [10]. However, the drawback is the required size of the chamber, high cost, and the long estimation time [10].

In Compact Antenna Test Ranges (CATR) method, a large parabolic antenna is used to reflect the incoming spherical wave-front from the feed and convert it to a planar wave-front [10]. Thus, the separation between the antennas is unnecessary. Therefore, the cost and size of the required chamber are reduced [10]. Although this method provides the same advantages as the far-field method discussed earlier [10], it also has some disadvantages. For example, the resulting blockage from the feed, edge diffraction from the parabolic reflector or the feed, depolarization coupling, and reflections from the chamber walls [10].

On the other hand, the Near-Field Far-Field (NF-FF) method uses sampling of the near field region by a calibrated probe and then using analytical methods and Fourier transform to estimate the far field pattern [10]. However, details of those methods are beyond the focus of this master thesis, and more details can be found in [10].

2.5.1.2 Field Calibration

a ***Absolute Antenna Calibration***

The Absolute antenna calibration technique uses a unique robot to perform the absolute calibration [10]. Absolute here implies that the phase-center variations are driven without a reference antenna [3, 10].

A precisely controlled robot is used to rotate and control the AUT [3]. Since the antennas are RHCP, the phase varies as a function of the azimuth angle [10]. Thus, controlling the orientation of the AUT will result in a change in the phase and a topology of the phase pattern can be achieved [3, 10].

The multi-path effect can also be eliminated by using this method. The main idea is to repeat the observations from the same constellation every side-real day and then calculate the differences between the measurements [3, 10]. The reason is that the far field multi-path repeats every day at the site [10]. An important note is an offset between the solar and the side-real day (about 4 minutes) [3, 10].

b ***Relative Antenna Calibration***

As the name indicates, this method estimates the phase-center of the AUT by utilizing a reference antenna [3, 10]. The method has been developed by the National Geodetic Survey (NGS) [10].

The concept is to mount the AUT and reference antenna in separated stable piers, typically with a separation of 5 meters[3, 10]. Both antennas are connected with receivers driven by the same atomic clock [10] . In the beginning, antennas are oriented toward the north, eliminating any changes resulting from any offset from the initial position [10].

The phase-center is estimated using the azimuth and elevation angles of the satellites [10]. Then, each carrier's average phase-center is computed individually relative to a known phase-center position [3, 10]. The a priori position is predetermined by using the reference antenna instead of the AUT before conducting the measurements [3, 10].

All previously mentioned calibration techniques consider calibrating the antenna and its radome without considering the surroundings and the site specifications [3, 10].

This project considered an alternative calibration method that uses predetermined accurate points to calibrate the AUT on-site, i.e., the station calibration technique. See the method section for more details.

2.5.2 Radio Frequency (RF) Front-end

The primary function of the RF front-end is to provide reference frequencies and timing[3]. It consists of several blocks where each performs a specific function [3, 10]. First, a Low Noise Amplifier (LNA) amplifies the incoming signals [10]. Then, after filtering the noise and interference, the carriers are down-converted to Intermediate Frequencies (IF) without modifying the PRN codes [3, 10]. The last step is sampling and quantization to discretize the received analog signals [3, 10].

2.5.3 Digital Signal Processor

In this functional block, signal acquisition and tracking are conducted [3, 10]. The first stage is the received discrete signal input into multiple channels, a channel for each satellite in modern receivers [3]. Next, a copy of a specific satellite signal is generated in each channel, employing the correlation technique [3, 5, 10]. After that, the DSP starts searching for the maximum autocorrelation between the two signals, the so-called signal acquisition [3, 5, 10]. Finally, the correct signals are followed over time. This process is known as tracking [3, 10].

Acquisition and tracking are closely connected, and the resulting successfully tracked signals are marked as locked [3, 10]. The outputs of this block, i.e., code and carrier phase pseudo-ranges are then sent to the final receiving stage [3, 5, 10].

2.5.4 Navigation Processor

The final step is position, time, and velocity estimation [3, 10]. The process starts by decoding the navigation message to compute satellite positions, followed by using code and phase measurements to estimate position, velocity, and time information [3, 10]. Another function of this functional block is to supply aiding information to filters and tracking loops [3, 10]. The results are then sent to the storage unit in the receiver following a specific format known as a receiver-independent exchange format, RINEX for short [3, 5, 10].

2.6 Data Processing

There are a variety of available processing programs for postprocessing and using the PPP method. Thus, a unified RINEX format was introduced [3]. The latest version is RINEX.3.0, developed in 2006 [3].

RINEX files are divided into two main parts, header and data block. The header contains various information about the station, the observed data, and satellites, among others [13]. The data block contains the information, including raw range and code data [3, 13]. Integrated with the RINEX files, the software then estimates the position depending on the selected positioning technique [3, 5, 10]. The following subsection introduces a description of the precise point positioning method.

2.6.1 Precise Point Positioning

PPP is a non-differencing technique [4] but more accurate of the two [3] . The primary advantage is utilizing precise orbits, precise clock parameters, and dual-frequency [3, 5]. Combining the above parameters with code and carrier phase observables, PPP can achieve centimeter level accuracy [3, 7].

Unlike the differential methods, PPP requires a single receiver [7, 14]. Mainly, PPP benefit from the pre-estimated accurate orbits and clock data that have been calculated by a network of stations, i.e., several kilometers apart. One example of such a network is IGS international networks [3, 5, 7]. Furthermore, employing a network of reference stations enhances the precision of the estimated parameters [3, 7]. PPP is thus more robust to reference station failure [7].

Many institutes have developed software to support high precision positioning like PPP. One example is the GNSS-Inferred Positioning System and Orbit Analysis, i.e., GIPSY-OASIS, developed by NASA Jet Propulsion Laboratory (JPL) [4, 5]. GIPSY is composed of UNIX shell-based scripts to compute and save data for orbits, clocks, and geophysical parameters [15]. BERNESE and GAMIT are other examples of high precision software packages developed by the University of Berne, Switzerland, and the Massachusetts Institute of Technology, USA, respectively [3, 4, 5].

2.6.2 GIPSY-OASIS and PPP Algorithm

PPP's main principle combines the so-called ionospheric-free observables with precise orbits, clock data, and error correction models to estimate the residuals [7]. The main two processes are highlighted to explain the PPP and GIPSY algorithm further.

2.6.2.1 Data Editing and Integration

Through continuous collaboration, a network of global stations, e.g., IGS, provides accurate satellite clocks and orbits [13, 14, 15]. GIPSY integrates pre-determined precise error models, including geophysical models, station information, and antennas data, with the provided satellite data to calculate an initial guess for the range between the satellite and station, $P_{Computed}$ [7, 15].

Before the calculation, the received observations are edited, decimated, and combined to form the ionospheric-free observables (L3 (or Lc), P3 (or Pc)) mainly processed [3, 7, 15]. These observables result from the difference between carrier or code measurements for both frequencies [3, 7], as shown in equations (2.11) and (2.12).

$$L3 = \frac{f_{L1}^2}{f_{L1}^2 - f_{L2}^2} L1 - \frac{f_{L2}^2}{f_{L1}^2 - f_{L2}^2} L2 \tag{2.11}$$

$$\begin{aligned} L3 &= 2.546L1 - 1.546L2 \\ P3 &= 2.546P1 - 1.546P2 \end{aligned} \tag{2.12}$$

Where f_{L1} and f_{L2} are the carrier frequencies, e.g., 1575.4 and 1227,6 for GPS in this case, L1, L2, and P1, P2 are the carrier phase and code pseudo-ranges for the first and second frequencies.

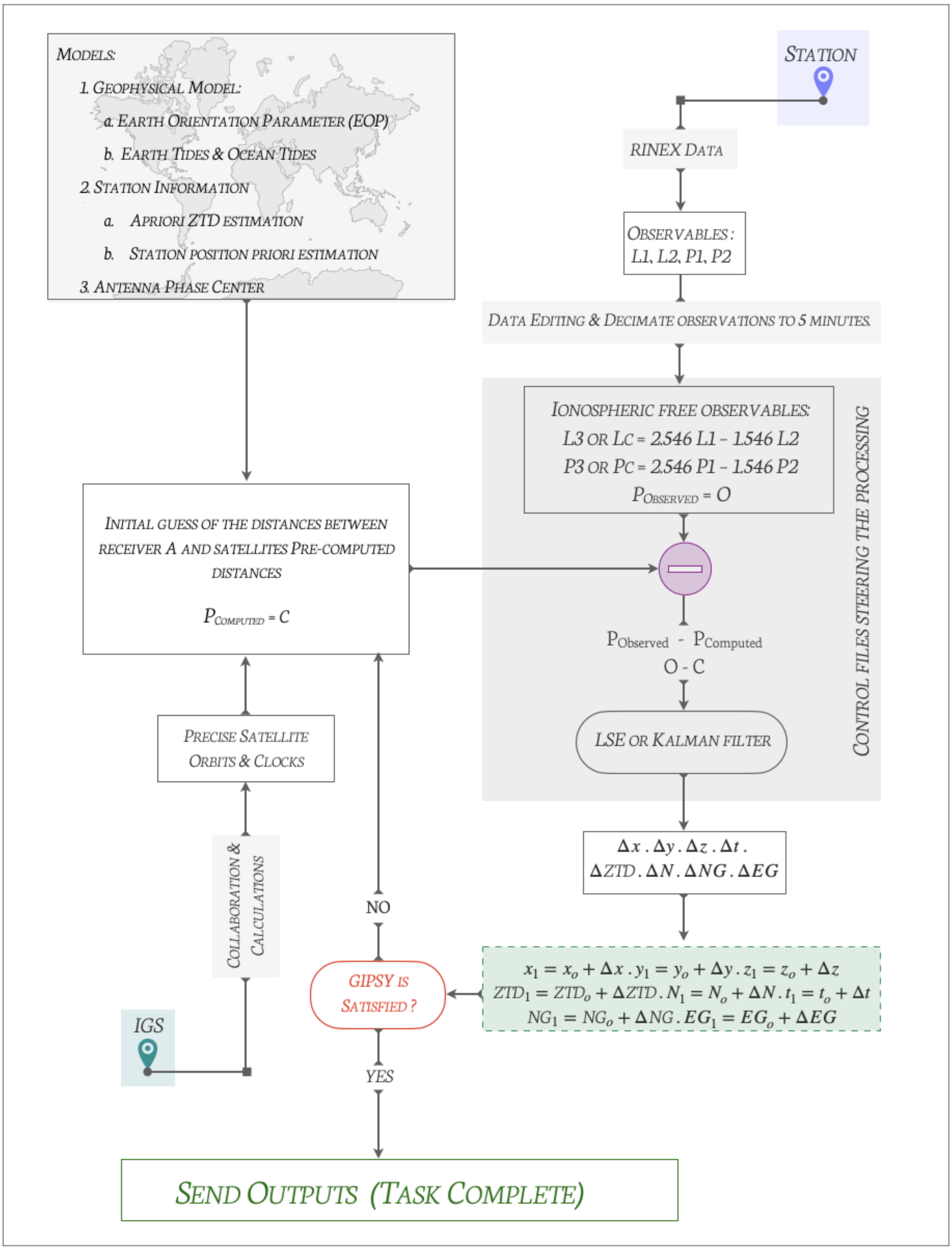

Figure 2.3: Schematic illustrating the GIPSY processing algorithm

2.6.2.2 Filtering

Before filtering, the empirical ionospheric-free measurements are incorporated with the computed initial guess [5] as in (2.13).

$$Data = P_{Observed} - P_{Computed} \tag{2.13}$$

Steered by pre-arranged control files containing the desired condition and constraint for the different results [15], the data are automatically processed utilizing the Least Squares Estimation technique (LSE) or a Kalman filtering process [3, 5, 15]. The Kalman filter is preferred over the traditional LSE due to its ability to incorporate time updates to the process (dynamic model) [3, 15, 16].

The filter relies on stochastic models, predictions, and covariance matrices to estimate the results [3, 7]. Finally, Kalman's results (residuals) are estimated iteratively using the updated residuals and state vectors [3]. The filter continues processing until the errors are in the accepted range identified by the control files [3, 5, 13, 16].

The primary outcomes from such a process are positions (x, y, z), time (t) estimations, tropospheric bias (ZTD), gradients (G), and phase ambiguity corrections (N) [5]. However, following the user's instructions, the high precision program, GIPSY, handles the different outputs. For example, positions and phase ambiguities are considered constants [3, 5]. Whereas, tropospheric delays, and gradients follow random walk processes [5], the offset between two consecutive values is strictly determined [17]. On the other hand, time is more problematic because it has a random behavior similar to white noise, values are independent for each epoch [5]. Figure 2.3 above illustrates GIPSY processing utilizing the PPP method.

2.7 Limitations and Error Sources

GNSS is based on a probabilistic approach and utilizes stochastic models to estimate the position, time, and velocity [3, 5, 18]. Thus, considering the dispersion of measurements, precision, around a mean and the deviation from the actual value, accuracy, is indispensable for GNSS results [18]. Furthermore, the above features are strongly affected by systematic and random noise associated with code or phase pseudo ranges [3, 18].

Although some systematic errors, biases, are mitigated and significantly reduced by modeling additional terms in the observation equations [3], random errors are more challenging and require careful attention [3, 18].

Different errors can be categorized according to their sources into three groups: satellite-based errors, propagation-medium-related errors, and receiver-related errors [3, 4, 18].

2.7.1 Satellite-related Errors

Orbit perturbations and clocks bias are the most apparent satellite related errors [3, 4, 18]. Although satellites are equipped with high-stability atomic clocks [1, 3, 4, 5], attention is required to account for any biases that these clocks encounter [3]. However, precise point positioning and differential techniques compensate for satellite clock errors [3, 5]. In addition, the control segment is continuously monitoring and tracking the satellites hence maintaining and correcting clock errors if required [18].

On the other hand, satellite orbits are designed in a sophisticated manner to achieve accurate positioning [5]. However, different factors affect the stability of these orbits [3, 18]. First, the non uniform shape of the Earth is one of the main elements that impact satellite orbits [6, 18]. The Earth is not a perfect sphere. Its shape is oblate spheroid [6], meaning that the equatorial radius is larger than the polar radius (the Earth is flattened in the equator) [3, 6, 18]. This non-homogeneous distribution of mass results in two effects [18], mainly the regression of nodes and the rotation of apsides [6, 18]. Regression of nodes results from the sliding of nodes, the ascending and descending nodes, in the equatorial plane [6, 18]. On the other hand, the rotation of apsides, apogee and perigee, is due to the non-central geopotential of Earth [18].

The second aspect is the direct impact of other celestial bodies [3, 6, 18]. For example, orbits are affected mainly by the gravitational force of the Sun and the Moon [3, 6, 18], with the Moon being the dominant contributor [18]. Moreover, the indirect impacts of these celestial bodies are tidal and ocean loading effects that deform the shape of Earth and hence change its gravitational potential [3, 6, 18]. Besides the above factors, solar radiation pressure is another disturbing factor for orbits [18]. It results from the photons radiating toward the satellite surface [18].

2.7.2 Receivers-related Errors

Like satellites, receiver clocks are also an error source that requires correction [3, 4, 18]. It is worth noting that introducing well-defined reference frames is vital for precise positioning [18]. Two reference system realizations are essential for satellite navigation, namely the Celestial Reference Frame (CRF) and the Terrestrial Reference Frame (TRF) [3, 6, 18]. In addition, the transformation between these reference frames is equally important [18]. Corrections for such errors, also known as Earth rotation corrections, include modeling and integration into the software package during the processing [3]. In addition, receivers' systematic errors are eliminated using the differential techniques [3].

Another receiver-related error that affects pseudo ranges is hardware delays, such as antennas, cables, and filters [19]. However, since these errors are constant for all observations, their correction is incorporated with the receiver clock corrections [19].

More challenging error sources are antenna-related errors [3, 4]. The antenna phase-center is a dominant error source that highly affects the results [4, 3]. As mentioned in earlier sections, these errors are mitigated through antenna calibration methods [3, 4, 5, 18]. Different calibration techniques were explained in detail in section 2.5.1. The calibration matrices are integrated during data processing [3].

On the other hand, multi-path is uncontrollable. It results from the reflecting objects around the station, especially at low elevations [3, 4, 18]. Furthermore, both measurements, code and phase, are affected by multi-path, But the effect on code measurements is much higher compared to phase observations [3, 18]. Several strategies are used to mitigate multi-path effects, one of which is directly connected to the antenna design [3]. As mentioned earlier, the choke rings are intended to eliminate reflections and multi-path effects [3, 10, 18]. In addition, improving filtering, signal design, and polarization can also reduce multi-path effects [6, 10]. However, the best approach is to avoid blockage and reflectors by placing the stations as far as possible from such obstructions [3, 18].

Recalling the concept of GNSS, the system requires four or more satellites to function correctly [1, 4, 18]. However, the distribution of those visible satellites above the horizon for the receiver is crucial for high-quality results [1, 3, 5]. This distribution is referred to as satellite geometry [1, 3, 5]. The standard measure for this behavior is the Dilution Of Precision (DOP) [1, 3, 4, 5]. DOP measures the degree to which satellite geometry dilutes the result's accuracy [1]. Thus, low DOP indicated good geometry, i.e., visible satellites of different elevations and positions, and vice versa [3, 5]. Furthermore, DOP is considered during data processing [3].

The phase ambiguity parameter is the last and most complex receiver-related error [1, 3, 4, 5, 18]. This parameter affects only carrier phase measurements [18]. Phase ambiguity originates from the misalignment between the received signal and its locally generated replica [3, 4, 5, 18]. It is an integer value representing the number of cycles that oscillates since the first measurement [5]. This number will be constant for all measurements unless the receiver loses the tracked satellite resulting in a cycle slip. Hence a new estimation is required [3, 4, 5]. The phase ambiguity parameter is compensated for by an additional term in the pseudo ranges equations [3, 5]. A rough calculation reveals that each day the total number of calculated ambiguities, considering continuous tracking (no cycle slips), four satellites/constellation (4) for each carrier (8), and that the satellites has a period of 12 hours ($8 \times 2 = 16$), the total for all constellations is 64 ($16 \times 4 = 64$).

2.7.3 Propagation Medium-related Errors

The GNSS space segment transmits electromagnetic waves towards the Earth. Those signals are then filtered, processed, and used for various applications [9]. However, signals traveling through the inhomogeneous atmosphere are delayed and attenuated due to the variation of air density in different atmospheric layers [3, 4, 9, 18]. In addition, it is worth mentioning that the propagation velocities (ν) depend on the speed of light in a vacuum (c) and the refractive index (n) [3, 4, 9, 18]. Equation (2.14) represents this relation [3].

$$\nu = \frac{c}{n} \tag{2.14}$$

Moreover, in equation 14, unless n is one, the propagation speed will change, i.e., delay or advance, from c [3, 4]. These delays form significant error sources for GNSS measurements [1, 3, 4, 5]. However, for GNSS, the atmosphere is divided into two layers, the dispersive and the neutral atmosphere [3, 4, 9, 18]. These layers affect the signal differently depending on their properties [3, 4, 9]. The following subsections provide more detail.

2.7.3.1 Dispersive Atmosphere Delays

Since the transmitted signals propagated first through the dispersive, i.e., frequency-dependent atmosphere, the ionosphere, it is more convenient to start discussing ionospheric-related errors. The ionosphere significantly impacts EM wave propagation [3, 4, 9, 18]. Extending from 60 km to over 1,000 km above the earth's surface, it contains partially ionized gases resulting from solar radiation [1, 4]. This characteristic implies that exposure to the Sun ionizes the neutral atoms during the daytime and produces free electrons, increasing the electron density [18]. On the other hand, these electrons and ions recombine at night, resulting in lower electron density [18]. Thus, according to their electron densities, the ionosphere is divided into four layers, D, E, F1, and F2 [4].

The speed of a signal traveling through the ionosphere depends on the previously mentioned electronic density, making it difficult to predict and estimate these layers [1, 4]. However, GNSS benefits from the ionospheric dispersive property to eliminate the associated delays [3, 4, 9, 18]. The elimination process starts early during the processing. The so-called ionospheric-free observables (see equation (2.11)), resulting from the dual-frequency method, are generated and used to estimate the position, time, and velocity [3, 4, 18]. A point worth mentioning is that this method compensates for 99% of the ionospheric delay. The remaining percentage is integrated with the tropospheric delays (since this delay is also elevation dependent) [18].

2.7.3.2 Neutral Atmosphere-related Errors

As the name indicates, the neutral atmosphere, mainly the troposphere and stratosphere, is non-ionized [3, 4]. Therefore, below 60 km, these layers have several impacts on the propagated waves, including changes in signal speed and direction (bending) [4, 9, 18]. Although the neutral atmosphere contains both layers, the associated delay is highly dominated by the troposphere. Hence this error is referred to as the tropospheric delay [3].

The troposphere is classified depending on its behavior into two constituents: the dry gases form the dry hydrostatic component; and the wet component resulting from the clouds and water vapor which highly depends on the weather conditions [3, 4, 9]. In practice, the calculations of the total tropospheric delay consider the ideal case, the shortest signal path in the zenith direction (at elevation 90°). Thus, the associated total delay is known as the Zenith Total Delay (ZTD) [3, 4, 9].

However, ZTD consists of two parts [9]. The delay caused by the hydrostatic component is referred to as the Zenith Hydrostatic Delay (ZHD), which includes effects caused by bending, and the unpredictable influence of water vapor forms the Zenith Wet Delay (ZWD) [9].

Unlike the ionospheric delay, the tropospheric delay is frequency independent. Thus, eliminating this effect can not be achieved by the dual-frequency method and requires more sophisticated models [3, 4, 18], primarily since this delay depends on the temperature, pressure, humidity,elevation, and location [18].

The tropospheric delay is elevation dependent, meaning that its values vary with elevation. Thus, an essential factor is the integration of the mapping functions [3, 18]. Their primary role is to estimate the ZTD in different elevations [9, 18]. There are different models and mapping functions that account for the tropospheric delay. The models are added during the processing and the ZTD is estimated as an additional term in the observation equations [3, 4, 9, 18].

In addition, atmospheric gradients are another critical parameter for ultimate precision and applications [9]. Gradients account for the variations in atmospheric delays at constant elevation angles with the azimuth direction [3, 9]. These variations depend on climatic and weather conditions, locally and regionally, which result in a non-symmetrical azimuth atmosphere around the site [9]. The atmospheric gradients are elevation and azimuth dependent, resulting in two components, the north-east gradient, and the east-west gradient. Hence, a mapping function is needed to account for the azimuth non-symmetry [3, 9]. The elevation dependence positioned the hydrostatic mapping function as a key parameter in the gradient's map function formulation, where the other parts compensate for the two gradient components (shortened north and east from here on) which are azimuth dependent [9]. Similar to the tropospheric delays, the gradient models are included during the processing.

2.8 GNSS Applications

Initially, GNSS was designed to support military applications [1, 3] mainly. However, in recent decades, the possibility of integrating GNSS measurements with other technologies added another dimension to GNSS applications [1, 3, 4]. Timekeeping, positioning, and velocity determination are the earliest and most widely known applications [1, 3, 4]. In addition, the integration of GNSS-based navigation devices in mobile phones facilitated personal navigation for everyone [1, 3].

The unique features of GNSS play an essential role in aviation and aircraft applications [3]. GNSS supports the aviation system requirements by providing accurate positions, but it extends by including integrity, availability, and continuity [3]. Utilizing GNSS in aviation added considerable advantages concerning efficiency and flexibility in route selection and increasing landing capacity [3]. GNSS also enhances safety levels and reduces flight time, fuel consumption, and maintenance costs [1, 3].

Maritime applications, including ocean, coastal and port operation applications, are also supported by GNSS [3]. It is worth mentioning that marine navigation is one of the original applications of GNSS [1].

Additionally, GNSS works as a support system for rail and road applications [1, 3] as navigation, guidance, fleet management, and autonomous vehicles. GNSS can not entirely support such applications due to interference and multi-path by environmental and artificial obstacles, e.g., mountains and tunnels. [3]. Mining and oil exploration, forest management, and geological monitoring are other interesting applications employing GNSS [1].

Furthermore, Scientific applications like geodesy and Earth study, climate and environment monitoring, disaster prediction and plate tectonics, and geo-dynamical phenomena monitoring, among others, are the most direct applications for GNSS [1]. Therefore, the accuracy requirement positioned the satellite navigation techniques as a crucial contributor to such applications [3].

As the number of GNSS-based applications increases, the emergence of GNSS in more applications is highly predictable [1], especially considering GNSS's rapid advancement [3].

2.9 Climate Monitoring and Numerical Weather Predictions

The unique design of GNSS signals and frequencies and the levels of accuracy and precision have positioned these systems as a tool for earth science and applications [3, 4]. The estimated results include estimations of both components of the tropospheric delays on the receiving side [3, 4, 18]. Furthermore, according to [4], the tropospheric refractivity is empirically related to the meteorological variables such as air density, pressure, water vapor content, temperature, and atmospheric motion. Hence, GNSS estimations are critical for atmospheric processes that directly and indirectly affect Numerical Weather Prediction (NWP) models [4].Furthermore, combined with weather observations, the ZTD can be used as a tool for water vapor precipitation prediction, climatology, and variability [4].

Recently, what are known as the GNSS Radio Occultation (GNSS RO) missions, also emerged to provide high accuracy atmospheric predictions [4]. For weather forecasting, the principle of the GNSS RO technique is to utilize the distorted signals from a GNSS satellite, hidden by the Earth, to estimate the changes in the atmosphere [4, 19]. Although this technique has been used for planetary science since the 60s, the development of GNSS dual-frequency enriched this concept economically and scientifically [19]. However, this process requires contributions from Low Earth Orbit Satellites (LEO) [4, 19]. These satellites are equipped with GNSS receivers, hence by tracking GNSS signals, the atmospheric characteristics are estimated [4, 19].

Climate monitoring is another application that requires high levels of accuracy and precision. GNSS RO features are suitable to such applications [4]. Moreover, since the RO observations are based on frequency rather than amplitude, their errors caused by clouds are negligible [19]. In addition, climate monitoring requires high stability, which is guaranteed for GNSS since they are operated by very stable atomic clocks [19]. The advancement of GNSS RO methods and the growing number of GNSS constellations will play a significant role in climate science and weather forecast [4].

3
Method

GNSS observations and results are highly influenced by a multitude of error sources as explained previously in section 2.7. In this project three GNSS constellations, particularly GPS, GLONASS, and Galileo, were utilized to study the Earth's atmosphere and its properties.

From the variety of different GNSS processing techniques, the PPP method was used. Details concerning PPP can be found in section 2.6.1. The PPP method provides close to absolute positioning given the required prior knowledge of precise satellite orbits and clocks, troposphere and ionosphere, the receiver system, and the local environment at the receiving stations.

During the project, different processing and calibration strategies were evaluated to investigate the significance of these strategies in improving the precision and accuracy of the results. Accordingly, by comparing results from different strategies the levels of the improvements in accuracy are assessed .

This section describes the overall approach of the process and the reasoning behind the selection of different strategies to mitigate GNSS limitations. It is worth noting that only the general approach will be presented despite the chronological order and various combinations to make the method section more understandable. However, different approaches and their results will be presented clearly and thoroughly in section 4 and the appendix.

The study included eight GNSS stations located at the Onsala Space Observatory. Mainly, the international IGS stations ONSA and ONS1 and the six OTT (Onsala Twin Telescopes) stations OTT 1 through 6. The Google earth map, figure 3.1, below illustrates the position of each station. It should be noted that the stations are mounted at different heights, which in turn, in particular affect the ZTD results despite the stations being in the same area.

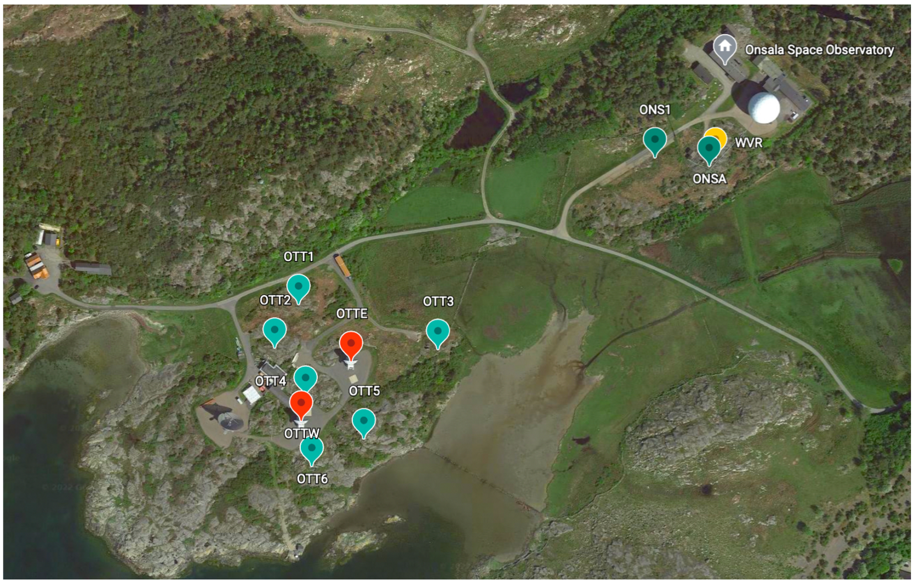

Figure 3.1: Map of the international and local GNSS stations at Onsala Space Observatory

At the early stages of the thesis work, the Javad receivers of the OTT stations were replaced with Trimble receivers. The reason being that the collected data by the Javad receivers resulted in very poor results when processed and analyzed. However, this exchange significantly increased the quality of the results, as can be seen in section E in the appendix. Therefore, only data collected after replacing the receivers was used to investigate the best possible calibration technique. The concluded reason for the poor quality of the Javad receivers was the logging of GLONASS data which resulted in deleting most of the GPS observations during processing. However, the exact rationale of this receiver error is unknown. As a result, before 2022, only the GPS and Galileo data were processed.

In addition to these stations, a few international stations were processed with the established optimal processing characteristics to test the performance of the selected parameters for stations in varying environments. These stations and their locations are listed in table 3.1. The resulting ZTD and gradients for the international stations can be seen in section 4.6 and appendix C.

Table 3.1: List of the seven international GNSS stations processed during the verification phase

Station Name	Location	Processing Period	Used Constellations
KOKB	Waimea - Hawaii	29 - 31 July, 2021	GE
KOKV	Waimea - Hawaii	29 - 31 July, 2021	GE
MDO1	Fort Davis - USA	29 - 31 July, 2021	GRE
GODN	Greenbelt - USA	29 - 31 July, 2021	GRE
GODE	Greenbelt - USA	29 - 31 July, 2021	GRE
GODS	Greenbelt - USA	29 - 31 July, 2021	GRE
WTZR	Bad Koetzting - Germany	29 - 31 July, 2021	GRE
ONSA	Onsala - Sweden	29 - 31 July, 2021	GRE
ONS1	Onsala - Sweden	29 - 31 July, 2021	GRE

Initially, three years of data (2019 - 2021) were processed for the observatory stations. After that shorter durations within the same period were mainly studied. The main reason for this was to compare the obtained results with WVR and VLBI results which were not available to the same extent as GNSS data.

The collected and used data were in the typical RINEX format files. The data was obtained from Lantmäteriet, The National Land Survey in Sweden, for the OSO stations. However, for the international stations,the data was obtained from IGS. More precise satellite orbits and clocks acquired from IGS were used to replace the navigation message broadcasted by the satellites, consequently, offering superior results.

Furthermore, the GipsyX software package also implements geophysical models of the Earth Orientation Parameter (EOP), Ocean loading, and Earth tidal effects. The EOP model is introduced to correct the errors caused by the earths orientation relative to the celestial reference frame, the CRF. Recalling that high quality models lead to more truthful results.

In general, GPS, GLONASS and Galileo are simultaneously used for most of the processing. However, some exceptions will be clearly explained and discussed further in the subsequent section.

3.1 Preparation and Data Processing

As mentioned previously, the software package GipsyX v.1.7 and the PPP processing method were used. In this section, the operation of GipsyX will be explained, accompanied by the different processing and calibration strategies examined in this project.

The practical part of the processing itself was relatively simple. During the preparation phase, processing scripts for the used constellations, GPS (G), GLONASS (R), and Galileo (E), were created, including details about the processing duration, i.e., 30 hours, antenna phase-center corrections, IGS satellite orbits and clock files, reference frames, and Earth orientation models. In addition, the batch files were generated for the intended stations and periods (from 2019 to 2021).

Moreover, the script naming followed a specific logic such that the title is explanatory. As an example, the script *GipsyX_PPP_GRE_30* indicates that GipsyX and PPP were used for processing data from three systems (GRE), and the processing period was 30 hours, i.e., the 24 hours of the day of interest and the successive 3 hours of the previous and following day. Basing the estimation on an extended duration improves the results as the Kalman filter has more time to stabilize.

An initial guess for the position (x_o, y_o, z_o), time (t_o), the phase ambiguity parameter (N_o), the total zenith delay (ZTD_o), and tropospheric gradient (NG_o, EG_o) is made as accurate as possible by applying the models mentioned above. GipsyX then combines the computed initial guess ($P_{Computed}$ (C)) with the ionospheric-free code and phase observables ($P_{Observed}$ (O)) and runs the resulting difference (O-C) through a Kalman filter.

After that, the Kalman filter estimates the residuals (Δ terms), i.e., the deviation from the initial guess of the receiver's position, the tropospheric delay, and gradients. The resulting values are then used to update the computed initial guess through the expression $x_{i+1} = x_i + \Delta x$. An identical procedure is performed for the remaining variables (y, z, t, N, ZTD, EG, and NG). If the results are not good enough from the users and their control factors point of view, the process will proceed with the updated values as the new initial guess.

The goal of the Kalman filtering procedure is to, from the best estimate at time i-1 and utilizing the covariance, predict the a posteriori value at time i utilizing the a priori estimate and corrections. The process repeats, until the best fit for all variables is obtained.

The position corrections as well as the phase ambiguity parameter are solved as constants over the epochs the satellite in question is tracked. On the other hand, the receiver time t is solved as a white noise parameter, meaning that the values of each epoch are independent of one another. More precisely, while the estimate for the clock at time i-1 is used to predict the value at time i, the estimation at time i is independent of the prediction.

The tropospheric components, ZTD, EG, and NG, are handled as a random walk process. Unlike the white noise, the predicted value at time i depends on the estimated value at time i-1 and the observed value at time i-1. The exact algorithm is performed in GipsyX "in the background" and is further explained in section 2.6.2.
For this study, the ZTD, tropospheric gradients and the coordinate results are of most interest. Therefore, these results are saved in specific, pre-determined files in the platform, the ZTD, GRAD, and Stacov folders, respectively.

3.2 Calibration and Processing Strategies

During this phase, different calibration and processing approaches were employed including gradient constraints, elevation cut-off angle, and antenna matrix. The ZTD and gradient constraints control the tightness of the data range determining which ZTD estimates will be kept, and which will be discarded. It is worth noting that these default ranges are guided by scientific facts and meteorological information. The elevation cut-off angle defines an angle under which the tracked satellites will not be included in the calculations. Finally, the antenna matrix is a model which characterizes the antenna phase-center as it is not necessarily identical to the geometric one.

3.2.1 Benchmarking

To start, three days (29 - 31 July, 2021) of data was processed with the default settings used by GipsyX. The ZTD constraint was 1.7e-4 [km/s^2], the gradient constraint was 1e-5 [km/s^2], and the elevation cut-off angle was 10°. The selection of days was highly influenced by weather stability and the availability of results from other measurement techniques for validation. In addition, the examined parameters were prioritized depending on their variability and impacts. Thus, the ZTD constraint was kept unchanged, considering the scientific approach used to specify the highest possible ZTD value and to limit the scope of the project. It would however be of interest to test different ZTD constraints in the future. The resulting ZTD, specifically the calculated ZWD, and gradient estimates were compared with measurements computed by the WVR and VLBI for the same selected days.

The primary outcomes of this phase were to investigate the performance of the typical system, identify hardware limitations, and identify a baseline for comparison, focusing on the uncertainties and overall trends.

3.2.2 Testing

During this step, different gradient constraints were tested. The baseline and tested constraints are summarized in table 3.2. Very tight constraints give smooth graphs, but many measurements will be omitted. Thus, they are not necessarily the truth. On the other hand, measurements are less controlled for loose constraints and can be used to verify the system's robustness. The associated noise however, is moderately high. Too loose constraints let through too much noise.

Table 3.2: The tested gradient constraints and elevation cut-off angles during the testing phase

Elevation angle
10°
7°
5°
3°

Gradient constraint [km/s^2]
1e-6
5e-6
1e-5
5e-5
1e-4
5e-4

The primary approach was to change JPL's default (safe) constraint and examine the implications of different values. The selection of values is trivial, however, the motivation was purely empirical, i.e., the selected value depends entirely on the observed results and comparison. These results can be found in section 4.

Nevertheless, when the best possible alternative for the gradient constraint was selected, several elevation cut-off angles were assessed. It is worth noting that only low elevation, below 10°, cut-off values were used. The reason is that high elevation cut-off angles would lead to fewer satellites being tracked, leading to fewer measurements being included in the calculations leading to poorer results. Moreover, the examined angles, i.e., 3°, 5°, 7°, and 10°, are commonly used in GNSS processing with 10° being extensively used by default. Although, 3° and 5° were very low, thus more susceptible to reflections, they were tested for verification purposes. The results were equally tested for many periods and compared to other methods such as WVR and VLBI when possible. The obtained results for the most convenient constraints are presented in section 4. The remaining results are available upon request.

Once the most suitable values for the gradient constraint and the elevation cut-off angle, in combination, were determined, the last step was to experiment with different antenna phase-center correction matrices. In particular, the default (model-specific) antenna matrix of the ONS1 station and the OTT stations were changed to antenna-specific phase-center matrices ,i.e, the antenna was calibrated prior to the station installation. The final calibration technique, station-specific, is explained in a subsequent section. Section 4.7 details the obtained results.

3.3 Measurements and Observations

In the following subsections, the analysis of the obtained results, as well as the comparison to WVR and VLBI, will be described in more detail.

3.3.1 Zenith Delays (ZTD, ZWD)

GNSS observes the accumulative tropospheric delay consisting of the wet and hydrostatic components. However, since the tropospheric dry constituents are significantly homogeneous and stable [9], the variability of the wet delay is more interesting when attempting to determine the quality of the results. Accordingly, the resulting tropospheric components for different calibration methods were compared to equivalent measurements obtained with a WVR, and VLBI.

It is worth noting that the comparison with VLBI measures was reasonably straightforward as the two techniques measure the same quantity (ZTD). On the other hand, the WVR measures the amount of water vapor in the atmosphere, consequently ZWD is estimated. Thus, to compare with the WVR, it was necessary to estimate the ZWD obtained by GNSS and VLBI. According to [21], the hydrostatic delay can easily be calculated, by estimating the air pressure (p) (in hectopascal or mbar), the station latitude (ϕ), and the ellipsoidal station height (h) in meters, and using the following equation (3.1).

$$\text{ZHD} = \frac{0.0022768 \cdot p}{10.00266 \cdot \cos(2\phi) - 0.28 \times 10^{-6} \cdot h} \tag{3.1}$$

Note that the height was calculated utilizing the GipsyX coordinate estimation. The pressure data were obtained from a pressure sensor at OSO. The same pressure data was used for all stations, since all stations are relatively close to each other and see the same atmosphere. The calculated ZHD was used to compute the ZWD.

This was plotted against the ZWD measured by the WVR using Matlab. As mentioned earlier, the WVR is highly sensitive to rain, thus, the sky camera at OSO was used to identify suitable dates, among the available, with reliable data for the comparison.

Further, throughout the project, Matlab was used for the data analysis, comparison, and visualization and to determine the degree of agreement between different measurement techniques and configurations. Additionally, the mean and root mean square (RMS) of the differences were calculated to make the results clearly determinable.

Apart from the comparisons with WVR and VLBI, the analysis included observing the general trends, uncertainty, error bars, and outliers. The analysis will be presented and discussed more in depth in section 4.

3.3.2 Tropospheric Gradients (GRAD)

Analyzing and comparing the North & East gradients are straightforward. GNSS, WVR, and VLBI results were compared using the same software (Matlab). Moreover, the mean and RMS of the differences were computed following the same logic.

3.4 Station-specific Calibration, Implementation and Setup

After identifying the best possible configuration, the final stage was to estimate site-specific calibration values for the stations at OSO. The measurement period was selected considering the weather conditions, i.e., avoiding snowy and rainy days, to ensure high-quality results.

At the observatory, four stations were set up at geodetic control network markers (around the main station ONSA) as shown in figure 3.2. These points have been measured multiple times by Lantmäteriet and OSO, so their coordinates are reasonably accurate. The antennas were mounted on stands and connected to four Javad receivers, more information is summarized in table 3.3.

Table 3.3: List of temporary stations mounted in precise geodetic checkpoints during (March - May 2022)

Station Name	Antenna Type	Receiver	Calibration
0302	Unknown Leica model	Javad (01590)	-
0303	Leica AR20 _ 23066002	Javad (01595)	28 April 2021
0304	Leica AR20 _ 23066005	Javad (01585)	2021
0501	Leica AR20 _ 23066017	Javad (01588)	2021

Data from the temporary stations were collected from March 2022 until May 2022. This tracking period was deemed sufficient to evaluate and estimate the required calibration values. The intention was to process the collected data using the BERNESE software and the differential techniques.

Unfortunately, due to time constraints, this process could not be finalized before the end of the project. However, the processing and analysis of the collected data will be continued.

(a) Station O302

(b) Station O303

(c) Station O304

(d) Station O501

Figure 3.2: Four temporary stations mounted in precise geodetic checkpoints during (March - May 2022)

4
Results and discussion

The main results of the project will be presented in this section. Finding a suitable approach to identify the best possible results was challenging since there are always unpredictable error sources that might affect the results. Therefore, the result assessment focused on minimizing the impact of the unexpected errors by examining, analyzing, and identifying the optimal configurations for specific variables in the control files.

The inspection included both the gradient constraints and the elevation cut-off angles. As a result, it was possible to eliminate or significantly reduce their associated errors by examining several combinations and assessing the performance of such groups of variables.

The second criteria was based on the comparison. For each processing strategy, a comparison between different measurement techniques was vital. In addition to the GNSS measurements, VLBI and WVR were used to compare the ZWD for the Onsala area.

The internationally available stations ONSA (or ONS0) and ONS1 were used as primary GNSS stations. Additionally, the available data for the twin telescopes, OTTE and OTTW, were used, mainly from 29 - 30 July 2021. Moreover, the pressure sensor at the observatory was equally used to calculate the ZHD and, thus, estimate the ZWD.

It is worth mentioning that non of the measurement techniques provide the absolute truth. However, the comparison concentrated on the general trend and error bars. In addition, some results will exclusively be presented in tables consisting of the calculated mean of differences, and root means square (RMS) values.

The results also present the ZTD and gradients for a few international stations employing the selected constraint and elevation cut-off angles.

Finally, the main focus of this project was to compare different antenna phase-center calibration methods. Antenna-specific and model-specific produced equivalent results for the eight GNSS stations at OSO. More elaboration can be found in section 4.7.

The analysis included many combinations for both gradient constraints and elevation cut-off angles. More information on the examined configurations is detailed in section 3.2.2. In addition, the processing strategies were examined for different periods from 2019 -to 2021, including three years of results and measurements for April 2021. However, only the most significant results will be shown due to the vast number of figures. Nevertheless, the entire catalog of figures can be obtained upon request.

4.1 Processing Strategies: Gradient Constraints and Elevation Angles

The following subsections discuss the significance of employing different processing techniques on the accuracy of the results. The main focus was to examine various gradient constraints and elevation cut-off angles and assess their impact on the result consistency and accuracy. Note that only model-specific antenna calibration method was used for this assessment.

The intention was to assess a combination of three GNSS constellations (GRE) and test eight stations at the observatory. However, apart from the two international stations, the remaining six showed significantly poor results for the intended systems and periods as explained previously. Thus, the result will only focus on ONSA and ONS1.

A note worth mentioning is that the reason behind the poor behavior of the six OTT stations was equally explored. The investigations showed that the error was receiver-related where the Russian system (GLONASS) contribution negatively affected GPS measurements. As a result, much of GPS data were removed during the processing, causing inaccurate results.

Nevertheless, improved results were achieved after eliminating GLONASS observations, and hence the six receivers were replaced. The new receivers work flawlessly for the GRE combination, results after receivers exchange can be found in section 4.7.

4.1.1 Baseline Assessment: 1e-5 and $10°$

The following subsection compares the three measurement techniques for the gradient constraint default value, i.e., 1e-5, in the processing software (GipsyX). The section focus on the most commonly used elevation cut-off angle 10°.

4.1.1.1 Zenith Wet Delay

As mentioned in section 2.7.3.2, the ZWD is less stable, and it highly affects the propagation of satellite signals. Thus, the zenith wet delay was considered throughout the analysis.

a ***Water Vapor Radiometer***

Figure 4.1 and 4.2 compare the ZWD estimated for GNSS stations, ONSA and ONS1, and the WVR for the 29th to 31st of July 2021. Both stations reflected similar results. However, a more fair comparison was to evaluate the mean and RMS of the differences between the two methods. These values can be found in table 4.1.

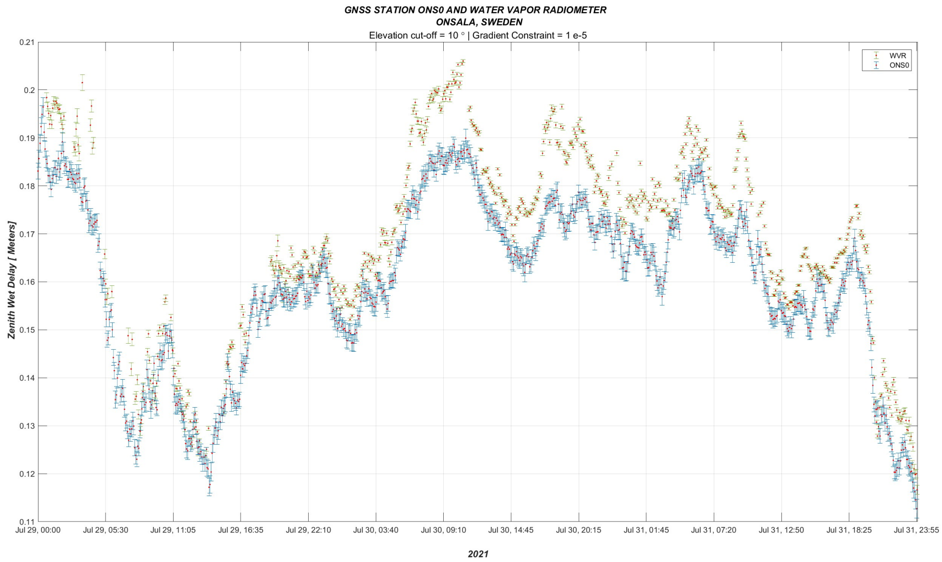

Figure 4.1: The time series of ZWD eatimated for the WVR and station ONS0

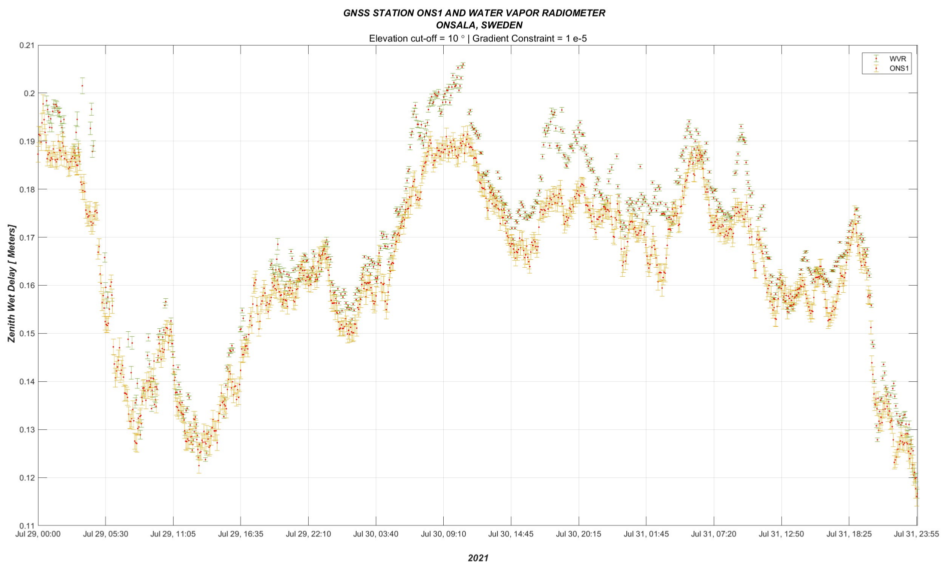

Figure 4.2: The time series of the ZWD estimated for the WVR and station ONS1

b ***Very Long Baseline Interferometry (OTTW and OTTE)***

The 20 m twin telescopes were also used for the ZWD comparison. Figures 4.3 and 4.4 show obtained results for the West and East VLBI, i.e., OTTW and OTTE, respectively. As opposed to the GNSS data, the telescopes' data were limited to one day. Data was handled carefully to ensure alignment. As a result, OTTE and OTTW showed identical results that coincide well with the GNSS results, where ONSA holds favorable outputs. Like the WVR case, table 4.1 below details the exact mean and RMS of the differences.

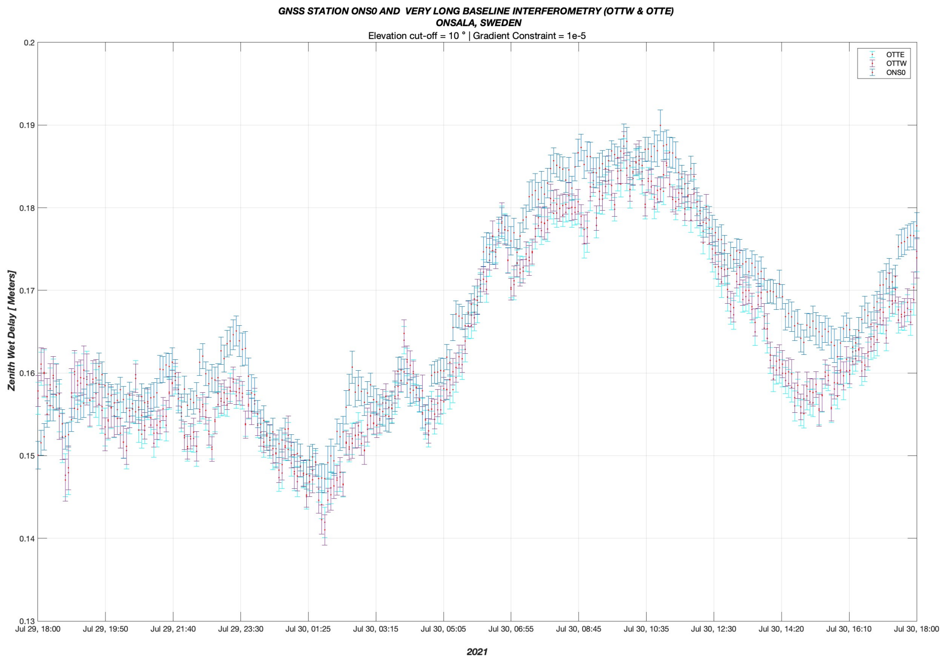

Figure 4.3: The time series of the ZWD estimated for the GNSS station ONS0 and the VLBI (OTTE and OTTW)

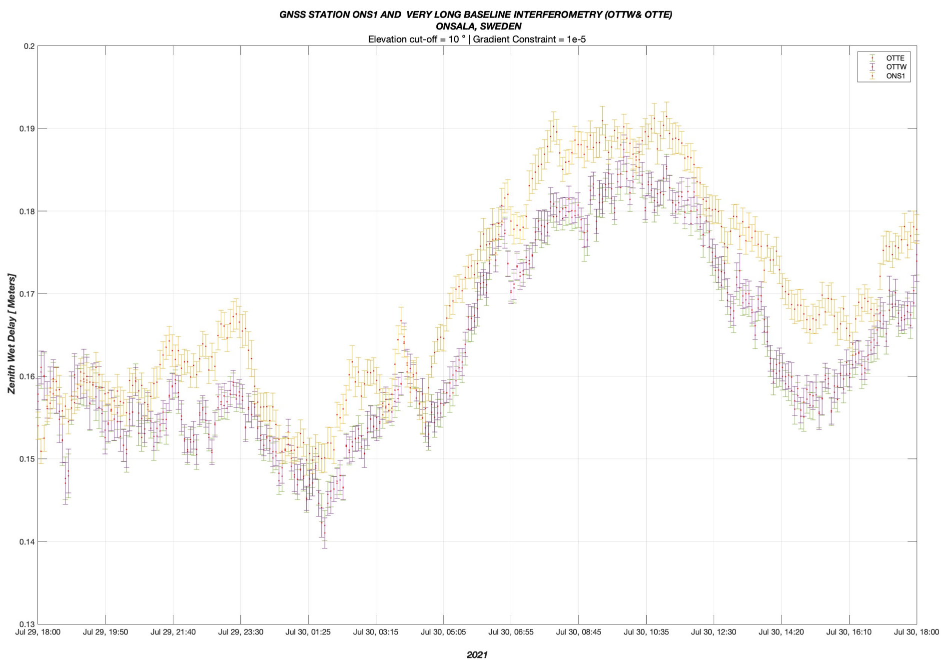

Figure 4.4: The time series of the ZWD estimated for the GNSS station ONS1 and the VLBI (OTTE and OTTW)

4.1.2 Tropospheric Gradients

a ***Water Vapor Radiometer***

Figure A.2 presents the time series of the estimated East (4.5a) and North (4.5b) gradients for ONSA for July 29-31. Again, ONSA shows consistent results following the same trend as the WVR. On the other hand, the WVR results contain many outliers, and the uncertainty of those outliers is relatively slight. Also, the WVR seems to have slightly higher values.

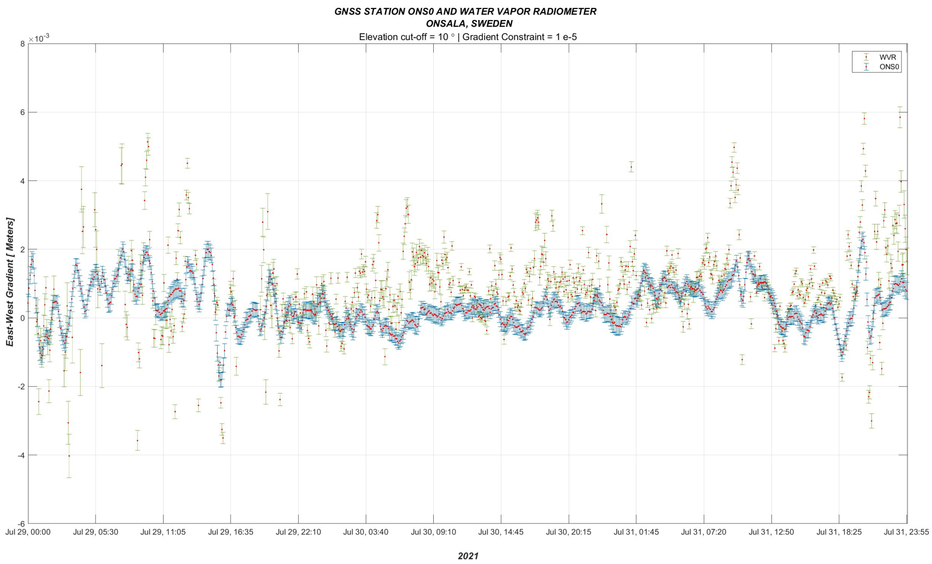

(a) East-West gradient estimated for station ONS0 and the WVR

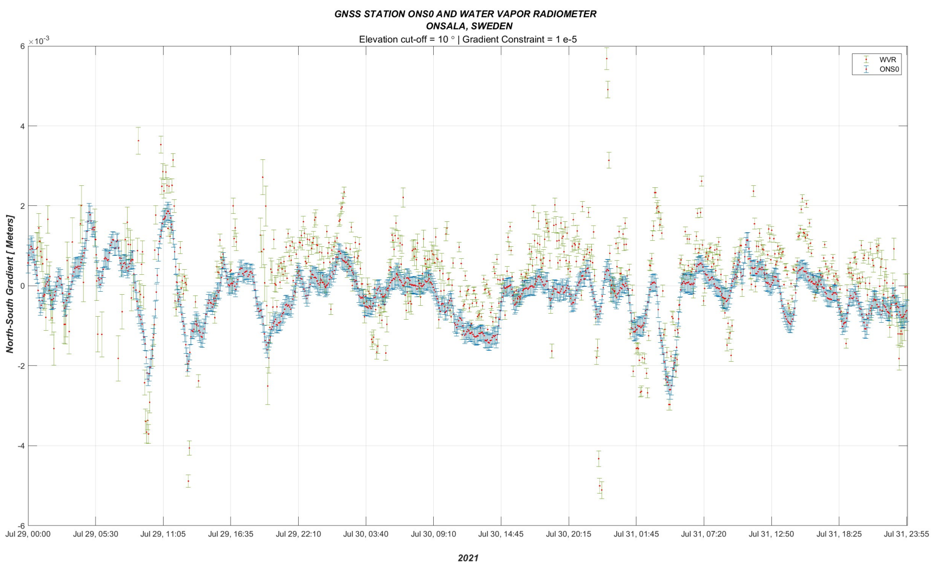

(b) North-South gradient estimated for station ONS0 and the WVR

Figure 4.5: Gradients time series of the East-West gradient (4.5a) and North-South gradient (4.5b) estimated for station ONS0 and the WVR

ONS1 was not an exception, and the station followed its preceding station. Similarly, the WVR showed scattered results and many outliers. ONS1 comparison with WVR can be seen in figure 4.6.

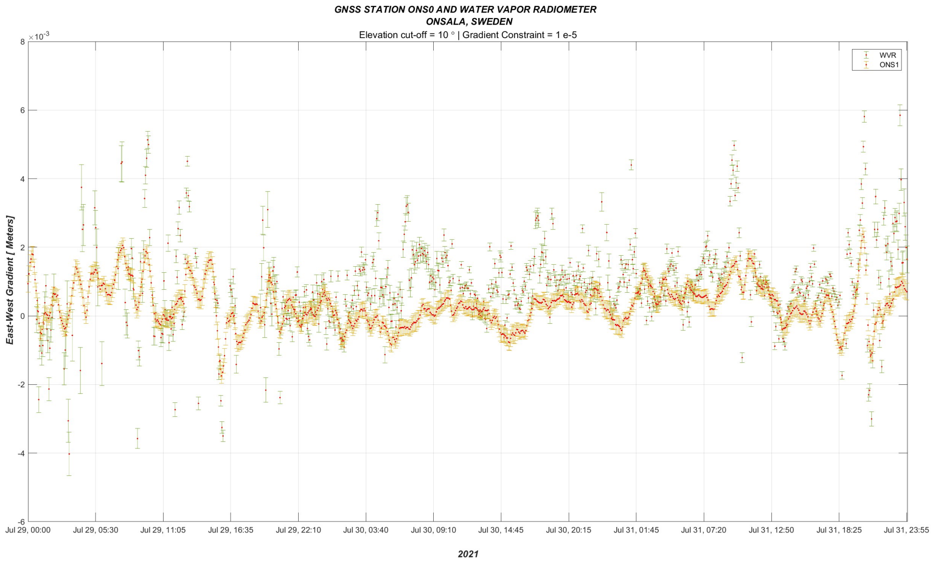

(a) East-West gradient estimated for station ONS1 and the WVR

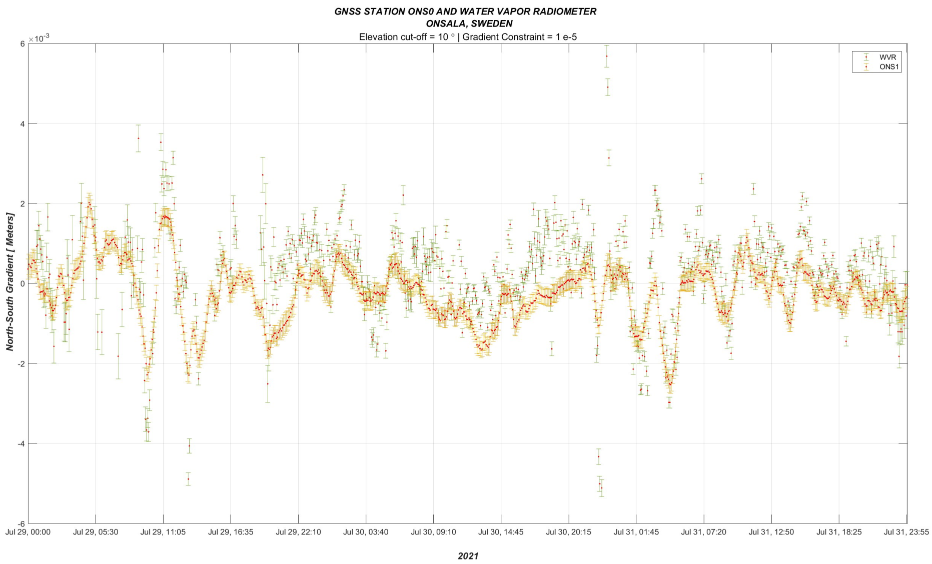

(b) North-South gradient estimated for station ONS1 and the WVR

Figure 4.6: Gradients time series of the East-West gradient (4.6a) and North-South gradient (4.6b) estimated for station ONS1 and the WVR

Using the default constraints, the measurements for both stations differ considerably from the WVR. The tables 4.2 and 4.3 contains comparisons of the mean and RMS of the difference.

b ***Very Long Baseline Interferometry (OTTW and OTTE)***

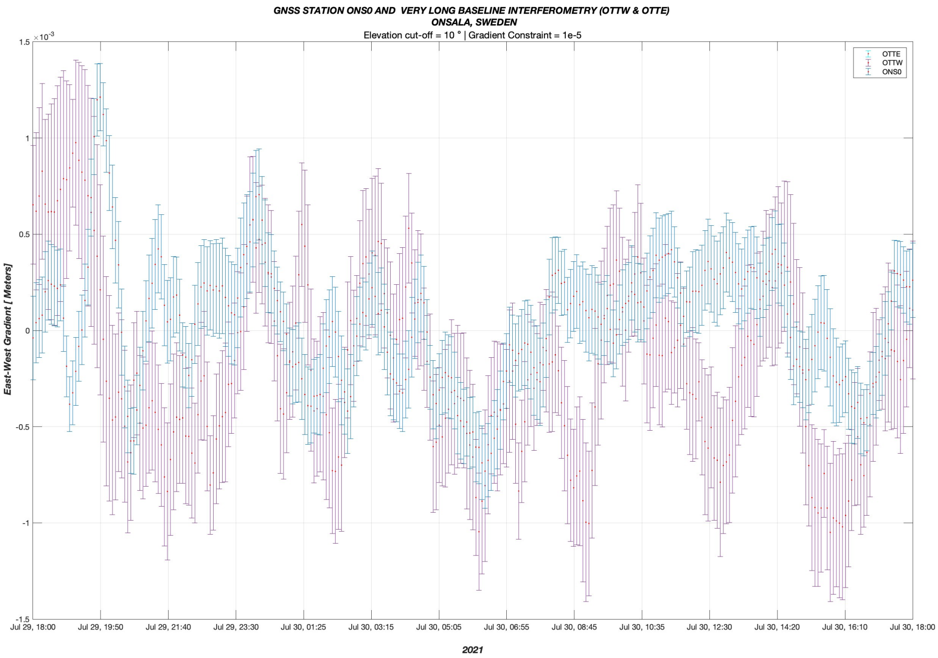

(a) East-West gradient estimated for station ONS0 and the VLBI

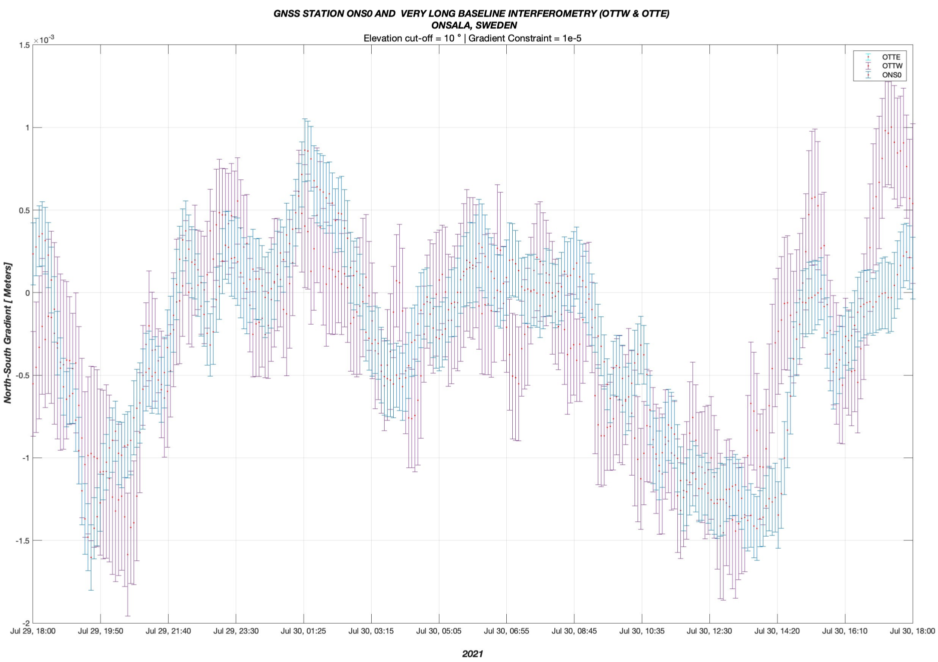

(b) North-South gradient estimated for station ONS0 and the VLBI

Figure 4.7: Gradients time series of the East-West gradient (4.7a) and North-South gradient (4.7b) estimated for station ONS0 and the VLBI (OTTE and OTTW)

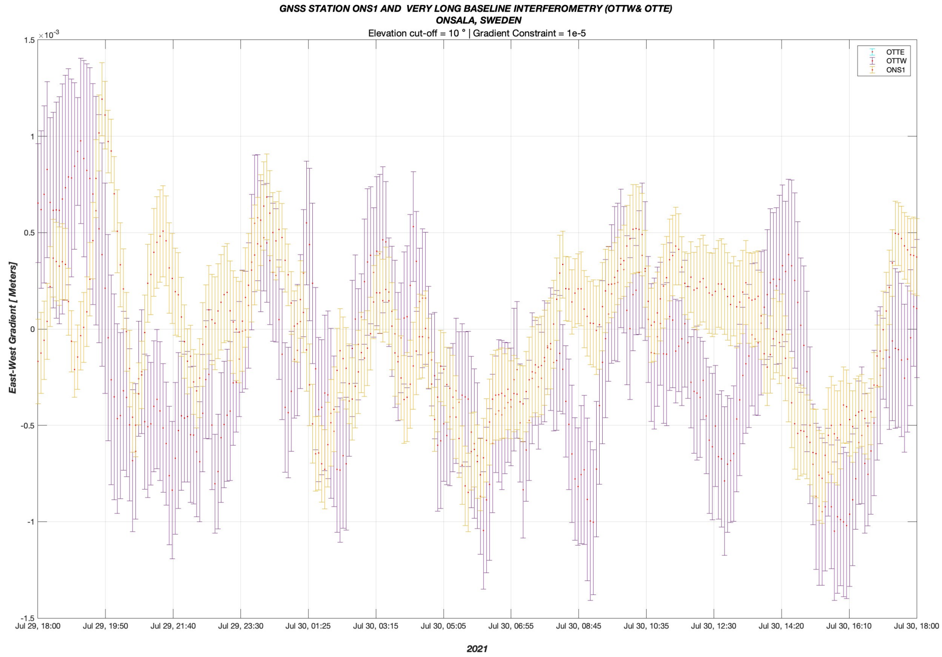

(a) East-West gradient estimated for station ONS1 and the VLBI

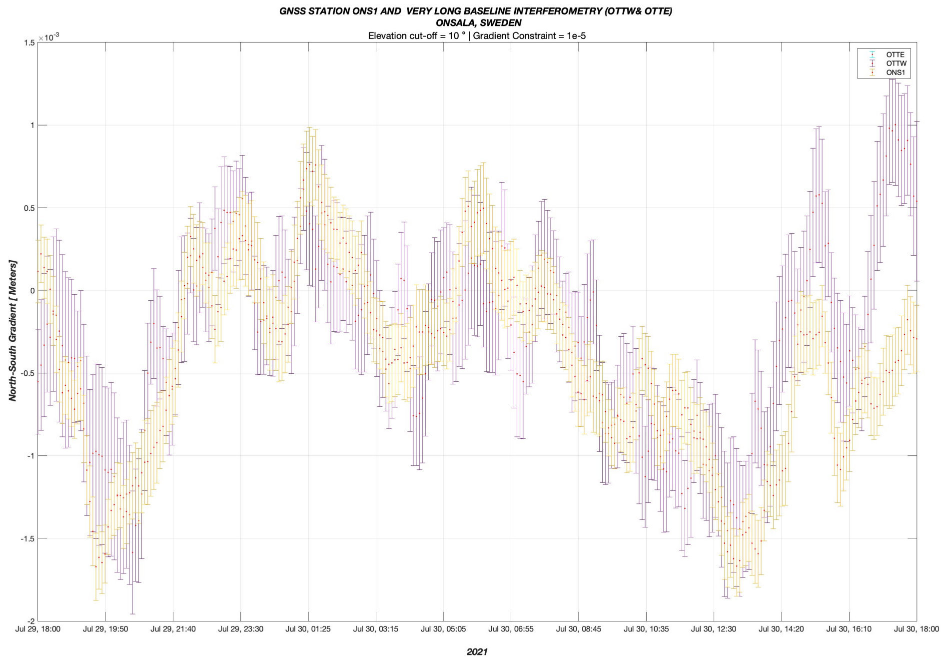

(b) North-South gradient estimated for station ONS1 and the VLBI

Figure 4.8: Gradients time series of the East-West gradient (4.8a) and North-South gradient (4.8b) estimated for station ONS0 and the VLBI (OTTE and OTTW)

The Onsala Twin Telescopes proved the limitation of the baseline constraint ($1e-5$) as the comparison projected poor results for both stations with the selected constraints (see figure 4.7 and 4.8). This is more apparent for the East-West gradients. The significant disagreement between the stations and the VLBI supports the observation that tight constraints might obstruct the performance of the software with false assumptions. Finally, the mean and RMS of the differences are available in tables 4.2 and 4.3.

4.2 Implications of Looser Gradient Constraint (5e-5)

This section presents the impacts of using a looser gradient constraint (5e-5) for the same elevation cut-off (10°). The same criteria were used, and comparisons with the WVR and VLBI were employed for the assessment.

4.2.1 Zenith Wet Delay

a ***The Water Vapor Radiometer***

Figures 4.9 and 4.10 present the estimated ZWD for ONSA and ONS1 and WVR for July 29 – 31, 2021. Although both stations are considerably different from the WVR, compared to figure 4.1 and 4.2 in the above section a slight improvement in results has been achieved.

A comparison between the mean and RMS values of the differences can be found in table 4.1a. The results prove that loosening the gradient constraint gives the software more room to include valuable observations that previously were forced to be eliminated due to the "safer" constraint.

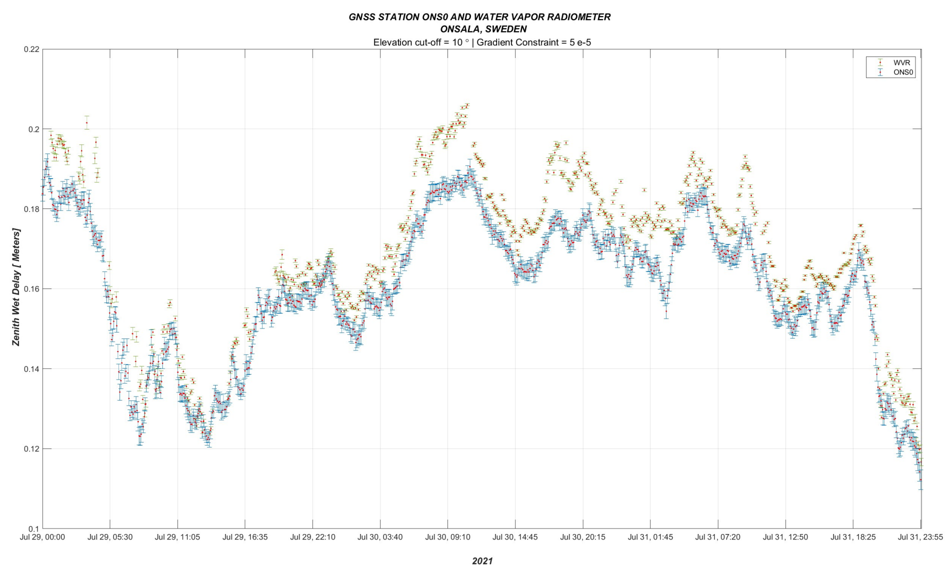

Figure 4.9: The time series of the ZWD estimated for station ONS0 and the WVR

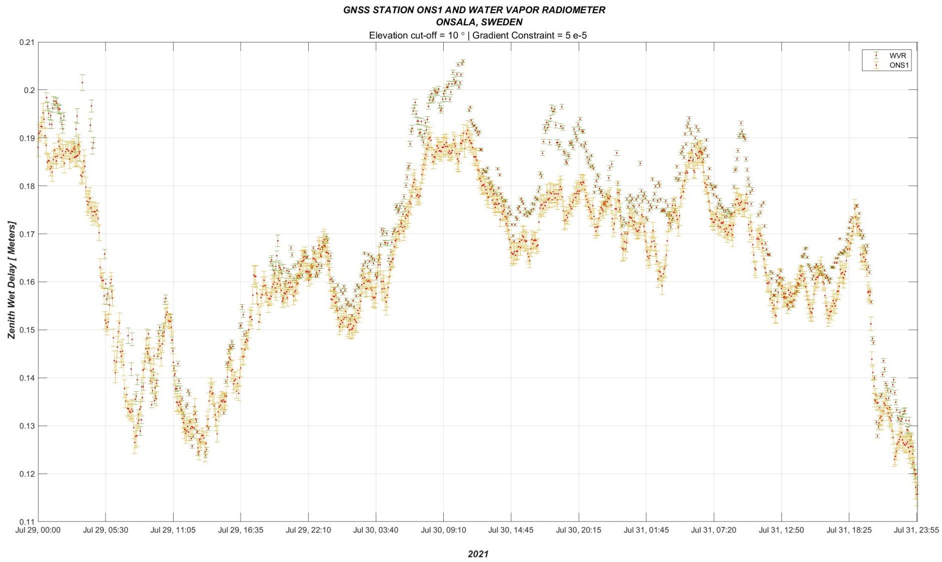

Figure 4.10: The time series of the ZWD estimated for station ONS1 and the WVR

b ***Very Long Baseline Interferometry (OTTW and OTTE)***

Similarly, the VLBI observations validate the WVR result for both stations. Therefore, figures 4.11 and 4.12 below reflect a more reasonable agreement between the two measurement methods. However, the results are better presented in table 4.1a comparing the mean and RMS values of the differences.

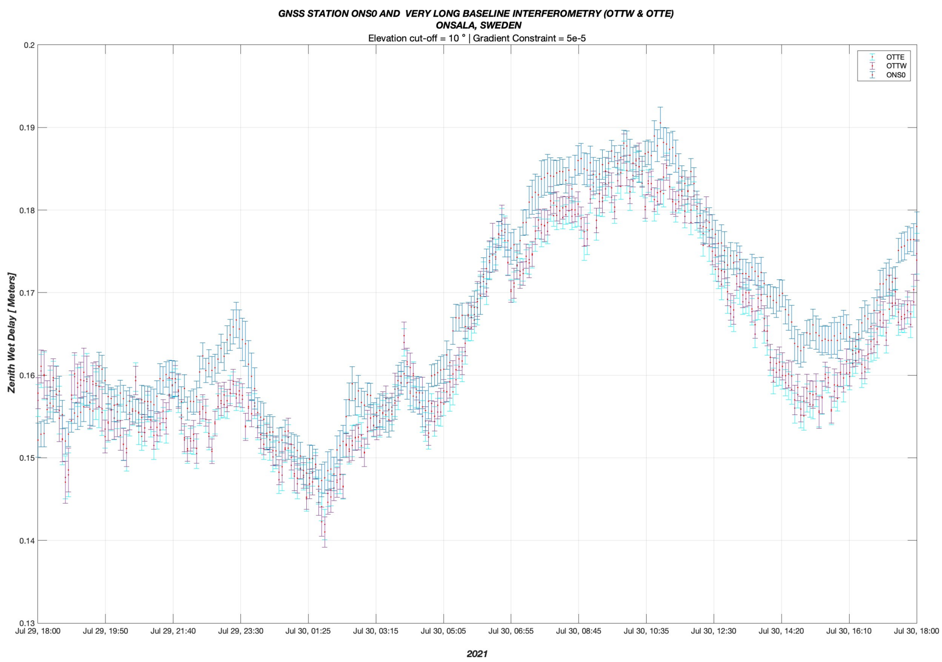

Figure 4.11: The time series of the ZWD estimated for station ONS0 and the VLBI (OTTE and OTTW)

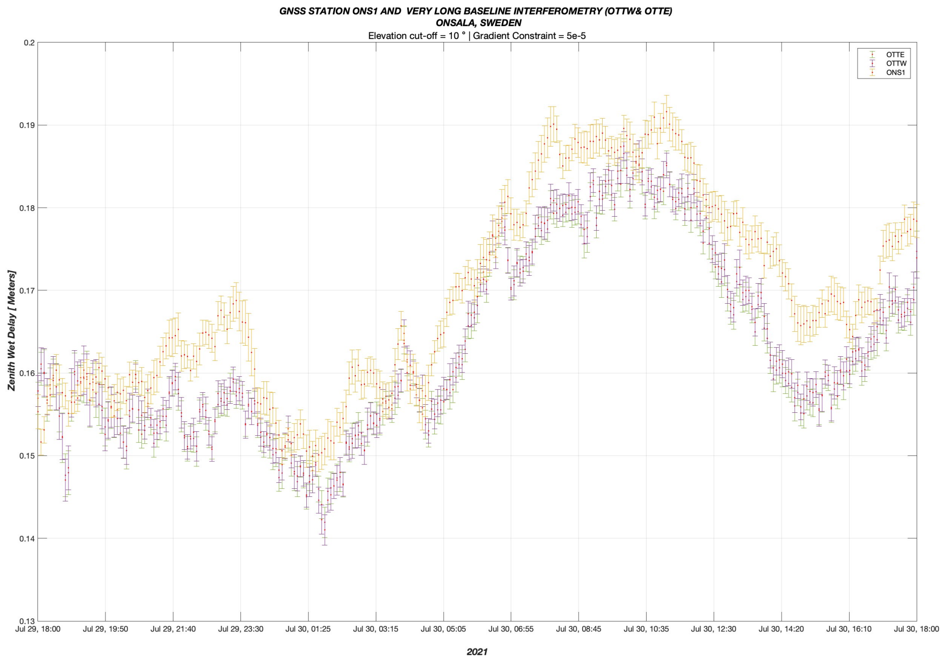

Figure 4.12: The time series of the ZWD estimated for station ONS1 and the VLBI (OTTE and OTTW)

4.2.2 Tropospheric Gradients

a ***The Water Vapor Radiometer***

The East and North gradients (figures 4.13 and 4.14) hold solid evidence that the new, i.e., looser, constraint improves the results significantly. ONSA and ONS1 observations are consistent with the WVR results. Although the uncertainty represented by the error bars is more prominent than those of the default constraint, this is a result of the looser constraint as the software is given more freedom and is no longer restricted. The mean and RMS values are presented in tables 4.2 and 4.3.

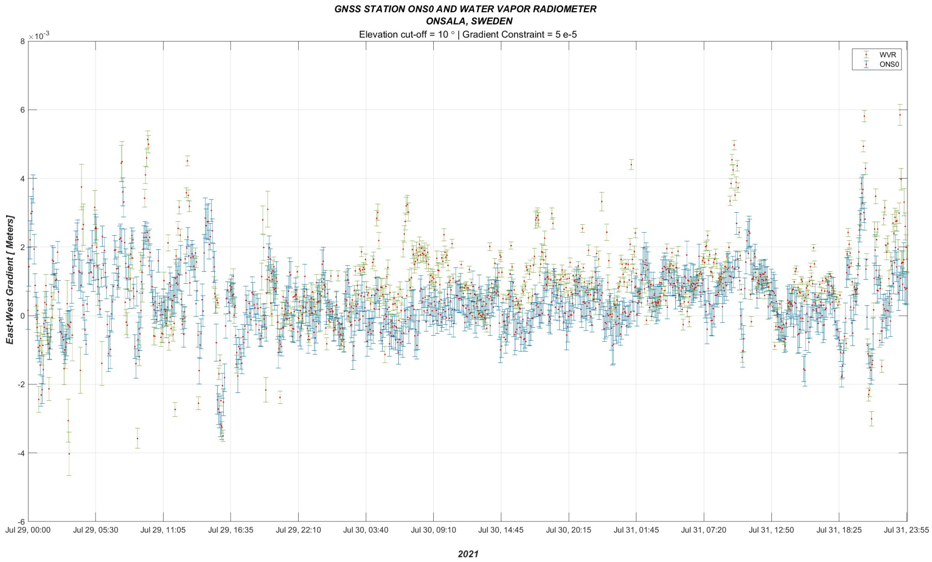

(a) East-West gradient estimated for station ONS0 and the WVR

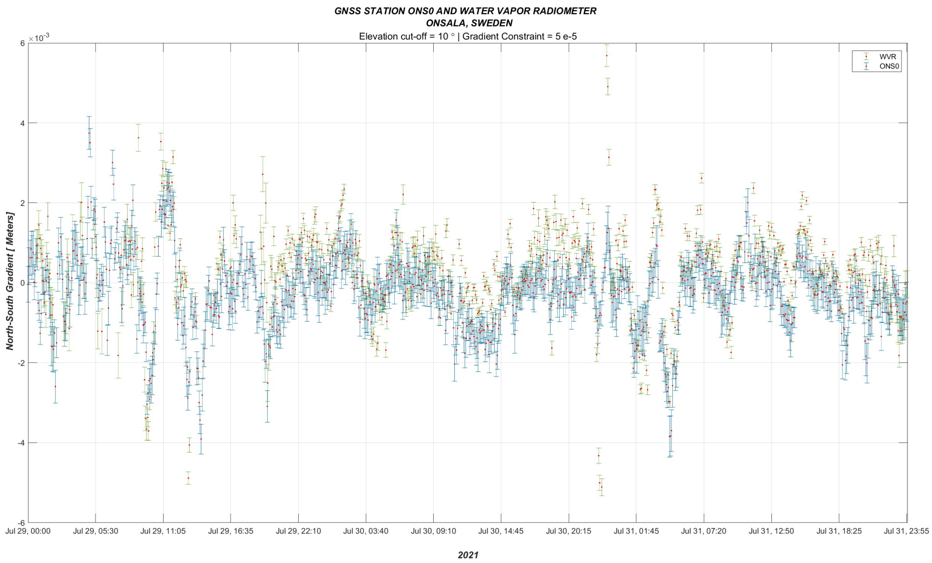

(b) North-South gradient estimated for station ONS0 and the WVR

Figure 4.13: Gradients time series of the East-West gradient (4.13a) and North-South gradient (4.13b) estimated for station ONS0 and the WVR

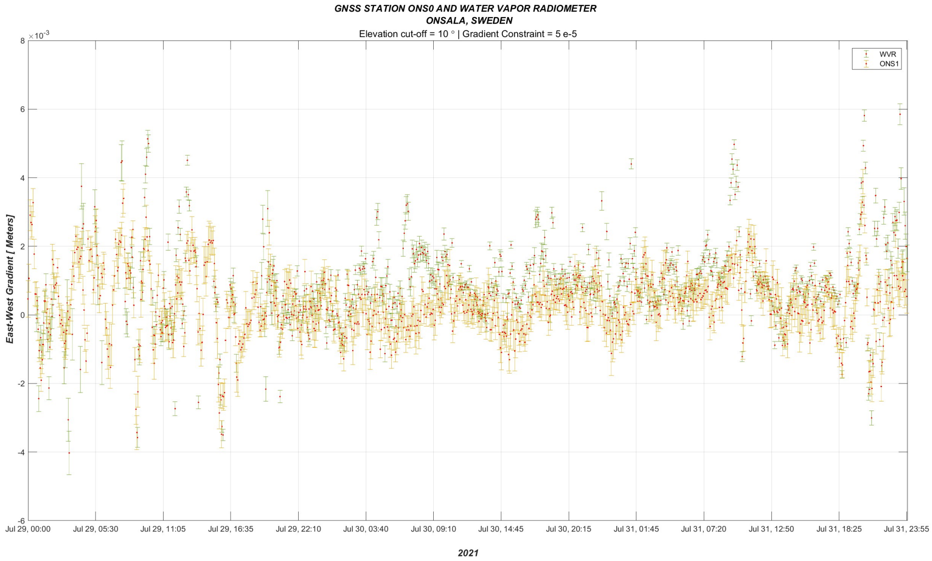

(a) East-West gradient estimated for station ONS1 and the WVR

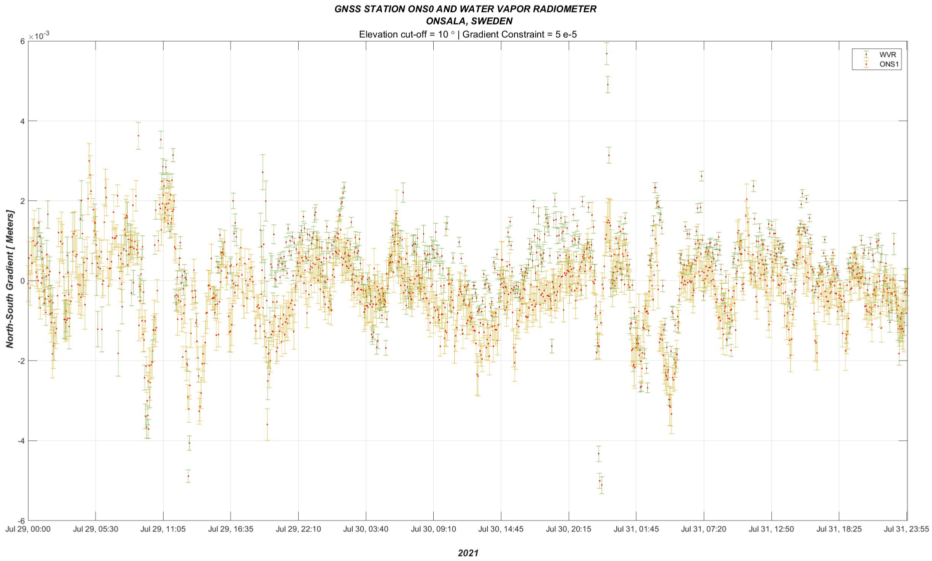

(b) North-South gradient estimated for station ONS1 and the WVR

Figure 4.14: Gradients time series of the East-West gradient (4.14a) and North-South gradient (4.14a) estimated for station ONS1 and the WVR

b ***Very Long Baseline Interferometry (OTTW & OTTE)***

Allowing Gipsy to have more freedom is significantly visible in this comparison. Unlike the ZWD case, the North (figure 4.15a) and East (figure 4.15b) for ONSA and ONS1 (figure 4.16a and 4.16b) gradients illustrate noticeable agreement. Tables 4.2 and 4.3 represents more results, more specifically the mean and RMS values.

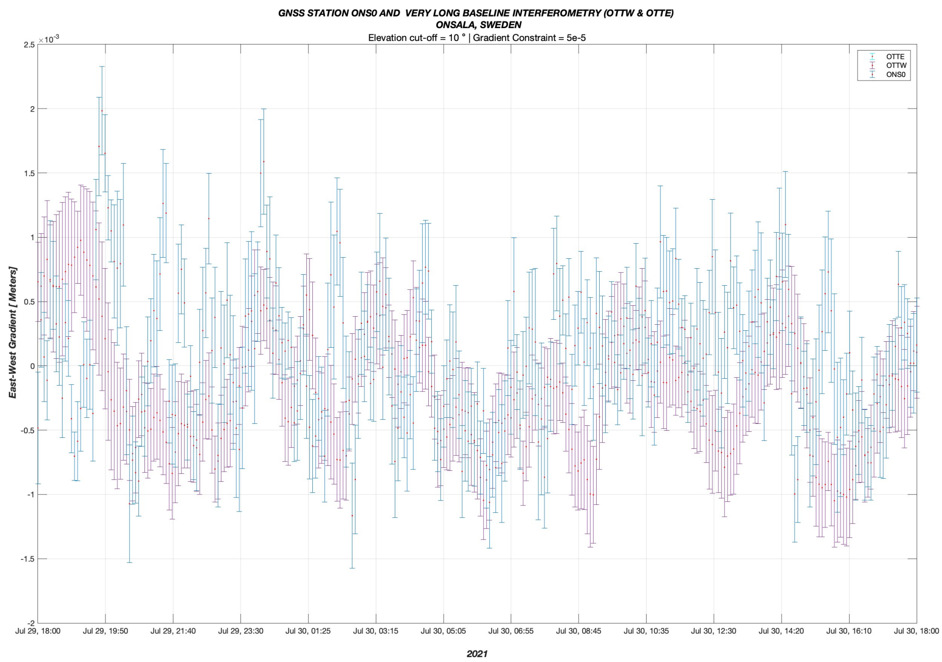

(a) East-West gradient estimated for station ONS0 and the VLBI

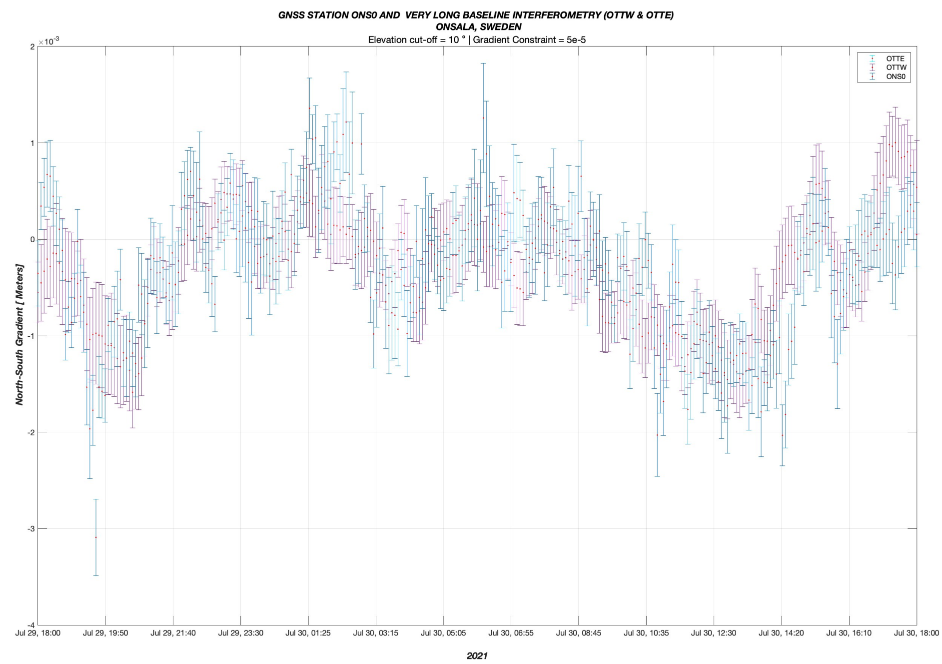

(b) North-South gradient estimated for station ONS0 and the VLBI

Figure 4.15: Gradients time series of the East-West gradient (4.15a) and North-South gradient (4.15b) estimated for station ONS0 and the VLBI (OTTE and OTTW)

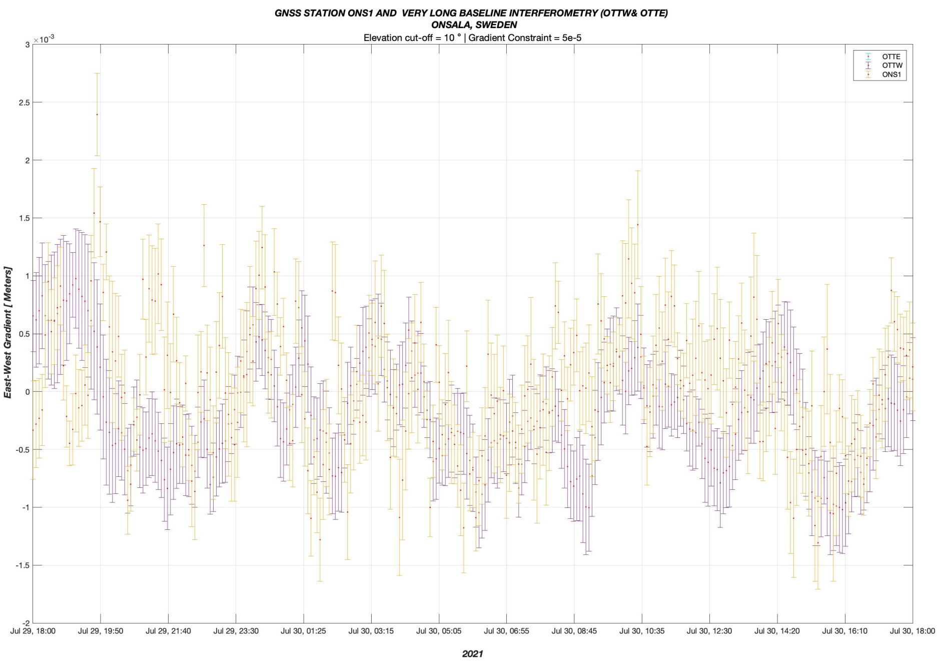

(a) East-West gradient estimated for station ONS1 and the VLBI

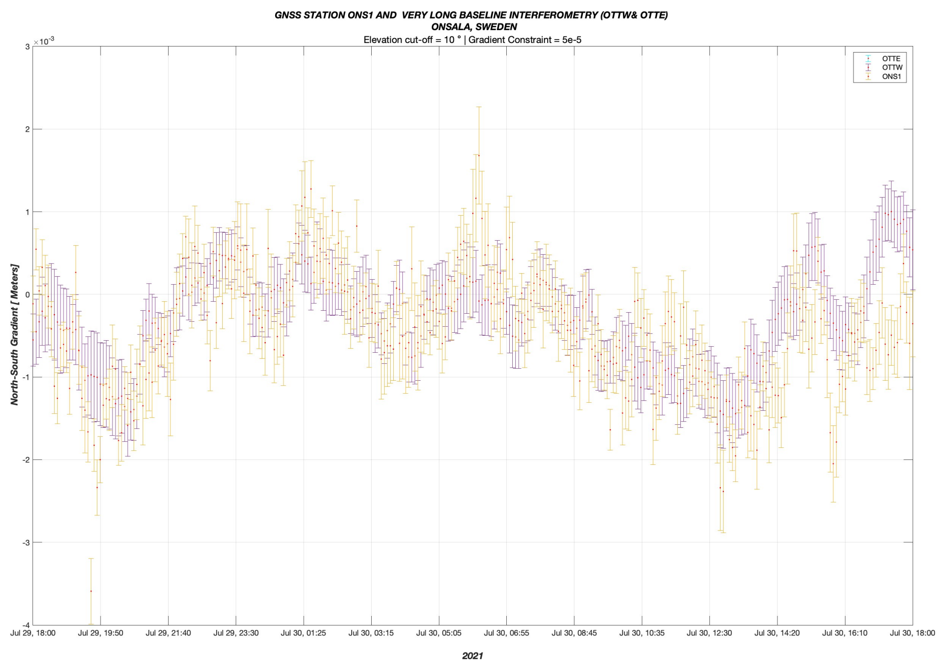

(b) North-East gradient estimated for station ONS1 and the VLBI

Figure 4.16: Gradients time series of the East-West gradient (4.16a) and North-South gradient (4.16b) estimated for station ONS0 and the VLBI (OTTE and OTTW)

Although several constraints were used during this project, both looser and tighter, the baseline and optimal values were presented in the previous section. More results are, however, available upon request.

As the gradient constraint was identified, the next step focused on testing different elevation angles and analyzing their impacts on both the ZWD and gradients.

4.3 Elevation Cut-off Assessment: 7° for the Default Constraint (1e-5)

The following subsection compares the GNSS, WVR, and VLBI results using the default gradient constraint value 1e-5, for the elevation cut-off angle 7°. Lower elevation angles allow the receivers to track the satellites for extended periods; thus, more observations will be included in the processing. However, the drawback concerns the phase ambiguity parameter for the phase pseudo-ranges as the signals will be more exposed to obstacles (blockage).

4.3.1 Zenith Wet Delay

a ***Water Vapor Radiometer***

Figures 4.17 and 4.18 present the ZWD obtained for ONSA and ONS1 compared with the WVR. The results are estimated for the 29 - 31 of July 2021. Both stations show similar results, with ONS1 following the WVR slightly better than ONSA. The difference between the stations and the WVR and its mean and RMS values can be found in table 4.1.

Moreover, no evident differences can be noticed when comparing the results for the same constraint and different angles, i.e., figures 4.1, 4.2, 4.17, and 4.18. However, the minimal differences can be detected in table 4.1 when comparing the mean and RMS.

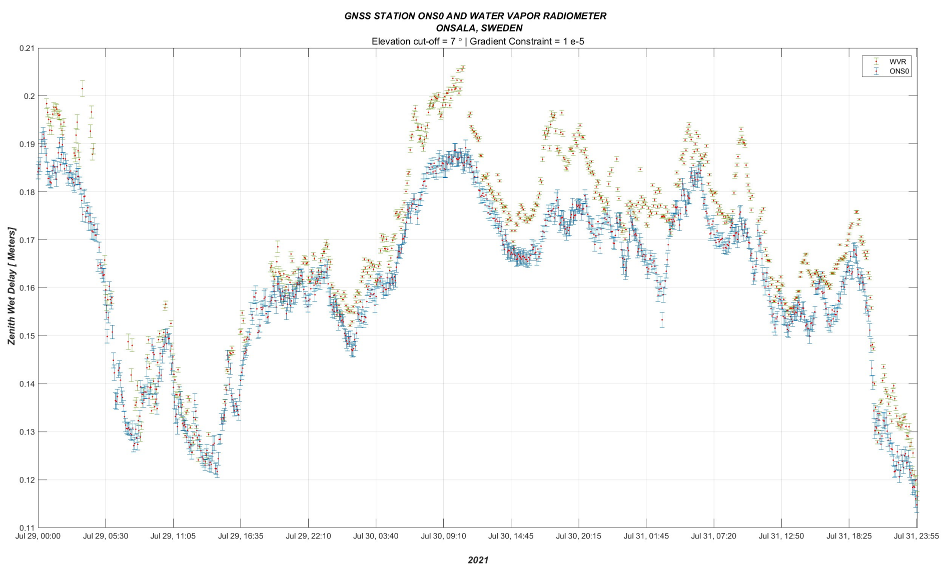

Figure 4.17: The time series of the ZWD estimated for station ONS0 and the WVR

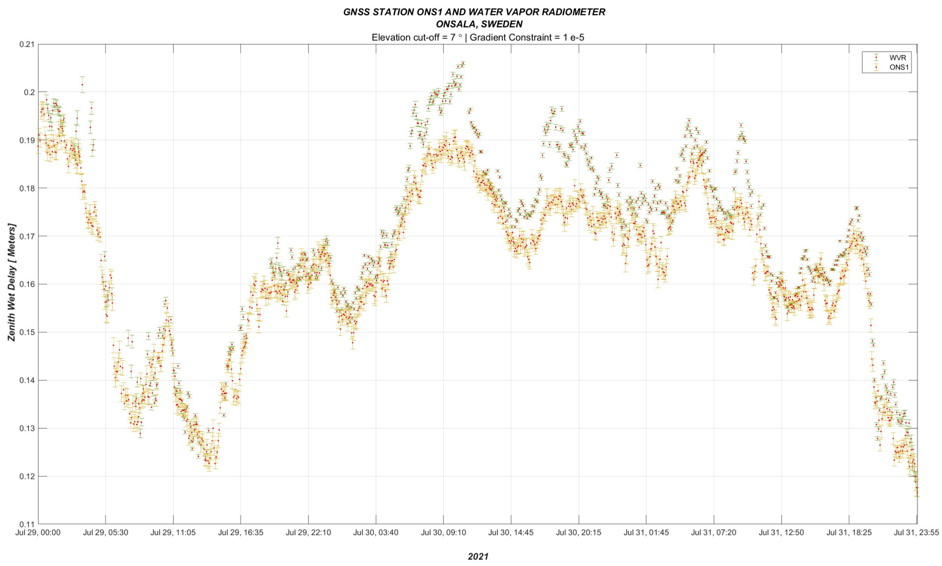

Figure 4.18: The time series of the ZWD estimated for station ONS1 and the WVR

b ***Very Long Baseline Interferometry (OTTW & OTTE)***

The 20m twin telescopes at Onsala show similar behavior, where the estimated ZWD for ONSA (4.19) and ONS1(4.20), elevation 7°, is comparable to elevation 10° for the same constraint. Nevertheless, there is a slight improvement, more likely due to more satellite measurements being included in the calculations. Moreover, a more convenient comparison is available in table 4.1.

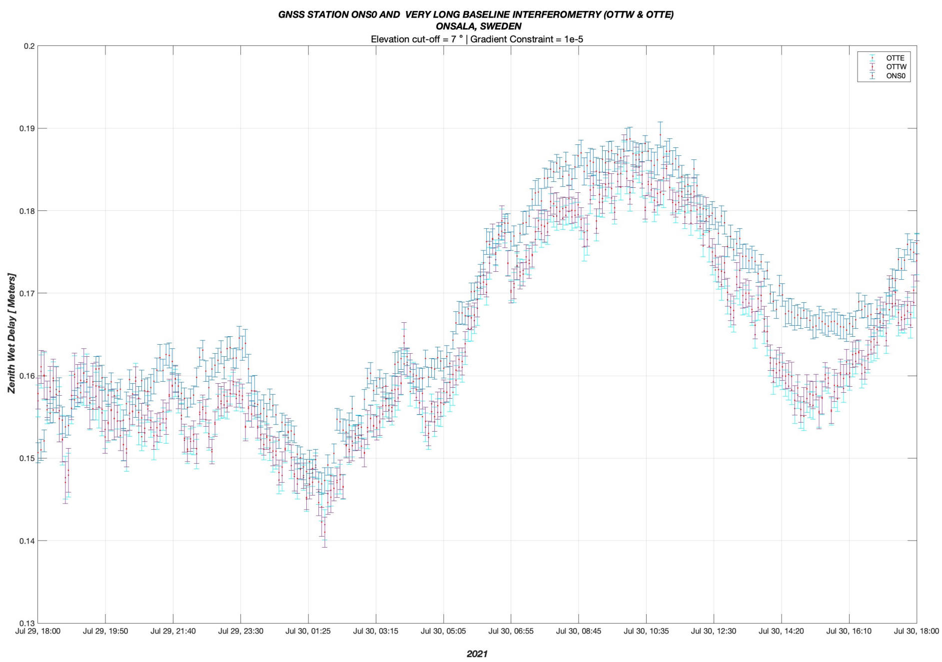

Figure 4.19: The time series of the ZWD estimated for station ONS0 and the VLBI (OTTE & OTTW)

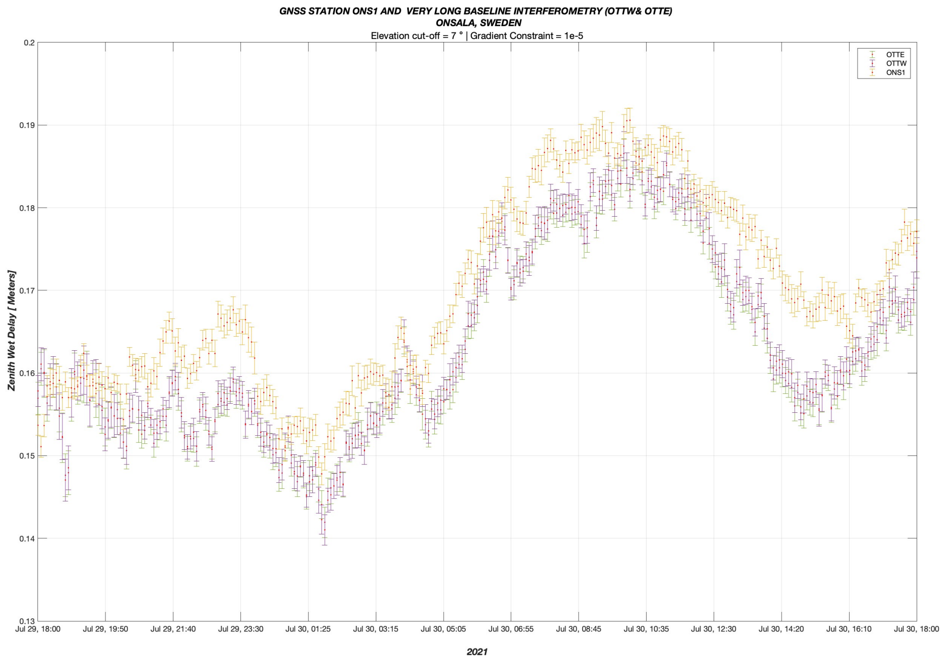

Figure 4.20: OThe time series of the ZWD estimated for station ONS1 and the VLBI (OTTE & OTTW)

4.3.2 Tropospheric Gradients

a ***Water Vapor Radiometer***

The estimated North and East gradients are presented in figures 4.21 and 4.22. for ONSA and ONS1. The results show similarities in terms of following the general trend. However, the uncertainty (error bars) is relatively lower in the 7° case than figures A.2 and 4.6.

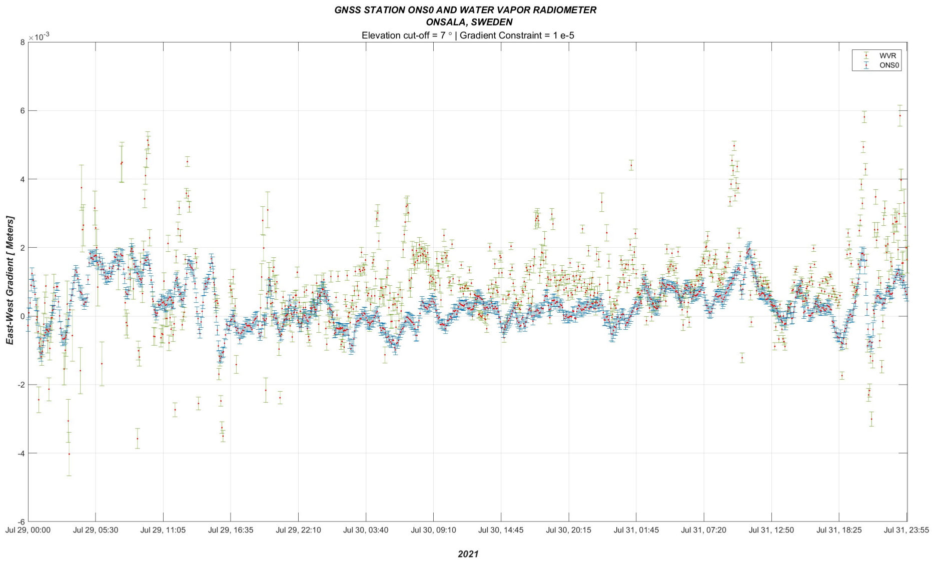

(a) East-West gradient estimated for station ONS0 and the WVR

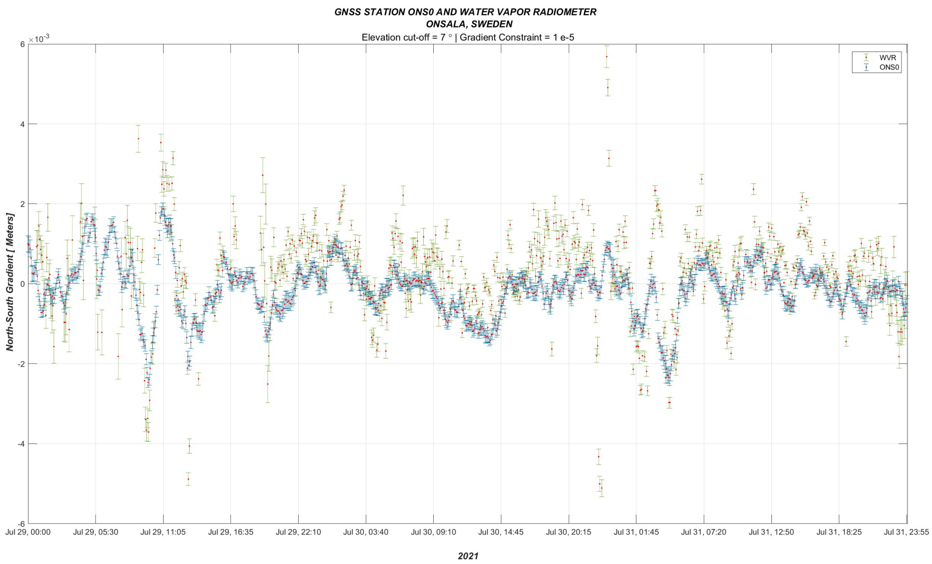

(b) North-South gradient estimated for station ONS0 and the WVR

Figure 4.21: Gradients time series of the East-West gradient (4.21a) and North-South gradient (4.21b) estimated for station ONS0 and the WVR

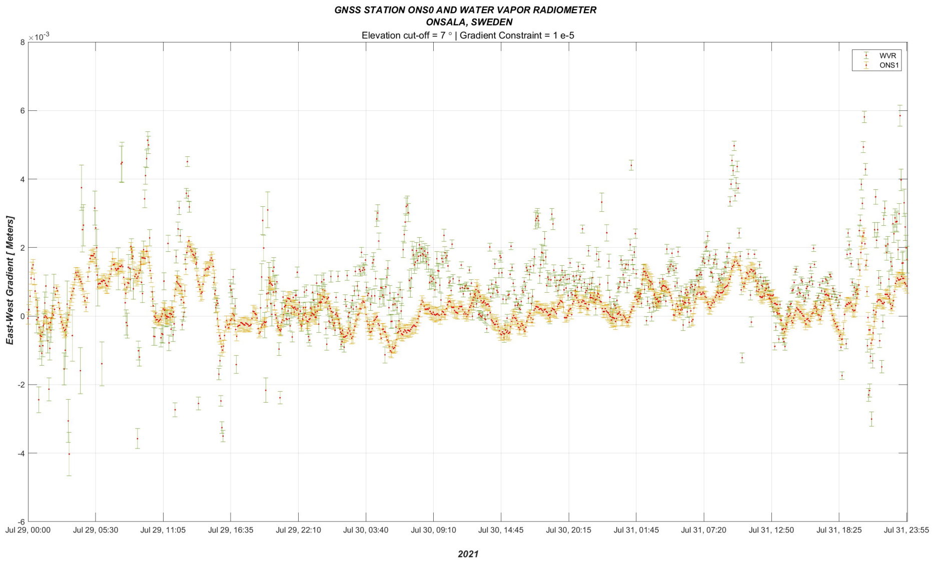

(a) East-West gradient estimated for station ONS1 and the WVR

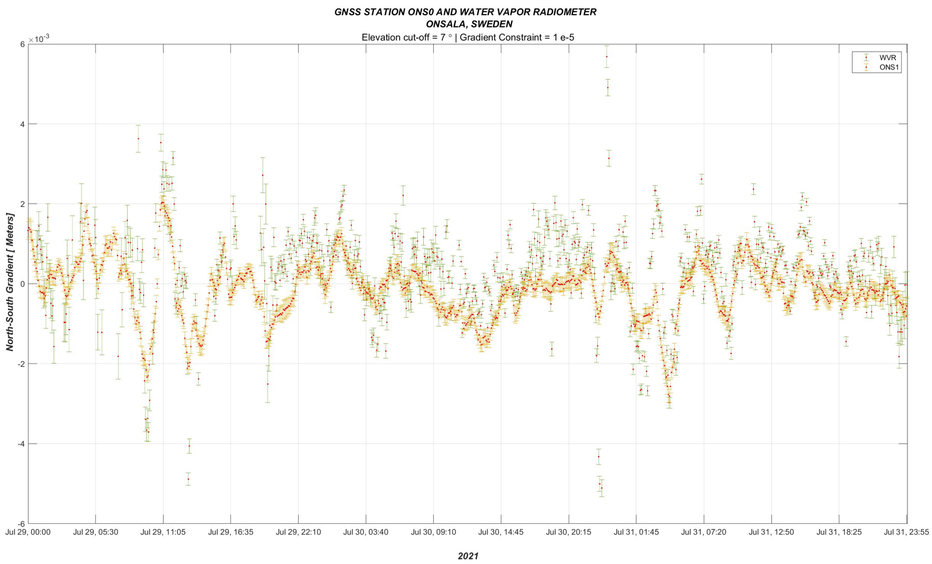

(b) North-South gradient estimated for station ONS1 and the WVR

Figure 4.22: Gradients time series of the East-West gradient (4.22a) and North-South gradient (4.22b) estimated for station ONS1 and the WVR

b *Very Long Baseline Interferometry (OTTW & OTTE)*

The VLBI East gradient estimations illustrated in figures 4.23 and 4.24 showed an insignificant change in the previous observations for both stations. On the other hand, the North gradients show an improvement relative to the previously presented configurations (4.7) and (4.8).

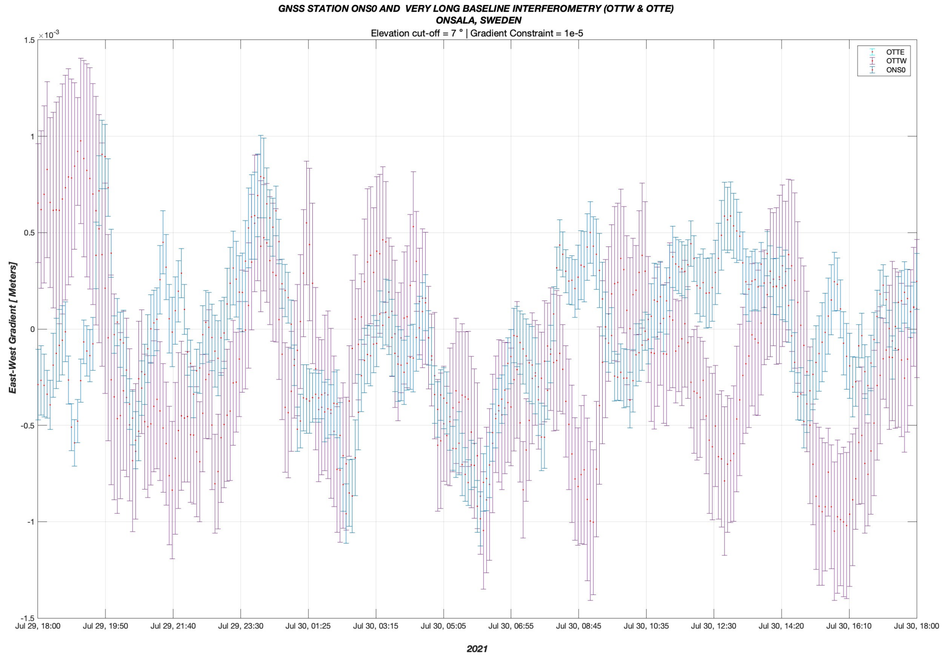

(a) East-West gradient estimated for station ONS0 and the VLBI

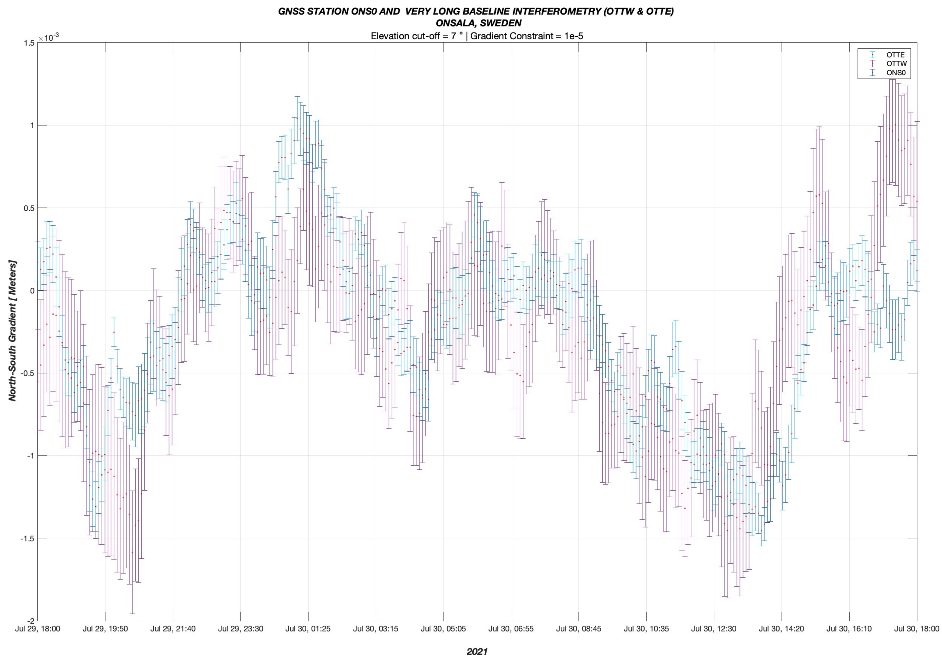

(b) North-South gradient estimated for station ONS0 and the VLBI

Figure 4.23: Gradients time series of the East-West gradient (4.23a) and North-South gradient (4.23b) estimated for station ONS0 and the VLBI (OTTE and OTTW)

(a) East-West gradient estimated for station ONS1 and the VLBI

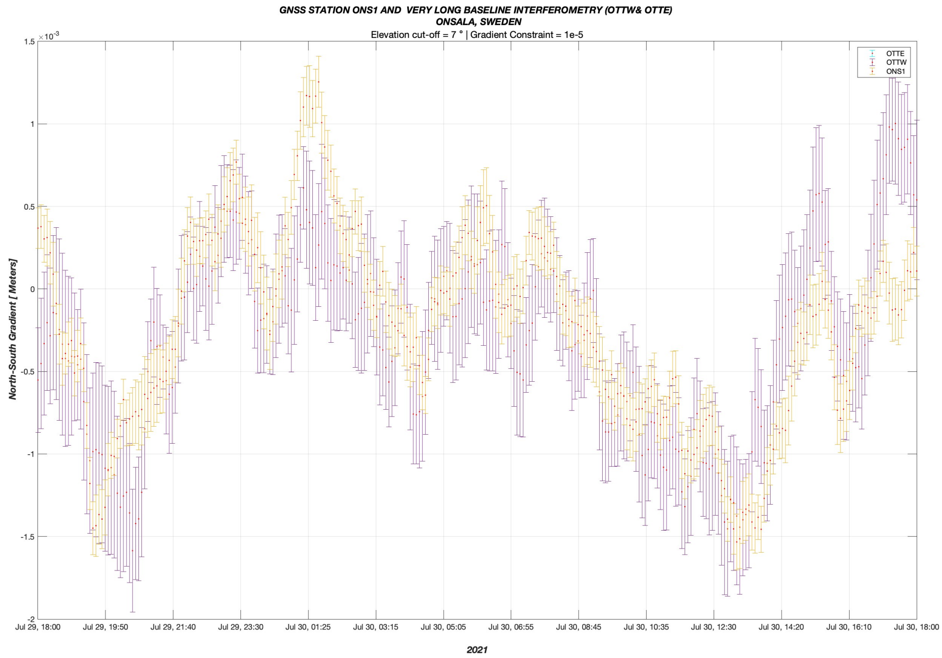

(b) North-South gradient estimated for station ONS1 and the VLBI

Figure 4.24: Gradients time series of the East-West gradient (4.24b) and North-South gradient (4.24b) estimated for station ONS1 and the VLBI (OTTE and OTTW)

4.4 The Optimal Configuration: Gradient Constraint 5e-5 and Elevation Cut-off Angle 7°

According to this project, this section presents the optimal configuration for the elevation angle and gradient constraints in the control files of the processing software (GipsyX v.1.7.), i.e., elevation cut-off 7° and gradient constraint 5e-5. The analysis is based on a careful comparison with different measurement techniques. Although all these measurement tools are equally not entirely reliable, they indicate how different constraints and processing strategies might affect the accuracy of the GNSS estimations.

4.4.1 Zenith Wet Delay

a ***Water Vapor Radiometer***

Figures 4.25 and 4.26 present the estimated ZWD obtained for ONSA and ONS1 compared with the WVR for the 29 - 31 of July 2021. As for gradient constraint 1e-5, both stations show similar results, with ONS1 following the WVR slightly better than ONSA. Refer to table 4.1 for the mean and RMS values of the difference. Worth mentioning that minor improvements are discernible relative to angle 7° and gradient constraint 1e-5 (4.17 and 4.18).

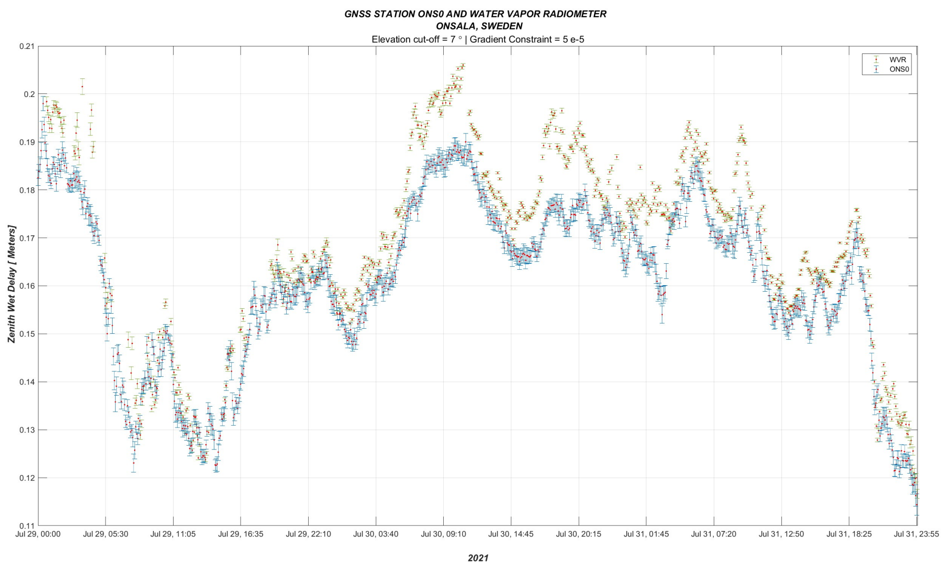

Figure 4.25: The time series of the ZWD estimated for station ONS0 and the WVR

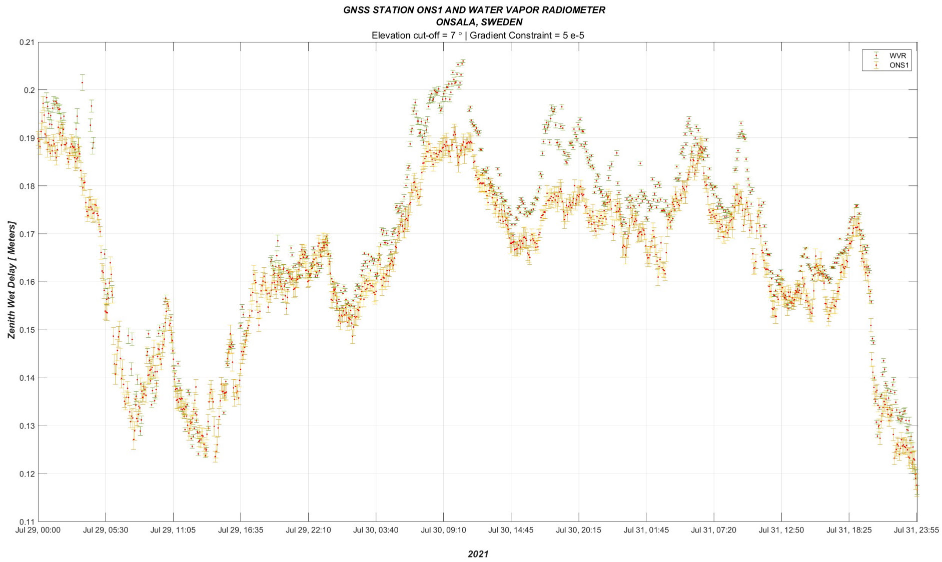

Figure 4.26: The time series of the ZWD estimated for station ONS1 and the WVR

b ***Very Long Baseline Interferometry (OTTW & OTTE)***

Figure 4.27 and 4.28 compare the time series of the ZWD estimated for ONSA and ONS1 with the VLBI estimations. No evident difference from gradient constraint 1e-5 is noticeable. However, table 4.1 provides more elaboration proving that a slight improvement has been achieved.

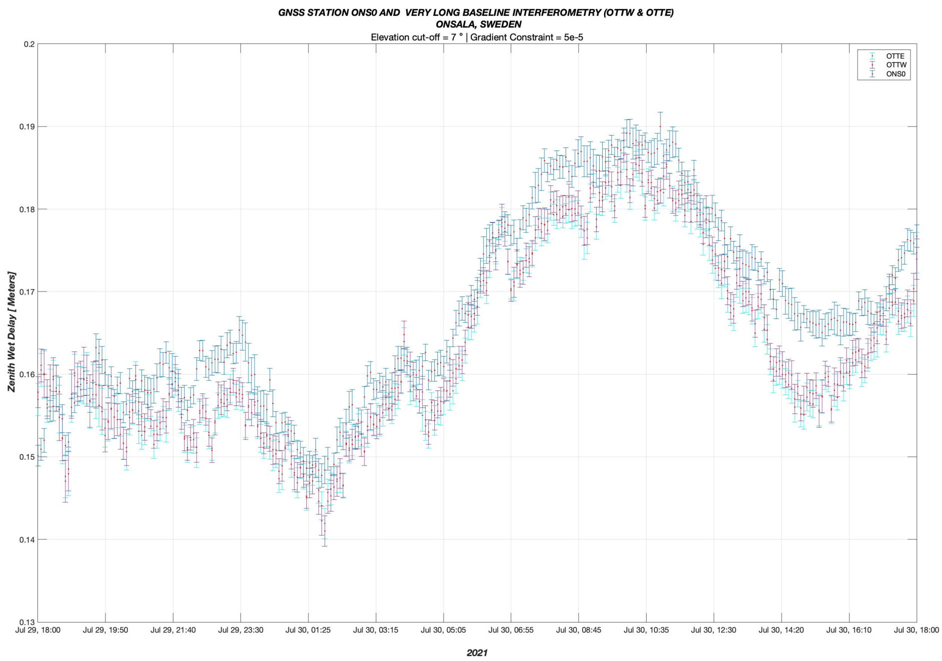

Figure 4.27: The time series of the ZWD estimated for station ONS0 and the VLBI (OTTE & OTTW)

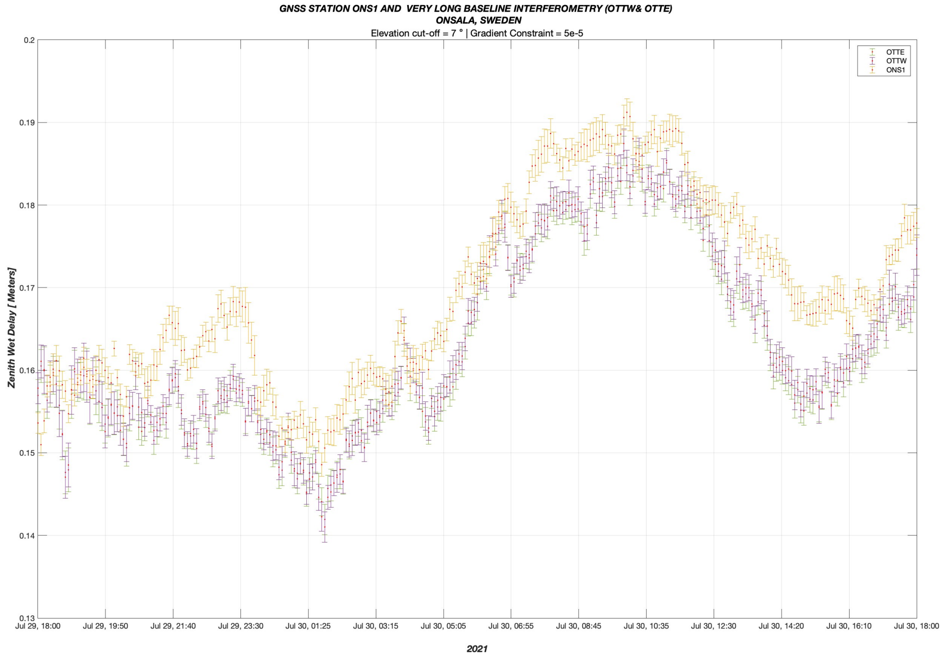

Figure 4.28: The time series of the ZWD estimated for station ONS1 and the VLBI (OTTE & OTTW)

4.4.2 Tropospheric Gradients

a ***Water Vapor Radiometer***

Lastly, a comparison between the time series of the estimated ZWD for GNSS stations ONSA (4.29) and ONS1 (4.30) and the VLBI is presented in this section. Compared to the default constraint (1e-5), 5e-5 provides a noticeable improvement for the same elevation angle (4.21 & 4.22). On the other hand, the improvement relative to the estimations using the baseline elevation angel (10°) is less obvious. It requires a closer look into the mean differences between the two techniques and RMS values in tables 4.2 and 4.3.

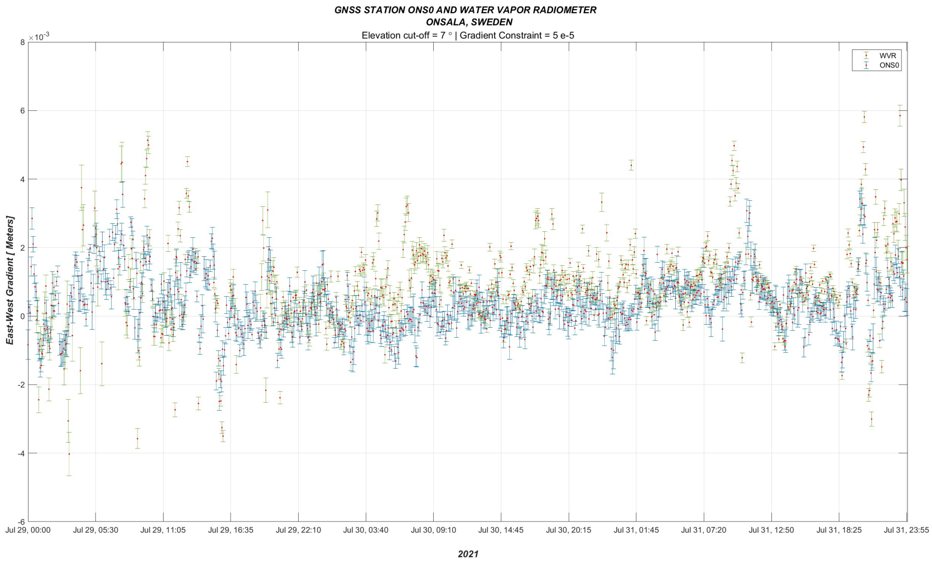

(a) East-West gradient estimated for station ONS0 and the WVR

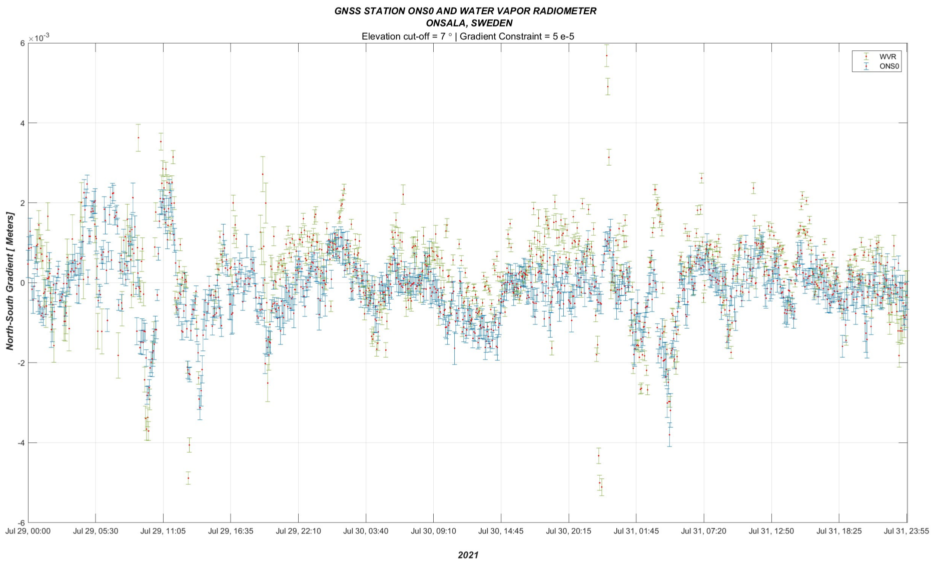

(b) North-South gradient estimated for station ONS0 and the WVR

Figure 4.29: Gradients time series of the East-West gradient (4.29a) and North-South gradient (4.29b) estimated for station ONS0 and the WVR

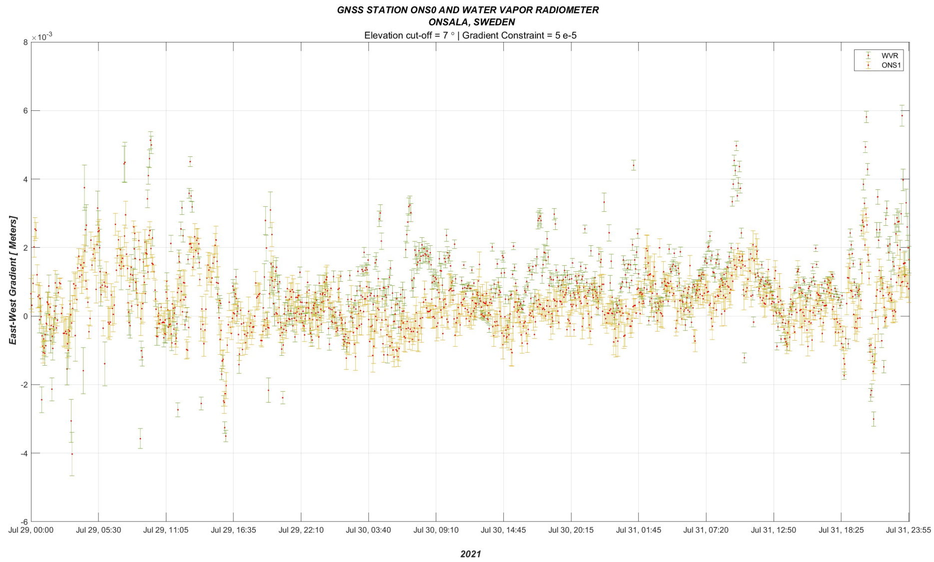

(a) East-West gradient estimated for station ONS1 and the WVR

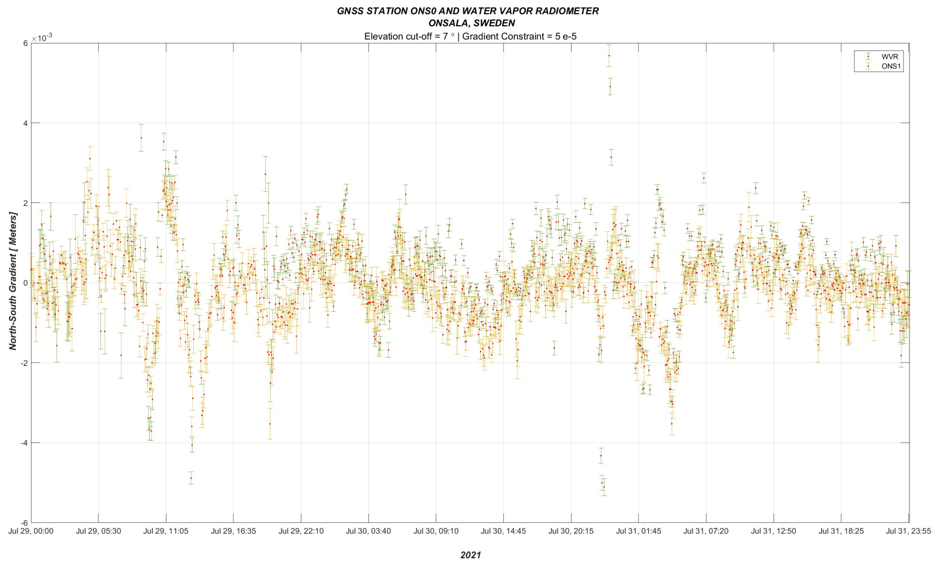

(b) North-South gradient estimated for station ONS1 and the WVR

Figure 4.30: Gradients time series of the East-West gradient (4.30a) and North-South gradient (4.30b) estimated for station ONS1 and the WVR

b ***Very Long Baseline Interferometry (OTTW & OTTE)***

Figures 4.31 and 4.32 show the East and North gradient of ONSA and ONS1 compared with the VLBI. The plotted estimations reflect a clear improvement compared to the tighter constraint for the same elevation cut-off. Loosening the gradient constraint has significantly enhanced the alignment between the GNSS gradient estimations and the VLBI results. The error bars are prominent. However, this does not necessarily imply worse results. The tighter constraints, 1e-5, might result in seamless plots due to the large data erasure during the processing.

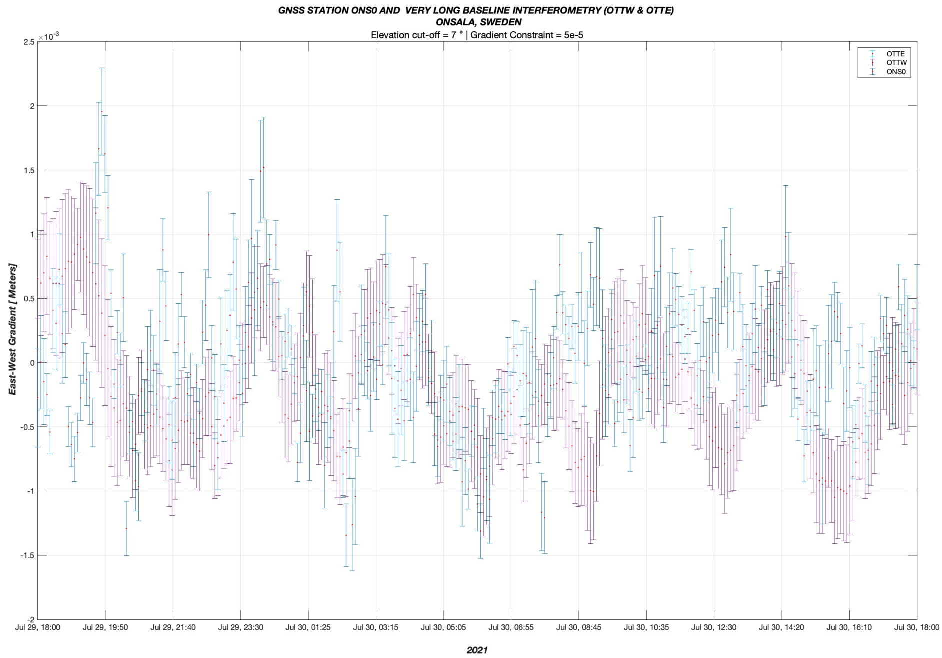

(a) East-West gradient estimated for station ONS0 and the VLBI

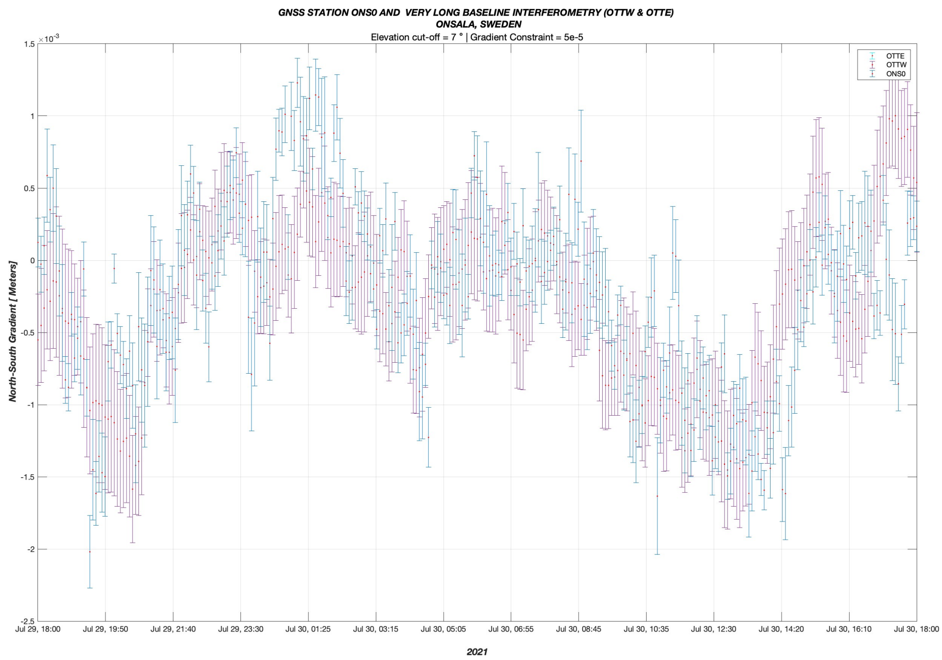

(b) North-South gradient estimated for station ONS0 and the VLBI

Figure 4.31: Gradients time series of the East-West gradient (4.31a) and North-South gradient (4.31b) estimated for station ONS1 and the VLBI (OTTE and OTTW)

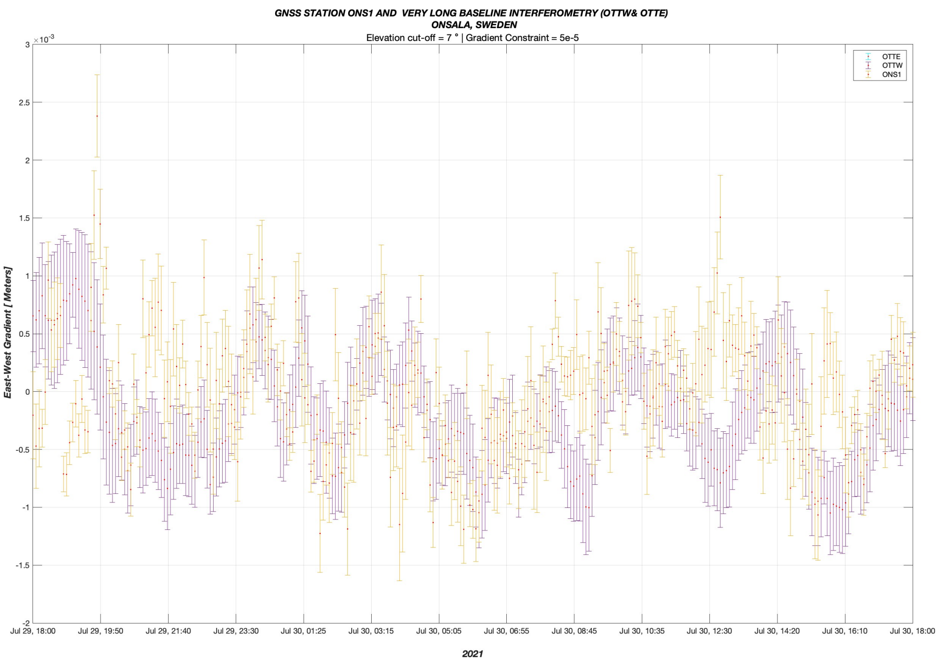

(a) East-West gradient estimated for station ONS1 and the VLBI

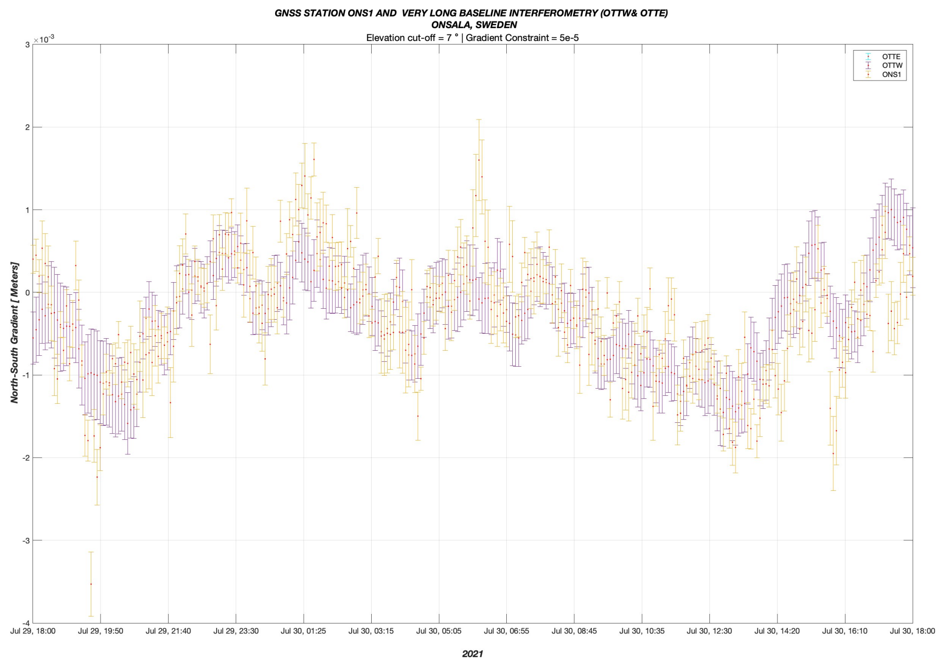

(b) North-South gradient estimated for station ONS1 and the VLBI

Figure 4.32: Gradients time series of the East-West gradient (4.32a) and North-South gradient (4.32b) estimated for station ONS1 and the VLBI (OTTE and OTTW)

Comparing to figures 4.15 and 4.16 for elevation 10° and gradient constraint 5e-5 estimates is more challenging. However, since both seem to show similar results, determining the superior elevation cut-off angle is unfortunately not straightforward. The differences, their mean, and RMS values could facilitate such a challenge. Thus, these results are also presented in table 4.2 and 4.3.

4.5 Concluding Discussion and Final Remarks

Table 4.1 presents a clear improvement in results relative to WVR for both ONSA and ONS1. Elevation 7° with gradient constraint $5e-5$ decreases the mean and RMS values of the differences between the two measurements, however, with a few exceptions. The RMS for ONS1 is the lowest for the baseline configuration, elevation 10°, and gradient constraint 1e-5. In figures 4.1 and 4.2, though, the GNSS estimations follow a very neat pattern for gradient constraint 1e-5. Nevertheless, the agreement with the WVR is low. On the other hand, in figures 4.9 and 4.10 for gradient constraints 5e-5, the GNSS estimations follow the WVR estimations much more closely. One likely reason for this might be that the 1e-5 constraint is too tight; thus, it restricts GipsyX, resulting in large amounts of data being deleted.

The mean and RMS values of ZWD for the VLBI comparison equally show poor results. Here angle 7° consistently results in larger mean and RMS values, with a few exceptions. Once again, this might partially result from the too tight gradient constraint of 1e-5. Moreover, the VLBI comparisons in this project are less reliable due to the limited amount of data and the variations in the measurement epochs compared to the GNSS. Utmost care was taken to align the GNSS and VLBI estimations properly; however, misalignment errors are unavoidable.

The VLBI data was only available for one day, so the values presented here should be considered a reference at best, regardless of which point one aims to prove. Should a longer period of data been available, the results might have looked different.

Table 4.1: Comparison between the ZWD for different measurement techniques

Elevation angle	Grad const [km/s^2]	WVR mean [m]	WVR RMS [m]	VLBI mean [m]	VLBI RMS [m]
10 °	1e-5	-8.720e-03	9.933e-03	3.754e-03	4.958e-03
	5e-5	-8.761e-03	9.938e-03	3.778e-03	4.962e-03
7 °	1e-5	-7.712e-03	9.312e-03	4.557e-03	5.544e-03
	5e-5	-7.643e-03	9.240e-03	4.678e-03	5.655e-03

(a) The mean and RMS of the ZWD differences for ONSA, WVR, and VLBI

Elevation angle	Grad const [km/s^2]	WVR mean [m]	WVR RMS [m]	VLBI mean [m]	VLBI RMS [m]
10 °	1e-5	–5.895e-03	7.630e-03	6.279e-03	7.263e-03
	5e-5	-5.778e-03	7.594e-03	6.325e-03	7.334e-03
7 °	1e-5	-5.768e-03	7.741e-03	6.426e-03	7.318e-03
	5e-5	-5.590e-03	7.614e-03	6.466e-03	7.364e-03

(b) The mean and RMS of the ZWD differences for ONS1, WVR, and VLBI

It is also important to point out that potential constraints used for the VLBI processing are unknown. Hence, the accuracy of these comparisons is questionable. It is important to remember that neither the WVR nor the VLBI are perceived to show the absolute truth. Therefore, these outliers do not necessarily prove that the calibration did not improve the accuracy of the estimations.

By referring to the figures in the section 4, improvement is in agreement, and alignment is almost certain.

Tables 4.2 and 4.3 show the east and north gradients' comparisons, respectively. The mean and RMS values are generally worse for angle 7° and gradient constraint 5e-5. However, recalling the figures for gradient constraint 1e-5, this behavior may be explained by the tightness of this constraint. As illustrated in the figures of elevation cut-off 7°, this value consistently produces smaller error bars than when angle 10° is used. So even though the mean and RMS for 7° and gradient constraint 5e-5 is often larger than those of angle 10° and 5e-5 in table 4.1 , 4.2, and 4.3, the smaller error bars indicate a smaller uncertainty, hence a larger accuracy for the estimates obtained for the selected optimal combination.

Table 4.2: Comparison between the East-West gradients for different measurement techniques

Elevation angle	Grad const [km/s^2]	WVR mean [m]	WVR RMS [m]	VLBI mean [m]	VLBI RMS [m]
10 °	1e-5	-5.776e-04	1.226e-03	2.231e-04	5.206e-04
	5e-5	-5.518e-04	1.195e-03	2.622e-04	6.852e-04
7 °	1e-5	-6.262e-04	1.256e-03	1.514e-04	5.695e-04
	5e-5	-5.831e-04	1.235e-03	1.862e-04	6.539e-04

(a) The mean and RMS of the differences for ONSA, WVR, and VLBI

Elevation angle	Grad const [km/s^2]	WVR mean [m]	WVR RMS [m]	VLBI mean [m]	VLBI RMS [m]
10 °	1e-5	-6.120e-04	1.242e-03	1.778e-04	4.936e-04
	5e-5	-6.049e-04	1.211e-03	2.351e-04	6.554e-04
7 °	1e-5	-6.088e-04	1.254e-03	1.473e-04	5.600e-04
	5e-5	-5.951e-04	1.253e-03	1.821e-04	6.475e-04

(b) The mean and RMS of the differences for ONS1, WVR, and VLBI

Table 4.3: Comparison between the North-South gradients for different measurement techniques

Elevation angle	Grad const [km/s^2]	WVR mean [m]	WVR RMS [m]	VLBI mean [m]	VLBI RMS [m]
10 °	1e-5	-5.251e-04	1.040e-03	3.347e-06	3.768e-04
	5e-5	-5.600e-04	1.070e-03	-6.261e-06	5.356e-04
7 °	1e-5	-4.641e-04	1.035e-03	7.547e-05	4.194e-04
	5e-5	-4.692e-04	1.080e-03	5.487e-05	5.170e-04

(a) The mean and RMS of the differences for ONSA, WVR, and VLBI

Elevation angle	Grad const [km/s^2]	WVR mean [m]	WVR RMS [m]	VLBI mean [m]	VLBI RMS [m]
10 °	1e-5	-5.816e-04	1.063e-03	-1.320e-04	4.416e-04
	5e-5	-5.956e-04	1.093e-03	-1.410e-04	6.197e-04
7 °	1e-5	-4.753e-04	1.022e-03	6.496e-05	3.799e-04
	5e-5	-5.045e-04	1.061e-03	6.530e-06	5.619e-04

(b) The mean and RMS of the differences for ONS1, WVR, and VLBI

Finally, table 4.5 shows the mean and RMS of the difference for ONSA and ONS1, using the different calibration values. In this table, angle 7° with constraint 1e-5 has the lowest mean and RMS values. Nevertheless, as argued before, this constraint appears considerably tight, resulting in cleaner-looking results, however more unreliable. Angle 7° with constraint 5e-5 overall delivers the second-lowest values. The few exceptions are for the north gradient. The reason behind this is unclear. However, it is not unlikely that the east and north gradients benefit differently from the configurations. In appendix 5, ONSA and ONS1 are plotted together for the different combinations. Thus, combined with the values in table 4.5, angle 7° and constraint 5e-5 seem the most accurate for stations ONSA and ONS1.

Table 4.4: Comparison of the estimated mean, and RMS of the Zenith Delays differences between ONS0 & ONS1 for the 29th to 31th of July 2021

Elevation angle	Grad const [km/s^2]	Zenith Total Delay		Zenith Wet Delay	
		mean [m]	RMS [m]	mean [m]	RMS [m]
10 °	1e-5	-2.82e-03	3.44e-03	-2.82e-03	3.44e-03
	5e-5	-3.03e-03	3.49e-03	-3.03e-03	3.49e-03
7 °	1e-5	-2e-03	2.88e-03	-2e-03	2.88e-03
	5e-5	-2.15e-03	3e-03	-2.15e-03	3e-03

Table 4.5: Comparison of the estimated mean, and RMS of the gradients differences between ONS0 & ONS1 for the 29th to 31th of July 2021

Elevation angle	Grad const [km/s^2]	North-South Gradient		East-West Gradient	
		mean [m]	RMS [m]	mean [m]	RMS [m]
10 °	1e-5	5.47e-05	2.57e-04	-2.82e-03	3.44e-03
	5e-5	2.17e-05	4.9e-04	-3.03e-03	3.49e-03
7 °	1e-5	4.44e-06	2.9e-04	-2e-03	2.88e-03
	5e-5	2.54e-05	5.1e-04	-2.15e-03	3e-03

To sum up, lowering the elevation cut-off angle from 10° to 7° decreases the error bars in the estimations, making their uncertainty lower. Furthermore, changing the gradient constraint from 1e-5 to 5e-5, thus loosening the tightness, allows GipsyX to include more measurements in the calculations, decreasing data elimination. It would, however, be of interest to continue these tests to find the most suitable calibration combinations for each station at OSO.

Table 4.1, 4.2, 4.3, and 4.5 proves that no specific combination of angle and gradient constraint makes the ultimate strategy. An important point to keep in mind is that Onsala's main station ONSA is not calibrated. Therefore, the previous section utilizes the antenna models provided in the software.

4.6 Verification Strategy: International Stations

As mentioned in table 3.1, different international stations were processed using the gradient constraint, 5e-5. The reason is to verify the optimality of the chosen constraint for other environments. In addition, the selected stations were processed for typical elevation cut-off angles, more specifically, 3°, 5°, 7°, and 10°. However, elevation 3° was not considered in the process, because it proved to have significantly poorer results.

The examination criteria mainly focused on assessing the consistency of results for different stations located in the same geographical area. This comparison method means ignoring the mutual error that might affect all stations, for example, satellite orbits and clock data. More elaboration is presented in the following subsections.

4.6.1 Zenith Total Delay

First, the Goddard stations are positioned in fairly good locations, and their antennas are of different types. Figure 4.33 presents the ZTD results for the stations, GODE, GODN, and GODS, in Greenbelt, USA, for 29 - 31 July 2021. It was evident that compared to 5°, elevations 7° and 10° reflect the best results. However, elevation 7° showed better consistency and uncertainty levels. The figures of the 10° results can be found in appendix C.

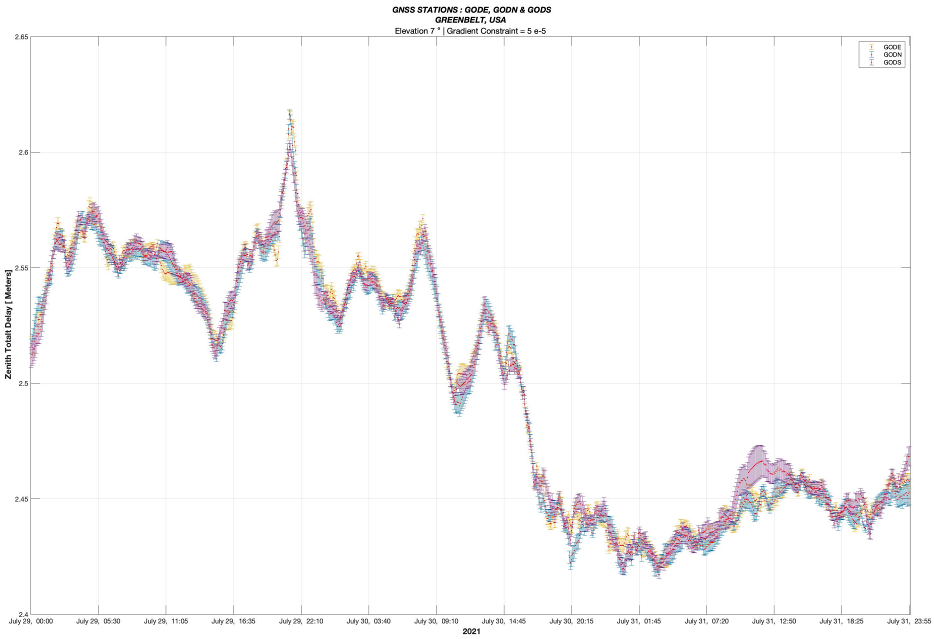

Figure 4.33: The time series of the ZTD estimated for the Goddard stations. Elevation cut-off: 7°

Unlike the Goddard stations, KOKV, and KOKB, the international stations in Kokee Park, Waimea, Hawaii, showed poor results for the examined angles, i.e., centimeter level uncertainty, as indicated in figure 4.34a below.

Our investigations showed that the stations are surrounded by big telescopes and vegetation that might act as reflecting surfaces, causing multi-path. Another observation, particularly for KOKV, is that the receiver is similar to the OTT receivers, which showed comparable behavior. Therefore, the immediate logical step was to exclude the Russian system (GLONASS) that deleted many GPS carrier-phase observables.

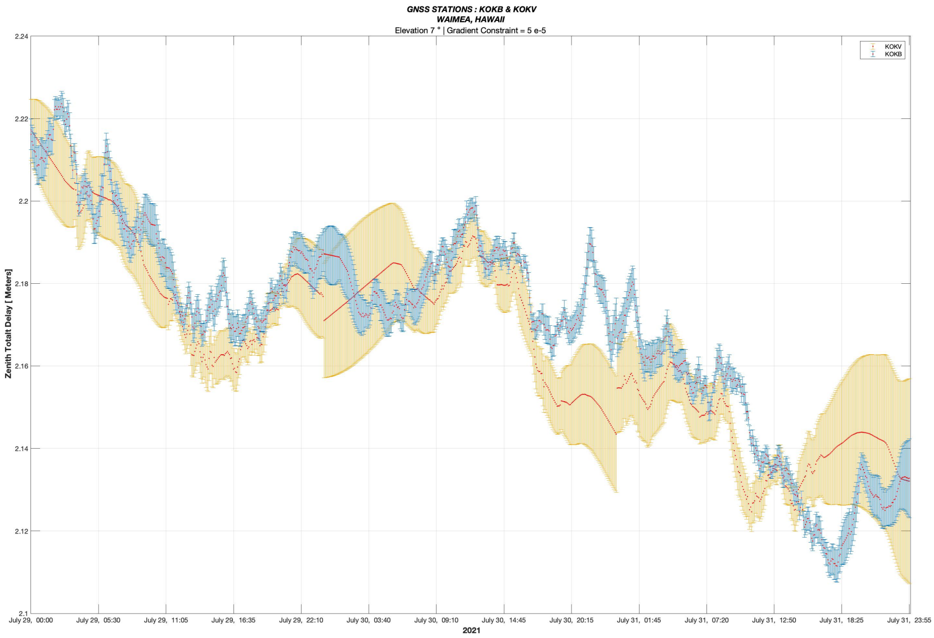

(a) The time series of the ZTD estimated for the Kokee Park stations processed with GRE. Elevation cut-off: 7°

(b) The time series of the ZTD estimated for the Kokee Park stations processed with GE. Elevation cut-off: 7°

Figure 4.34: The Time series of the ZTD estimated for the Kokee Park stations, including (4.34a) and excluding (4.34b) the Russian system

Luckily, the results have improved significantly for both stations in terms of consistency and uncertainty, e.g., millimeter level accuracy, as shown in figure 4.34b.

In addition, Two international stations were equally examined, MDO1 in Fort Davis, USA, and WTZR in Koetzting, Germany. Like the Goddard, Kokee Park, and Onsala stations, they were a part of an international campaign for July 2021. Thus their results were also assessed. The results for these stations are comparable. Where elevation 5° resulted in a slightly better uncertainty compared to 7°. Elevation 10° results, however, were the poorest.

The investigation showed that the number of included residuals for those stations, MDO1 and WTZR, is higher for elevation 7°, particularly with many deleted GPS measurements. This observation may justify the slight difference in uncertainties. More results can be found in section C.

4.6.2 Tropospheric Gradients

East and north gradients followed the same trend for all stations, with the best results reserved for elevation 7°. However, the results are anticipated considering the investigations and observations mentioned earlier.

Apart from the spike for GODS, 29th of July in the morning, the results for elevation 7° are more consistent with the remaining two, GODE and GODN. Those results are presented in figure 4.35.

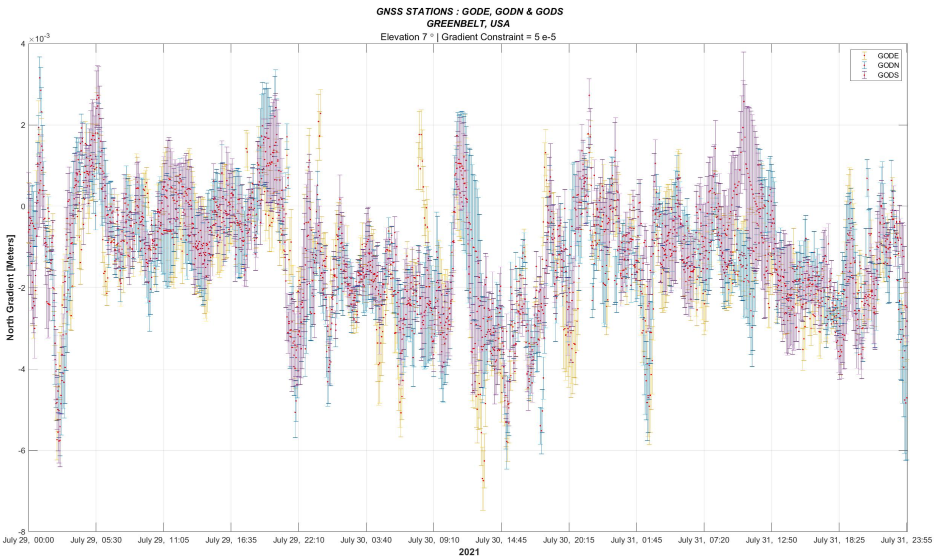

Figure 4.35: The time series of the North-South gradient estimated for the Goddard stations Elevation cut-off: 7°

The results for the Hawaii stations equally improved when removing GLONASS measurements. Figure 4.36 below compares the North gradient using GRE and GE constellations.

As opposed to ONSA and ONS1, the number of included measurements are generally below 80% for all international stations. Our interpretation suggests that the reason might be station or location-dependent. In addition, the number of deleted observations considerably improved when the Russian system was excluded. However, the impact of GLONASS on GPS measurements is interesting and requires further assessment.

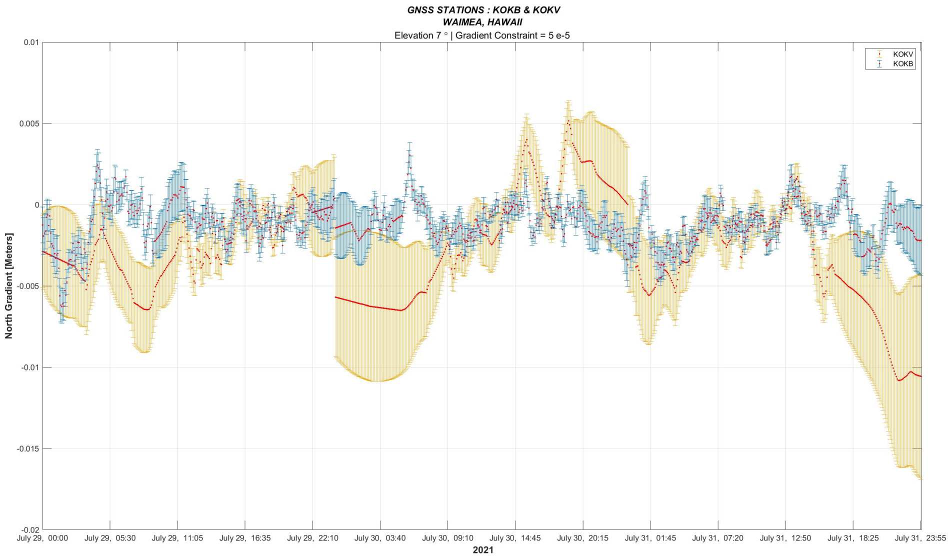

(a) The time series of the North-South gradient estimated for the Kokee Park stations processed with GRE. Elevation cut-off: 7°

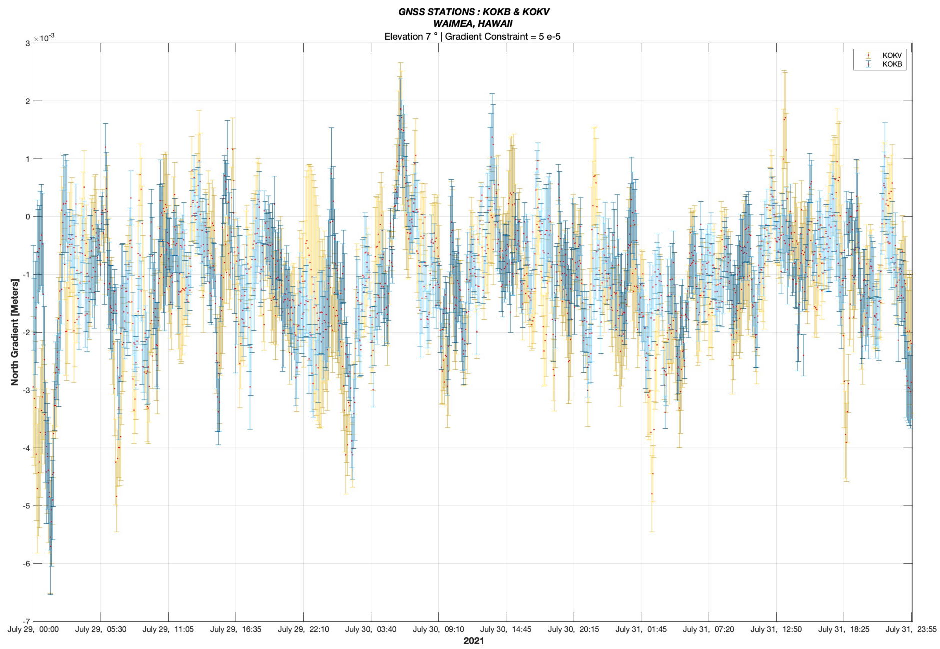

(b) The time series of the North-South gradient estimated for the Kokee Park stations processed with GE. Elevation cut-off: 7°

Figure 4.36: The time series for the North-South gradient for Kokee Park stations,including (4.36a) and excluding (4.36a) the Russian system

It is worth noting that the presented figures intend to highlight the differences between the tested cut-off angle. However, like in the ZTD case, more figures are available in appendix C.

The exact tools for comparison were unavailable to us during the assessment of the international stations. For instance, the unavailability of pressure data makes comparisons to WVR and VLBI impossible. However, the general conclusion is that using the elevation cut-off angle 7° and gradient constraint 5e-5 results in better agreement between the stations studied. In addition, the amount of the deleted GPS observations when including the GLONASS is considerable. Therefore, we acknowledge that more investigations are required.

4.7 Antenna Calibration Techniques Antenna-Specific vs Model-Specific

This section presents the results after implementing the antenna-specific phase-center correction matrices, instead of the default model-specific configuration, for ONS1 and the OTT stations. Since the obtained results for the OTT stations, including the Russian system, were poor, only periods after exchanging the receivers were included (February - March 2022).

The following subsections present a comparison between the antenna-specific and model-specific for the same station. For all these measurements, elevation cut-off angle 7° and gradient constraint 5e-5 have been used during processing.

4.7.1 Zenith Total Delay

Figure 4.37 compares antenna matrix corrections for ONS1 for April 2021. The results showed an identical behavior for both calibration techniques. No significant differences were identified.

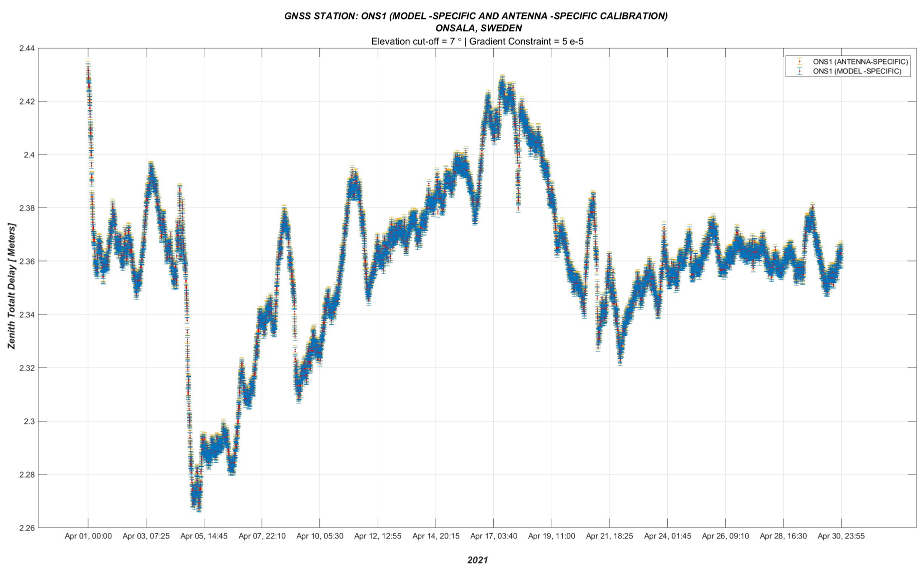

Figure 4.37: The time series for ZTD estimated for April 2021 for station ONS1, Model-specific (blue) and Antenna-specific (yellow)

On the other hand, apart from OTT1, all other OTT stations witnessed similar results for both calibration methods with identical estimation for the ZTD. OTT5 is the best in terms of uncertainty, as shown in figure 4.38.

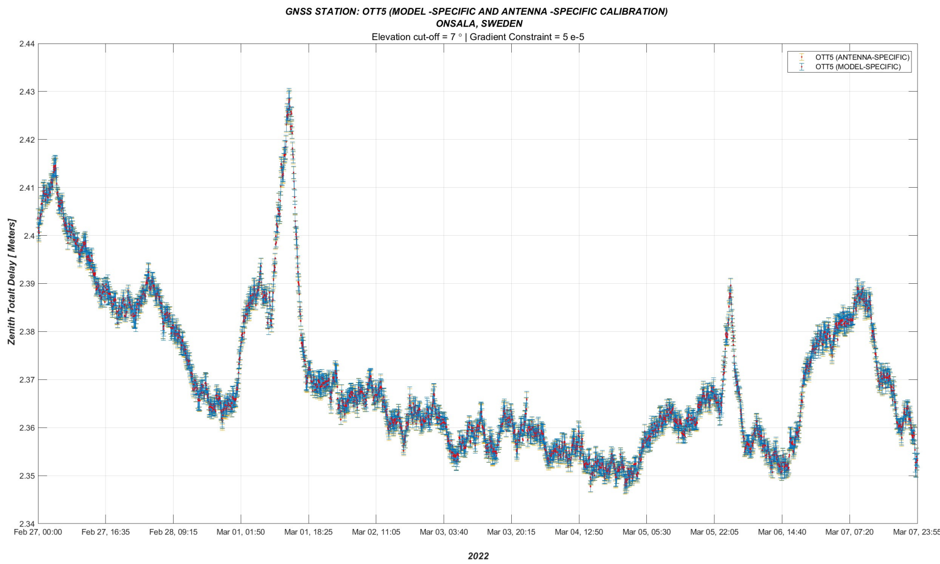

Figure 4.38: The time series for ZTD estimated for February - March 2022 for station OTT5, Model-specific (blue) and Antenna-specific (yellow)

The antenna-specific corrections for OTT1 (figure 4.39) forced the result to shift slightly. The reason for such bias is unknown, however, one explanation might be its location, considering the surrounding environment.

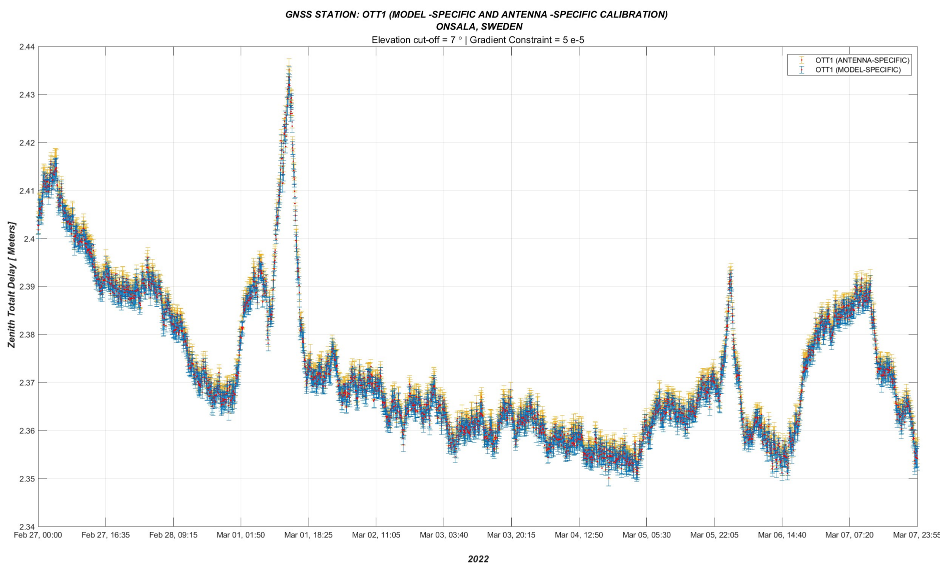

Figure 4.39: The time series for ZTD estimated for February - March 2022 for station OTT1, Model-specific (blue) and Antenna-specific (yellow)

A comparison with the VLBI or WVR data would have been of value. However, this was not feasible as the data was unavailable during the project. Nevertheless, we anticipate that, given the previous results, both calibration techniques have similar outcomes.

4.7.2 Tropospheric Gradients

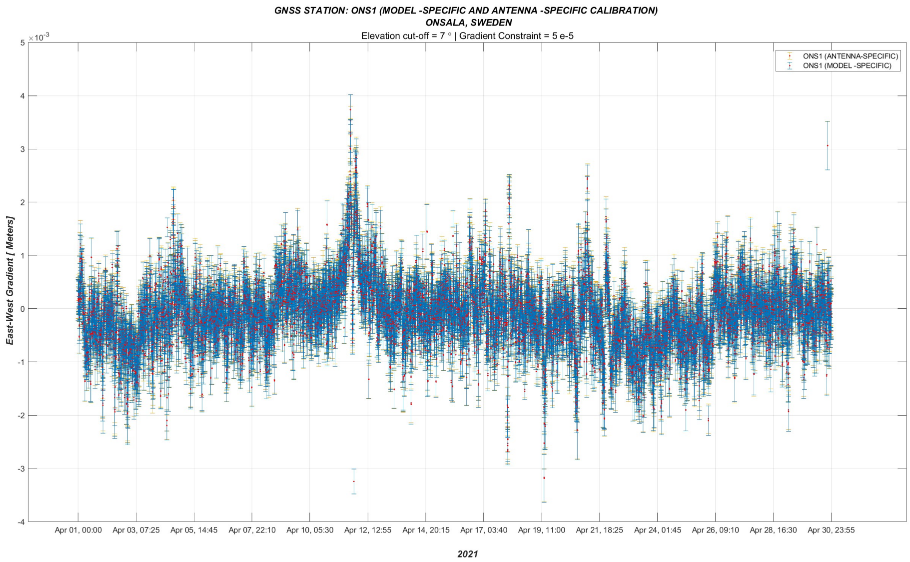

(a) The time series for North-South gradient estimated for April 2021 for station ONS1, Model-specific (blue) and Antenna-specific (yellow)

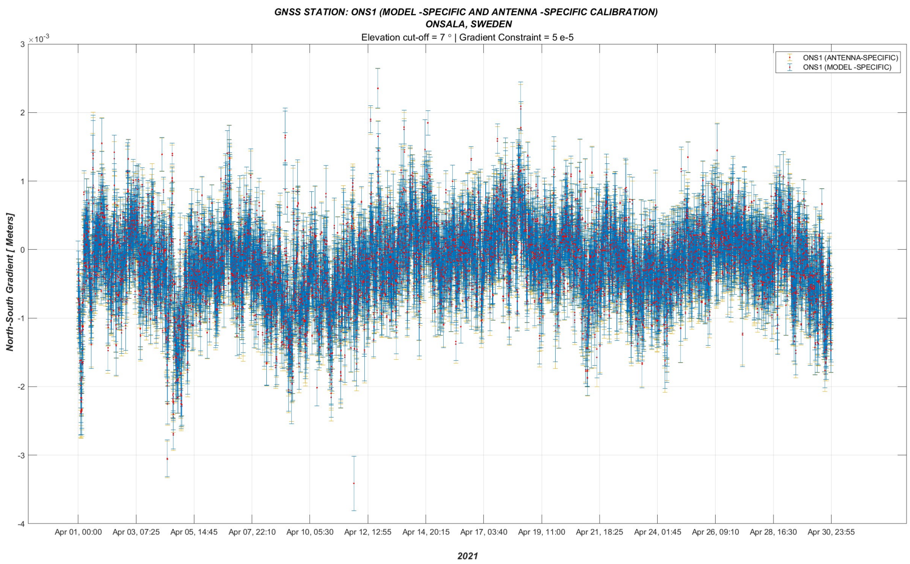

(b) The time series for East-West gradient estimated for April 2021 for station ONS1, Model-specific (blue) and Antenna-specific (yellow)

Figure 4.40: The time series for tropospheric gradients estimated on February - March 2022 for ONS1 station, North-South gradient (4.40a) & East-West gradient (4.40b)

North and east gradients are no exception to the previous results. All stations, including OTT1, reflected a total agreement between the compared results, with a millimeter level accuracy. Figure 4.40 and 4.41 represent the north and east gradients for the international station ONS1, and OTT5, respectively. The remaining results are included in section D.0.2.

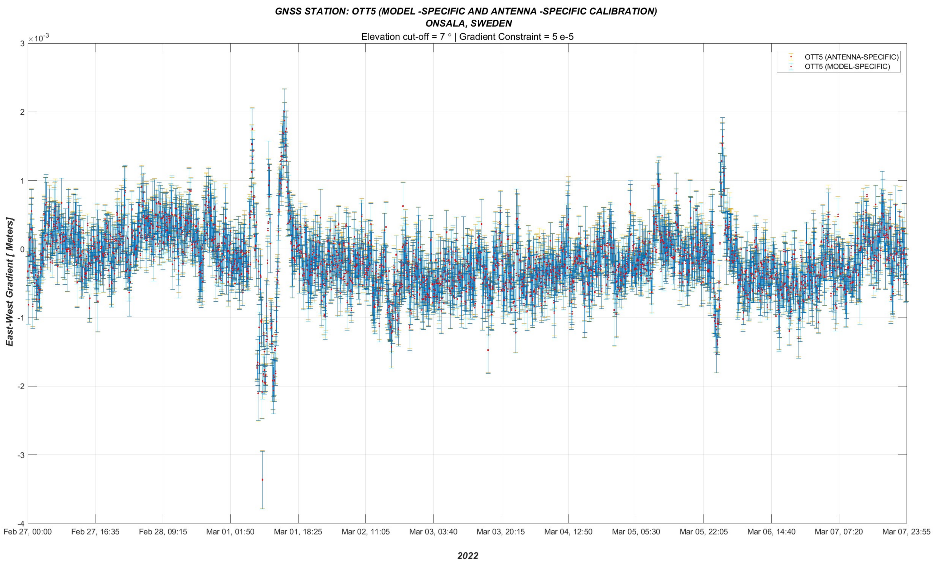

(a) The time series for North-South gradient estimated for February - March 2022 for station OTT5, Model-specific (blue) and Antenna-specific (yellow)

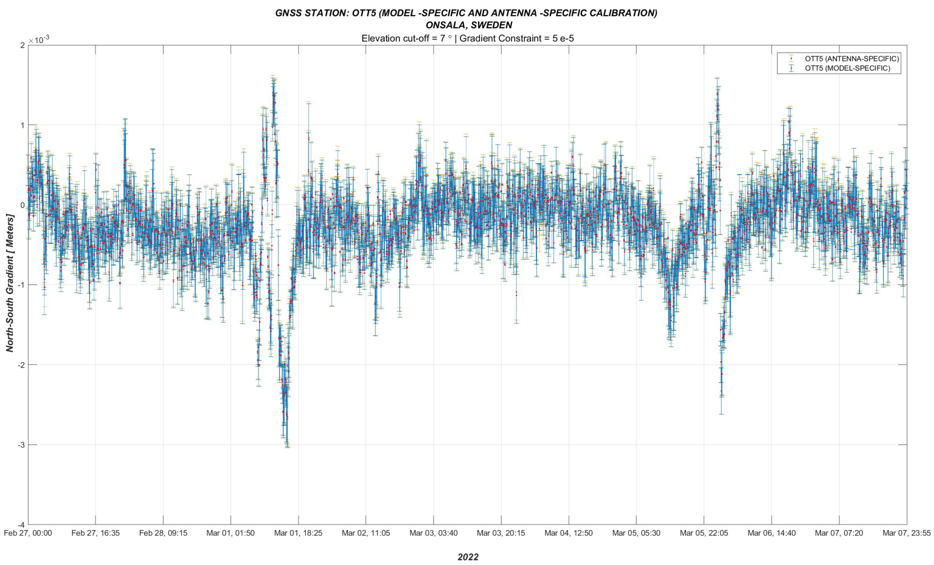

(b) The time series for East-West gradient estimated for February - March 2022 for station OTT5, Model-specific (blue) and Antenna-specific (yellow)

Figure 4.41: The time series for tropospheric gradients estimated on February - March 2022 for ONS1 station, North-South gradient (4.41a) & East-West gradient (4.41b)

An important point to mention is that the antenna for ONSA, the main station at the observatory, was not calibrated. However, an available station-calibration matrix was computed several years ago. Nevertheless, the matrix was developed to correct the phase-center for GPS measurements only. Thus, the intention was to develop an alternative that compensates for the three existing systems, GPS, GLONASS, and Galileo (see section 3.4 for more details).

5
Conclusion

GNSS contributes drastically to geodetic and geodynamic studies. However, despite the various error sources that hinder the quality of the results, the unpredictable variations of these systems raise another concern. Atmospheric prediction and climate monitoring are examples of GNSS high precision applications. Therefore, the report focused on examining different processing strategies to identify the best possible control factors that might eliminate some receivers-related errors.

The study's first phase, which concentrated on identifying the best gradient constraint and elevation cut-off angle, relied on comparisons with other measurement techniques, namely the WVR and VLBI. However, similar to the GNSS these techniques do not provide the absolute truth and possess multiple error sources. The WVR, for instance, is very sensitive to rain, thus its measurements are less reliable on rainy days. The study revealed that different constraints would differently impact measurement accuracy. Therefore, identifying an optimal control condition is exceptionally challenging, and it depends on a complicated correlation between those control parameters, especially for prediction and monitoring applications.

The selection of the optimal processing strategies followed a comprehensive approach considering multiple outcomes simultaneously and conducting detailed investigations. The analysis criteria included comparing the time series and their general trends, the mean and RMS values of the differences, and the uncertainties.

During the project, it was discovered that there are no ultimate choice of elevation cut-off angle or gradient constraint. Using the default constraint, 1e-5, resulted in lower mean and RMS values, however, the figures showed that this is likely only a result of the tight constraints, and therefore have a high uncertainty. Instead loosening the constraint generally seem to produce estimates that coincides more to those of WVR and VLBI. Similarly using the elevation cut-off angle 10° consistently results in larger error bars than for 7°. Therefore changing the original values of 10° and 1e-5 to 7° and 5e-5 appears to result in a small improvement of accuracy.

The processing of the international stations, generally showed that angle 7° is a valid choice in different environments across the globe. Saying that the calibrations used are the ultimate choice is of course impossible. However, the results seem to support the conclusion that it at least provides similar or better quality results to angle 10° and gradient constraint 1e-5.

An interesting finding during the project is the apparent effect of GLONASS data on the deletion of GPS data when using certain receivers. This issue was encountered both for the OTT stations at OSO and the KOK stations at Hawaii. The reason unfortunately remains unknown.

The study retains many limitations, one of which is that the attention was exclusively focused on a single environment and geographical area. Another limitation concerns the verification techniques, i.e., WVR and VLBI, as they do not provide the optimal solution or the limited available data. In addition, however, the two techniques provide data at different epochs leading to a slight misalignment between the different measurements, mainly when calculating the differences. Nevertheless, the results look promising. However, we anticipate the necessity of further investigations for different environments and results.

The second part of the study focused on antennas and their phase-center. Phase-center corrections are available as models in the software. They can also be provided in the control files for the individual antenna. The project examined the two previous methods and assessed the implications of utilizing different calibration matrices for the antenna phase-center. Changing the phase-center calibration matrices for ONS1 and the OTT stations showed no significant change in the results. A future subject of study could be to research the affect these matrices have when using different elevations cut-off angles and gradient constrains.

The last part of the project included the implementation and data acquisition for four temporary stations. The intention was to use these measurements to derive a station-specific calibration matrix that assesses the station's surrounding environment. Unfortunately, the station-specific calibration was not finalized. However, considering the importance of such investigation for the Swedish permanent network of GNSS stations, SWEPOS, and GNSS results, the study and investigation shall continue.

Bibliography

[1] D. Gebre-Egziabher and S. Gleason. Global navigation satellite systems: Present and future. In *GNSS Applications and Methods*, chapter 1 & 3, pages 1–20. Artech House, Norwood, MA, USA, 1 edition, 2009.

[2] L. Jacobson. *GNSS Markets and Applications*. GNSS Technology and Applications. Artech House, Norwood, MA, USA, 2007.

[3] B. Hofmann-Wellenhof, H. Lichtenegger, and E. Wasle. *GNSS–global navigation satellite systems: GPS, GLONASS, Galileo, and more*. Springer Science & Business Media, 2007.

[4] S. Jin, E. Cardellach, and F. Xie. *GNSS Remote Sensing: Theory, Methods and Applications*. Number 19 in Remote Sensing and Digital Image Processing. Springer Netherlands : Imprint: Springer, Dordrecht, 1st ed. 2014 edition, 2014.

[5] G. Blewitt. Basics of the GPS technique: observation equations. *Geodetic applications of GPS*, 10:54, 1997.

[6] D. Roddy. *Satellite communications*. McGraw-Hill Education, 2006.

[7] J.M. Juan Zornoza J. Sanz Subirana and M. Hernández-Pajares. ESA Navipedia, 2011.

[8] P. Blunt. Gnss signal acquisition and tracking. In *GNSS Applications and Methods*, chapter 2. Artech House, 2009.

[9] T. Hobiger and N. Jakowski. Atmospheric signal propagation. In Oliver Montenbruck and Peter J.G. Teunissen, editors, *Springer Handbook of Global Navigation Satellite Systems*, chapter 6. Springer International Publishing, 2017.

[10] B. Rama Rao, W. Kunysz, R. Fante, and K. McDonald. *GPS/GNSS Antennas*. Artech House, 2013.

[11] P.S. Kildal. *Foundations of Antenna Engineering: A unitfied approach for Line-of-Sight and Multi-path*. Kildal Antenn AB, Gothenburg, Sweden, 2015.

[12] D. Bétaille. Assessment and improvement of the capabilities of a window correlator to model gps multi-path phase errors. 2004.

[13] International GNSS Service. Data and products, 2020.

[14] C. Rizos and D.A. Grejner-Brzezinska. Geodesy and surveying. In *GNSS Applications and Methods*, chapter 14. Artech House, 2017.

[15] S.M. Lichten, Y. Bar-Sever, W. Bertiger, M. Heflin, K. Hurst, R.J. Muellerschoen, S.C. Wu, T.P. Yunck, and J. Zumberge. Gipsy-oasis11: A high precision gps data processing system and general satellite orbit analysis tool.

[16] D. Gebre-Egziabher, M. Petovello, and D. Bevly. Integration of gnss and ins: Part. In *GNSS Applications and Methods*, chapter 6. Artech House, 2017.

[17] S.L.Miller and D. Childers. *Probability and Random Processes With Applications to Signal Processing and Communications*. Elsevier In, 2012.

[18] J. Sanz Subirana, J.M. Juan Zornoza, and M. Hernández-Pajares. *PGNSS DATA PROCESSING :Volume I: Fundamentals and Algorithms*. ESA Communications, 2013.

[19] C.O. Ao. Atmospheric sensing using gnss occultations. In *GNSS Applications and Methods*, chapter 15. Artech House, 2017.

A

Processing Strategies: Gradient Constraints & Elevation Angles

This section contains additional results for July 29th to 31st. Comparing different processing configurations.

A.1 Baseline Assessment: 1e-5 and 10°

A.1.1 Zenith Delays

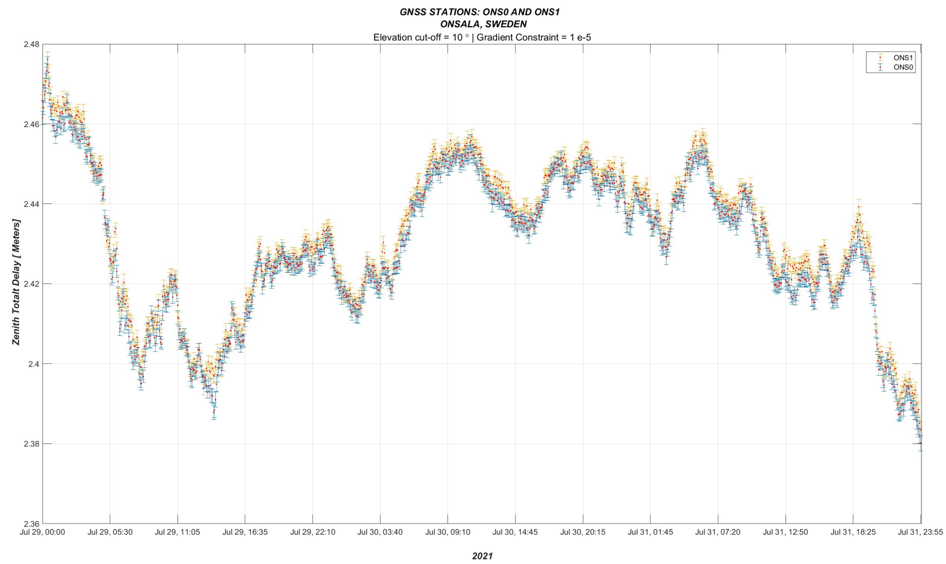

Figure A.1: The time series of the ZTD eatimated for stations ONS0 and ONS1. Gradient constraint: 1e-5, Elevation cut-off: 10°

A.1.2 Tropospheric Gradients

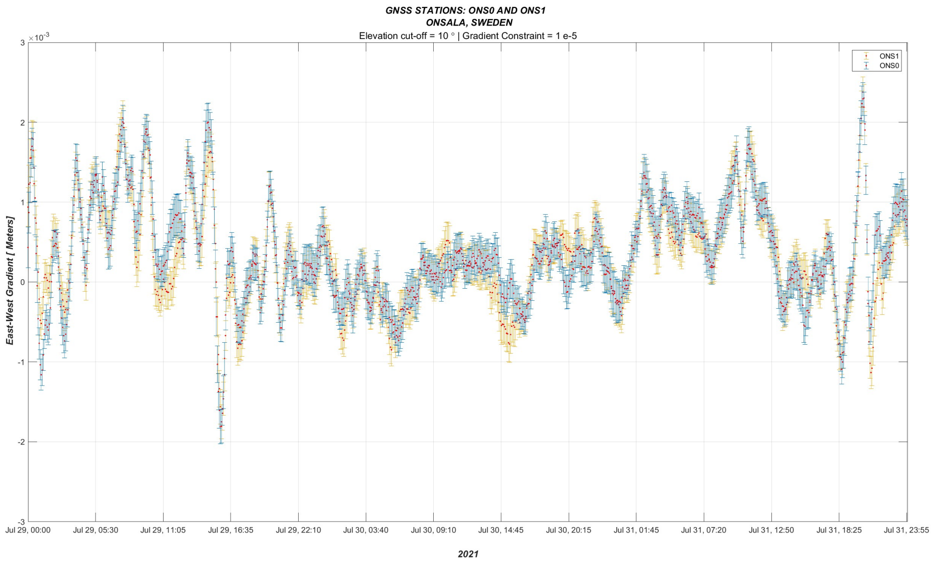

(a) East-West gradient estimated for stations ONS0 and ONS1. Gradient constraint: 1e-5, Elevation cut-off: 10°

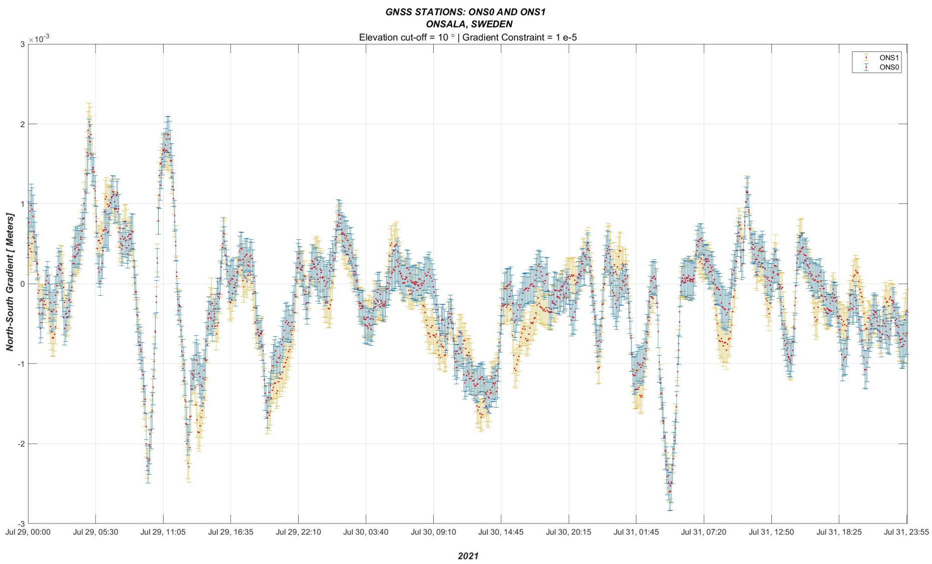

(b) North-South gradient estimated for stations ONS0 and ONS1. Gradient constraint: 1e-5, Elevation cut-off: 10°

Figure A.2: Gradients time series of the East-West gradient (A.2a) and North-South gradient (A.2b) estimated for stations ONS0 and ONS1. Gradient constraint: 1e-5, Elevation cut-off: 10°

A.2 Implications of Loosening the Gradient Constraint: 5e-5 and 10°

A.2.1 Zenith Delay

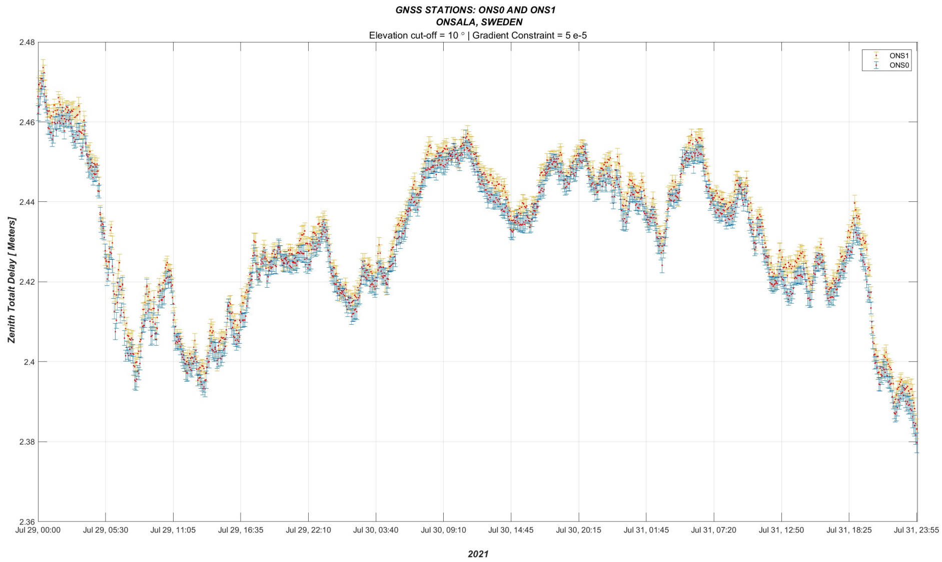

Figure A.3: The time series of the ZTD eatimated for stations ONS0 and ONS1. Gradient constraint: 5e-5, Elevation cut-off: 10°

A.2.2 Tropospheric Gradients

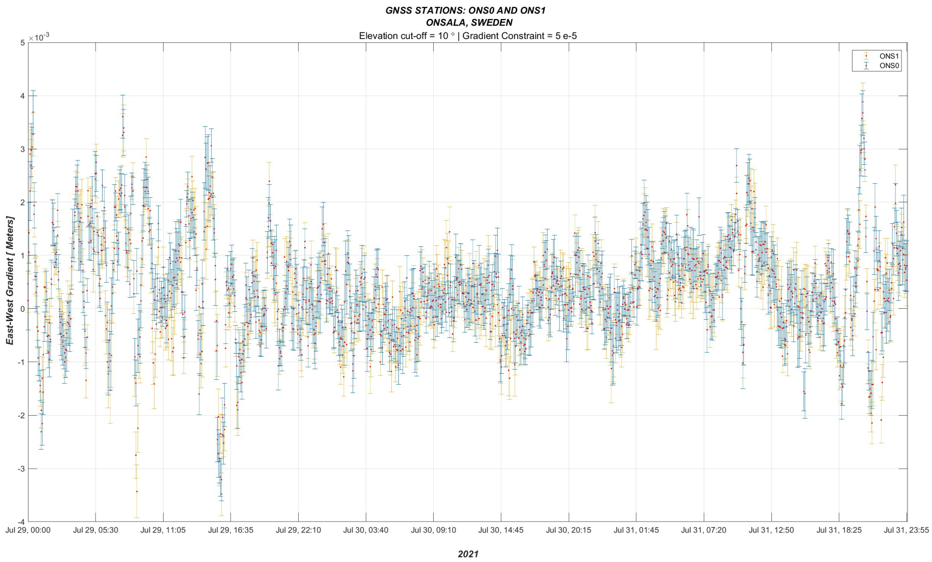

(a) East-West gradient estimated for stations ONS0 and ONS1. Gradient constraint: 5e-5, Elevation cut-off: 10°

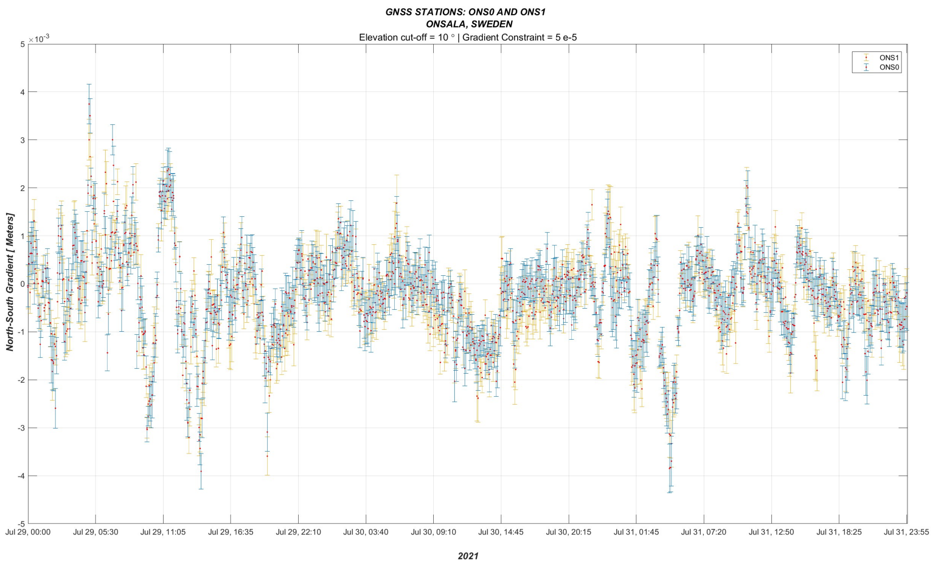

(b) North-South gradient estimated for stations ONS0 and ONS1. Gradient constraint: 5e-5, Elevation cut-off: 10°

Figure A.4: Gradients time series of the East-West gradient (A.4a) and North-South gradient (A.4b) estimated for stations ONS0 and ONS1. Gradient constraint: 5e-5, Elevation cut-off: 10°

A.3 Elevation Cut-off Assessment: 1e-5 and 7°

A.3.1 Zenith Delay

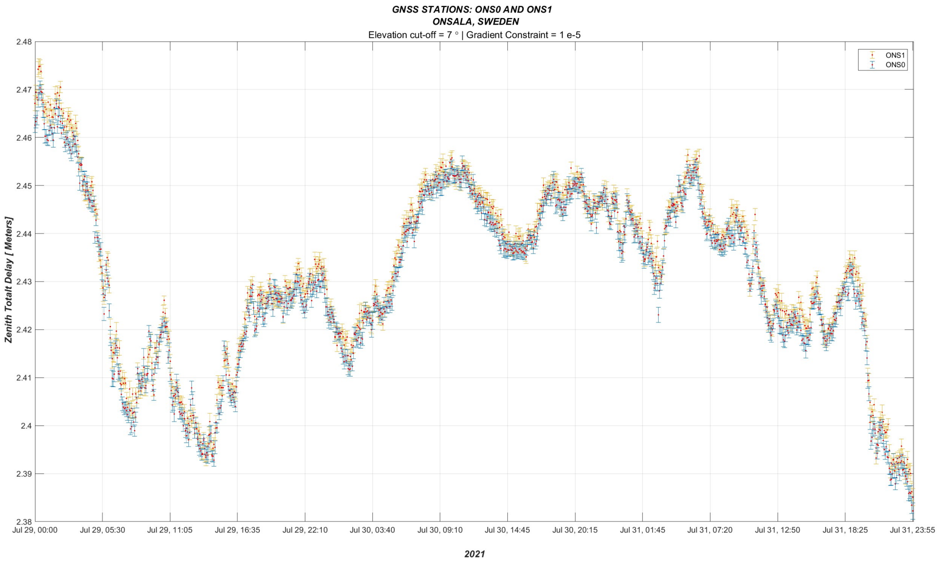

Figure A.5: The time series of the ZTD eatimated for stations ONS0 and ONS1. Gradient constraint: 1e-5, Elevation cut-off: 7°

A.3.2 Tropospheric Gradients

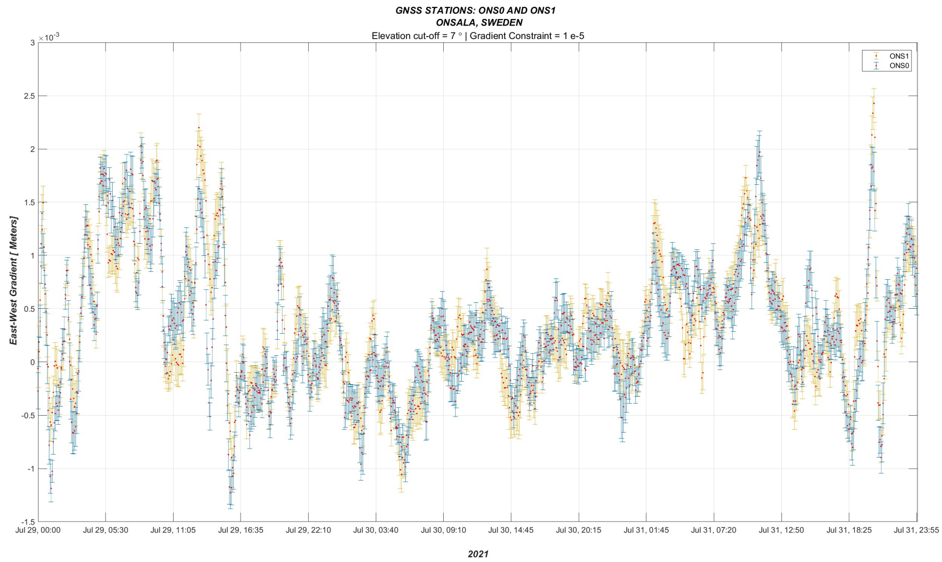

(a) East-West gradient estimated for stations ONS0 and ONS1. Gradient constraint: 1e-5, Elevation cut-off: 7°

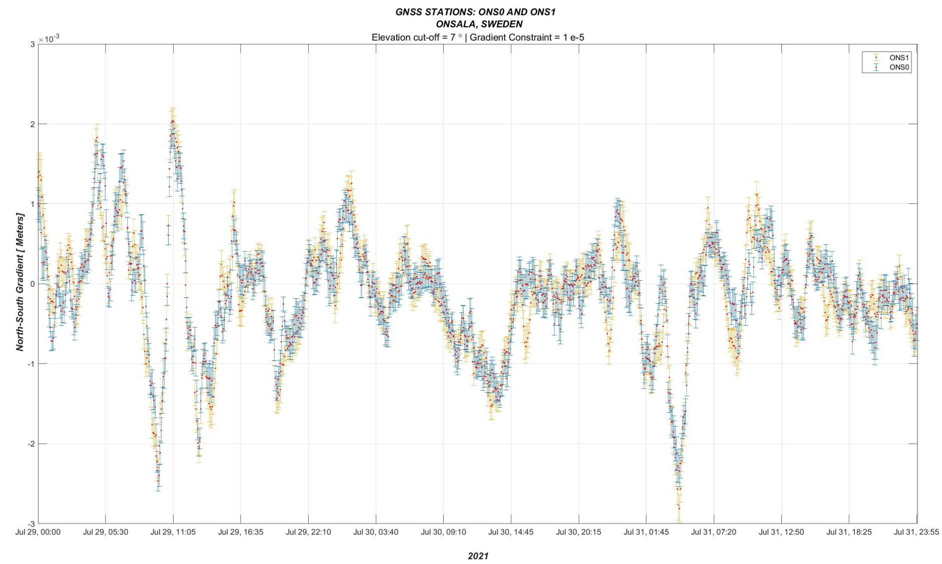

(b) North-South gradient estimated for stations ONS0 and ONS1. Gradient constraint: 1e-5, Elevation cut-off: 7°

Figure A.6: Gradients time series of the East-West gradient (A.6a) and North-South gradient (A.6a) estimated for stations ONS0 and ONS1. Gradient constraint: 1e-5, Elevation cut-off: 7°

A.4 The Optimal Configuration: 5e-5 and Elevation and 7°

A.4.1 Zenith Delay

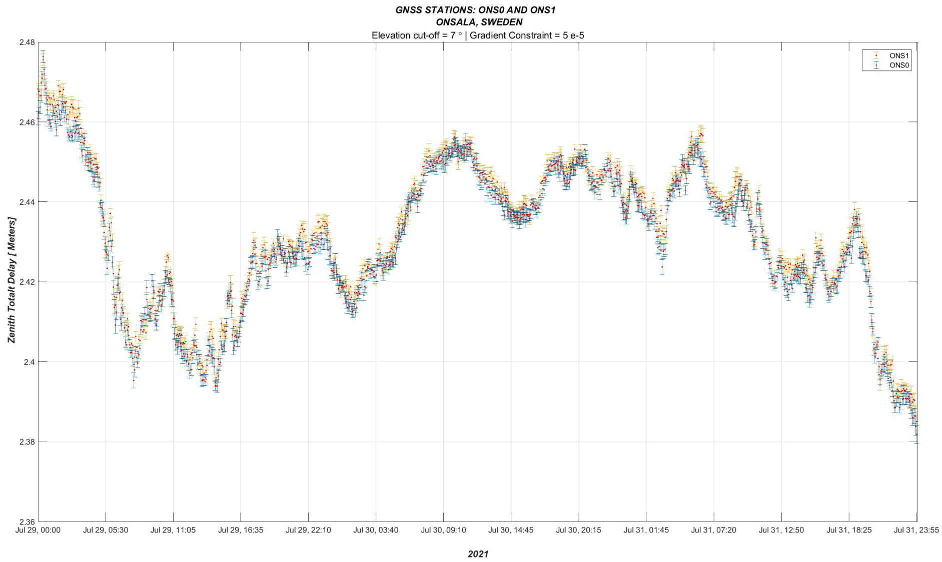

Figure A.7: The time series of the ZTD eatimated for stations ONS0 and ONS1. Gradient constraint: 5e-5, Elevation cut-off: 7°

A.4.2 Tropospheric Gradients

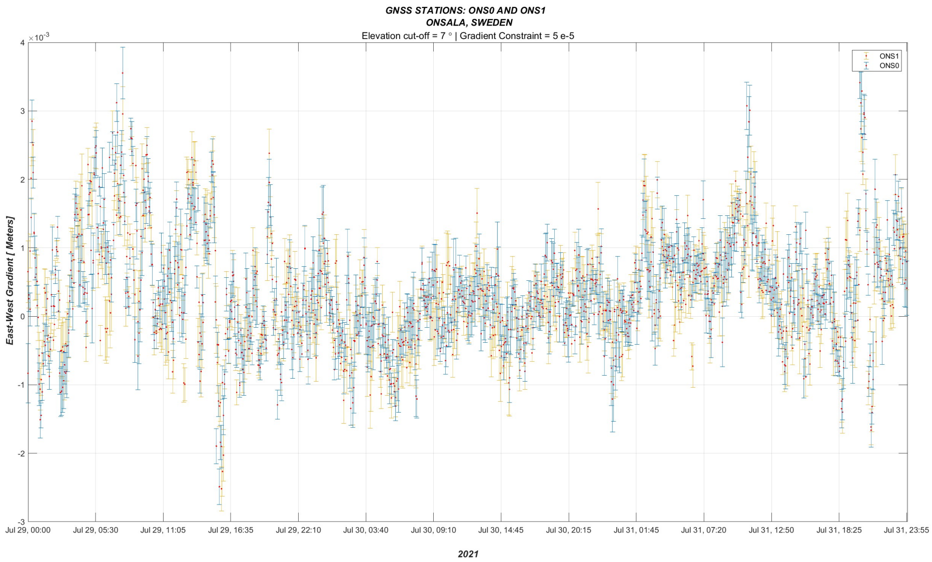

(a) East-West gradient estimated for stations ONS0 and ONS1. Gradient constraint: 5e-5, Elevation cut-off: 7°

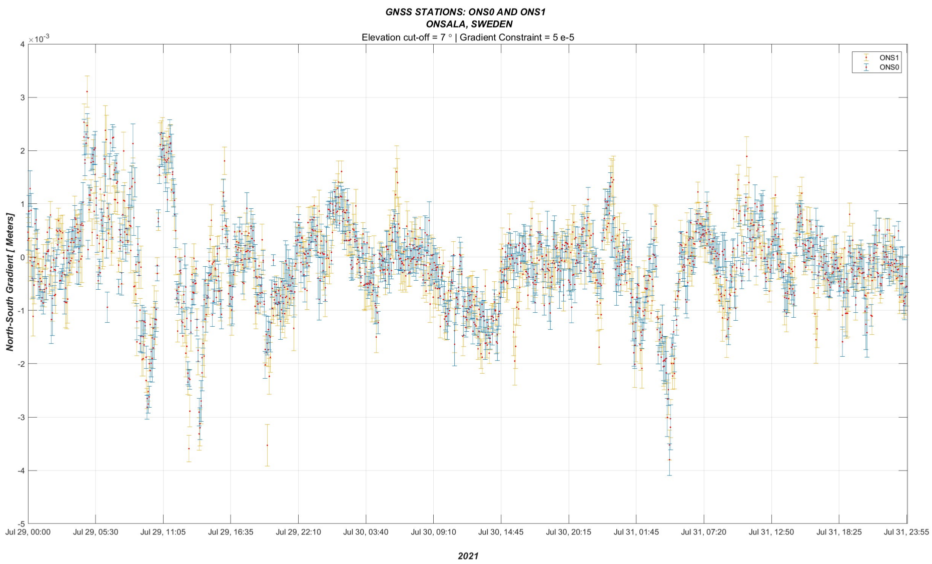

(b) North-South gradient estimated for stations ONS0 and ONS1. Gradient constraint: 5e-5, Elevation cut-off: 7°

Figure A.8: Gradients time series of the East-West gradient (A.8a) and North-South gradient (A.8a) estimated for stations ONS0 and ONS1. Gradient constraint: 5e-5, Elevation cut-off: 7°

A.4.3 The Mean and RMS of the Differences for ONS0, ONS1, VLBI, and WVR

Table A.1: The mean and RMS of the ZWD differences estimated for ONS0, ONS1 and WVR (22 to 27 April 2021)

Elevation angle	Grad const [km/s^2]	ONS0		ONS1	
		WVR mean [m]	WVR RMS [m]	WVR mean [m]	WVR RMS [m]
10 °	1e-5	-1.053e-03	2.442e-03	2.104e-03	3.181e-03
	5e-5	-1.108e-03	2.444e-03	2.275e-03	3.308e-03
	1e-4	-1.107e-03	2.454e-03	2.283e-03	3.317e-03
	5e-4	-1.109e-03	2.464e-03	2.272e-03	3.308e-03
7 °	1e-5	-5.823e-04	2.282e-03	1.450e-03	2.753e-03
	5e-5	-5.968e-04	2.266e-03	1.632e-03	2.889e-03
	1e-4	-5.692e-04	2.367e-03	1.614e-03	2.887e-03
	5e-4	-6.010e-04	2.293e-03	1.599e-03	2.900e-03

Table A.2: The mean and RMS of the ZWD differences estimated for ONS0 A.2a, ONS1 A.2b, VLBI (OTTE) (29-30 July 2021) and WVR (29-31 July 2021)

Elevation angle	Grad const [km/s^2]	WVR mean [m]	WVR RMS [m]	VLBI mean [m]	VLBI RMS [m]
10 °	1e-6	-8.058e-03	1.069e-02	3.667e-03	5.048e-03
	5e-6	-7.807e-03	1.050e-02	3.755e-03	4.954e-03
	1e-4	-8.712e-03	9.965e-03	3.820e-03	5.012e-03
	5e-4	-7.781e-03	1.047e-02	3.818e-03	5.018e-03
7 °	1e-4	-7.692e-03	9.280e-03	4.702e-03	5.678e-03
	5e-4	-7.651e-03	9.293e-03	4.722e-03	5.701e-03
5 °	1e-5	-7.169e-03	9.006e-03	4.893e-03	5.886e-03
	5e-5	-7.181e-03	8.979e-03	4.974e-03	5.959e-03
	1e-4	-7.171e-03	8.971e-03	4.994e-03	5.984e-03
	5e-4	-7.157e-03	8.996e-03	4.969e-03	5.955e-03
3 °	1e-5	-6.767e-03	8.836e-03	5.242e-03	6.282e-03
	5e-5	-6.966e-03	8.894e-03	5.109e-03	6.131e-03
	1e-4	-6.993e-03	8.911e-03	5.089e-03	6.123e-03
	5e-4	-6.974e-03	8.922e-03	5.094e-03	6.129e-03

(a) Mean and RMS of the ZWD differences for ONS0, OTTE, and WVR

Elevation angle	Grad const [km/s^2]	WVR mean [m]	WVR RMS [m]	VLBI mean [m]	VLBI RMS [m]
10 °	1e-6	-5.653e-03	9.124e-03	5.978e-03	7.148e-03
	5e-6	-5.547e-03	8.908e-03	6.030e-03	7.121e-03
	1e-4	-5.855e-03	7.630e-03	6.281e-03	7.307e-03
	5e-4	-5.208e-03	8.835e-03	6.253e-03	7.297e-03
7 °	1e-4	-5.596e-03	7.603e-03	6.498e-03	7.388e-03
	5e-4	-5.605e-03	7.602e-03	6.460e-03	7.355e-03
5 °	1e-5	-5.954e-03	8.035e-03	6.377e-03	7.278e-03
	5e-5	-5.856e-03	7.892e-03	6.262e-03	7.166e-03
	1e-4	-5.797e-03	7.847e-03	6.401e-03	7.307e-03
	5e-4	-5.831e-03	7.883e-03	6.219e-03	7.123e-03
3 °	1e-5	-5.683e-03	7.920e-03	6.776e-03	7.707e-03
	5e-5	-5.756e-03	7.865e-03	6.821e-03	7.774e-03
	1e-4	-5.739e-03	7.880e-03	6.862e-03	7.839e-03
	5e-4	-5.718e-03	7.844e-03	6.803e-03	7.731e-03

(b) Mean and RMS of the ZWD differences for ONS1, OTTE, and WVR

Table A.3: The mean and RMS of the North-South gradients differences estimated for ONS0, ONS1 and WVR (22 to 27 April 2021)

Elevation angle	Grad const [km/s^2]	ONS0		ONS1	
		WVR mean [m]	WVR RMS [m]	WVR mean [m]	WVR RMS [m]
10 °	1e-5	-2.641e-04	4.586e-04	-2.260e-04	4.226e-04
	5e-5	-2.833e-04	5.385e-04	-2.475e-04	5.441e-04
	1e-4	-2.875e-04	5.745e-04	-2.503e-04	5.994e-04
	1e-5	-2.401e-04	3.972e-04	-1.921e-04	3.753e-04
7 °	1e-5	-2.401e-04	3.972e-04	-1.921e-04	3.753e-04
	5e-5	-2.577e-04	4.688e-04	-2.038e-04	4.642e-04
	1e-4	-2.744e-04	6.846e-04	-2.077e-04	5.044e-04
	5e-4	-2.742e-04	7.366e-04	-1.336e-04	2.722e-03

Table A.4: The mean and RMS of the North-South gradient differences estimated for ONS0 A.4a, ONS1 A.4b, VLBI (OTTE) (29-30 July 2021) and WVR (29-31 July 2021)

Elevation angle	Grad const [km/s^2]	WVR mean [m]	WVR RMS [m]	VLBI mean [m]	VLBI RMS [m]
10 °	1e-6	-4.985e-04	1.253e-03	7.151e-05	4.696e-04
	5e-6	-5.315e-04	1.138e-03	2.490e-05	3.581e-04
	1e-4	-5.810e-04	1.106e-03	-7.984e-06	5.892e-04
	5e-4	-5.944e-04	1.203e-03	-1.126e-05	6.260e-04
7 °	1e-4	-4.778e-04	1.105e-03	5.303e-05	5.437e-04
	5e-4	-4.875e-04	1.121e-03	5.134e-05	5.591e-04
5 °	1e-5	-3.804e-04	1.049e-03	1.597e-04	4.395e-04
	5e-5	-4.013e-04	1.088e-03	1.222e-04	5.038e-04
	1e-4	-3.967e-04	1.098e-03	1.227e-04	5.174e-04
	5e-4	-4.059e-04	1.112e-03	1.222e-04	5.271e-04
3 °	1e-5	-3.771e-04	1.071e-03	1.775e-04	4.523e-04
	5e-5	-3.745e-04	1.087e-03	1.512e-04	4.952e-04
	1e-4	-3.772e-04	1.091e-03	1.483e-04	5.042e-04
	5e-4	-3.753e-04	1.104e-03	1.476e-04	5.092e-04

(a) Mean and RMS of the North-South gradients differences for ONS0, OTTE, and WVR

Elevation angle	Grad const [km/s^2]	WVR mean [m]	WVR RMS [m]	VLBI mean [m]	VLBI RMS [m]
10 °	1e-6	-6.027e-04	1.310e-03	-8.210e-05	4.872e-04
	5e-6	-6.313e-04	1.200e-03	-1.250e-04	4.135e-04
	1e-4	-6.247e-04	1.142e-03	-1.538e-04	7.005e-04
	5e-4	-6.782e-04	1.269e-03	-1.609e-04	7.576e-04
7 °	1e-4	-7.692e-03	9.280e-03	1.259e-05	6.408e-04
	5e-4	-7.651e-03	9.293e-03	6.329e-07	6.736e-04
5 °	1e-5	-4.105e-04	1.032e-03	1.687e-04	4.193e-04
	5e-5	-4.578e-04	1.058e-03	7.871e-05	5.345e-04
	1e-4	-4.577e-04	1.082e-03	4.066e-05	6.377e-04
	5e-4	-4.679e-04	1.096e-03	3.523e-05	6.951e-04
3 °	1e-5	-3.865e-04	1.061e-03	2.044e-04	4.492e-04
	5e-5	-4.231e-04	1.085e-03	1.579e-04	5.569e-04
	1e-4	-4.155e-04	1.094e-03	1.206e-04	6.441e-04
	5e-4	-4.164e-04	1.091e-03	1.172e-04	6.277e-04

(b) Mean and RMS of the North-South gradients differences for ONS1, OTTE, and WVR

Table A.5: The mean and RMS of the East-West gradients differences estimated for ONS0, ONS1 and WVR (22 to 27 April 2021)

Elevation angle	Grad const [km/s^2]	ONS0		ONS1	
		WVR mean [m]	WVR RMS [m]	WVR mean [m]	WVR RMS [m]
10 °	1e-5	-5.984e-04	7.342e-04	-5.603e-04	7.105e-04
	5e-5	-5.877e-04	7.822e-04	-5.681e-04	7.912e-04
	1e-4	-5.800e-04	8.085e-04	-5.707e-04	8.407e-04
	5e-4	-5.777e-04	8.293e-04	-5.728e-04	8.802e-04
7 °	1e-5	-5.284e-04	6.908e-04	-5.496e-04	7.102e-04
	5e-5	-5.515e-04	7.624e-04	-5.541e-04	7.716e-04
	1e-4	-5.739e-04	9.053e-04	-5.561e-04	7.993e-04
	5e-4	-5.713e-04	9.084e-04	-5.744e-04	9.800e-04

Table A.6: The mean and RMS of the East-West gradient differences estimated for ONS0, ONS1, VLBI (OTTE)(29-30 July 2021) and WVR (29-31 July 2021)

Elevation angle	Grad const [km/s^2]	WVR mean [m]	WVR RMS [m]	VLBI mean [m]	VLBI RMS [m]
10 °	1e-6	-5.325e-04	1.353e-03	2.066e-04	4.926e-04
	5e-6	-5.405e-04	1.281e-03	1.982e-04	4.896e-04
	1e-4	-5.284e-04	1.252e-03	2.734e-04	7.418e-04
	5e-4	-5.345e-04	1.324e-03	2.734e-04	7.783e-04
7 °	1e-4	-5.903e-04	1.253e-03	1.896e-04	6.904e-04
	5e-4	-5.807e-04	1.291e-03	1.858e-04	7.052e-04
5 °	1e-5	-5.920e-04	1.264e-03	1.663e-04	5.701e-04
	5e-5	-5.901e-04	1.260e-03	1.550e-04	6.286e-04
	1e-4	-5.893e-04	1.272e-03	1.496e-04	6.544e-04
	5e-4	-5.743e-04	1.317e-03	1.522e-04	6.692e-04
3 °	1e-5	-6.168e-04	1.279e-03	1.304e-04	5.253e-04
	5e-5	-5.853e-04	1.273e-03	1.324e-04	5.902e-04
	1e-4	-5.762e-04	1.279e-03	1.349e-04	6.113e-04
	5e-4	-5.583e-04	1.323e-03	1.360e-04	6.219e-04

(a) Mean and RMS of the East-West gradients differences for ONS0, OTTE, and WVR

Elevation angle	Grad const [km/s^2]	WVR mean [m]	WVR rms [m]	VLBI mean [m]	VLBI rms [m]
10 °	1e-6	-5.515e-04	1.353e-03	1.699e-04	4.901e-04
	5e-6	-5.617e-04	1.287e-03	1.578e-04	4.649e-04
	1e-4	-5.852e-04	1.241e-03	2.425e-04	7.261e-04
	5e-4	-5.550e-04	1.280e-03	2.481e-04	7.840e-04
7 °	1e-4	-6.038e-04	1.270e-03	1.790e-04	6.895e-04
	5e-4	-6.054e-04	1.286e-03	1.820e-04	7.168e-04
5 °	1e-5	-6.129e-04	1.284e-03	1.559e-04	5.718e-04
	5e-5	-6.049e-04	1.258e-03	1.737e-04	6.441e-04
	1e-4	-5.985e-04	1.265e-03	2.849e-04	1.559e-03
	5e-4	-5.926e-04	1.268e-03	2.951e-04	1.646e-03
3 °	1e-5	-6.323e-04	1.293e-03	1.558e-04	5.415e-04
	5e-5	-6.328e-04	1.298e-03	2.024e-04	8.955e-04
	1e-4	-6.115e-04	1.288e-03	2.994e-04	1.667e-03
	5e-4	-6.258e-04	1.313e-03	2.946e-04	1.729e-03

(b) Mean and RMS of the East-West gradients differences for ONS1, OTTE, and WVR

B

Processing Strategies : Three Years Comparison

This section contains additional results for April 2019 to December 2021. Comparing the default configurations (1e-5 and 10°) with the optimal selection (5e-5 and 7°).

B.0.1 Zenith Delay

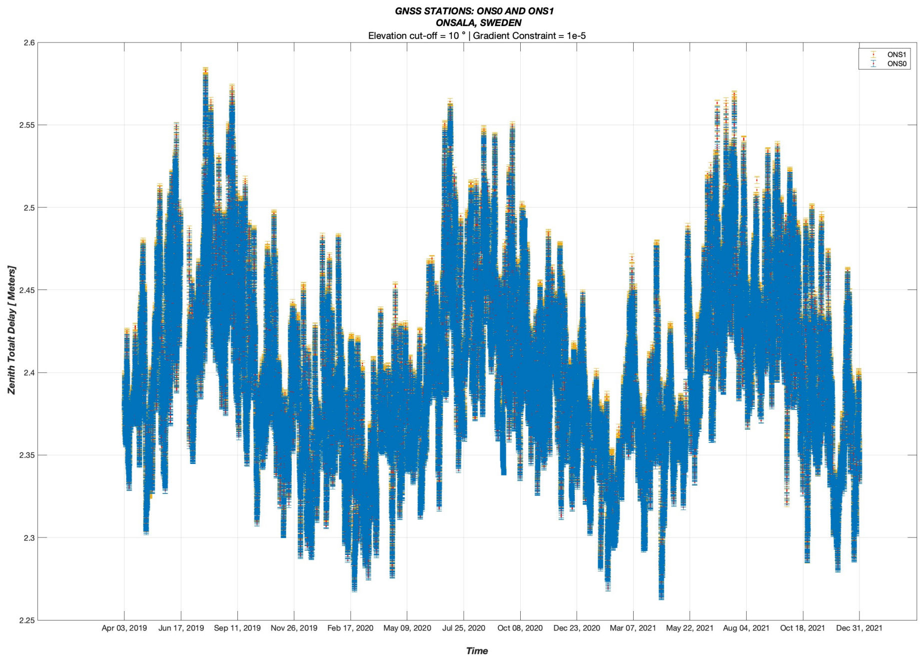

Figure B.1: The time series of the ZTD eatimated for stations ONS0 and ONS1. Gradient constraint: 1e-5, Elevation cut-off: 10°

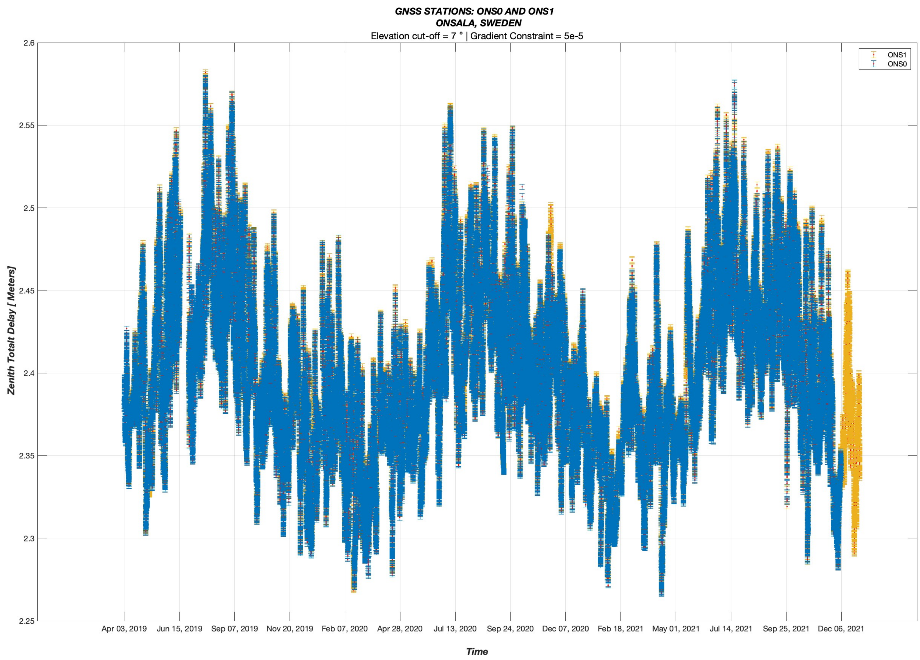

Figure B.2: The time series of the ZTD eatimated for stations ONS0 and ONS1. Gradient constraint: 5e-5, Elevation cut-off: 7°

B.0.2 Tropospheric Gradients

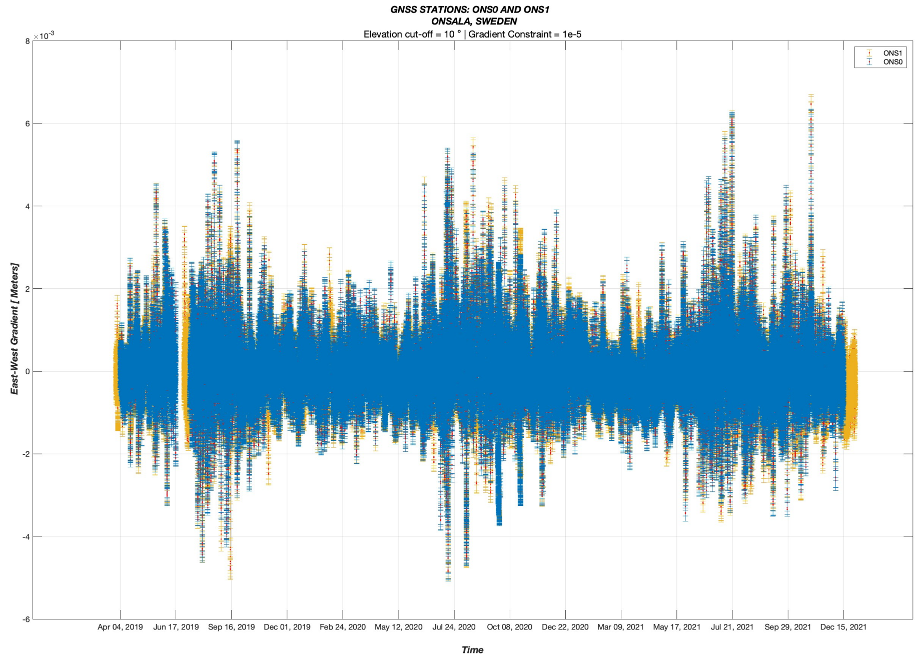

(a) East-West gradient estimated for stations ONS0 and ONS1

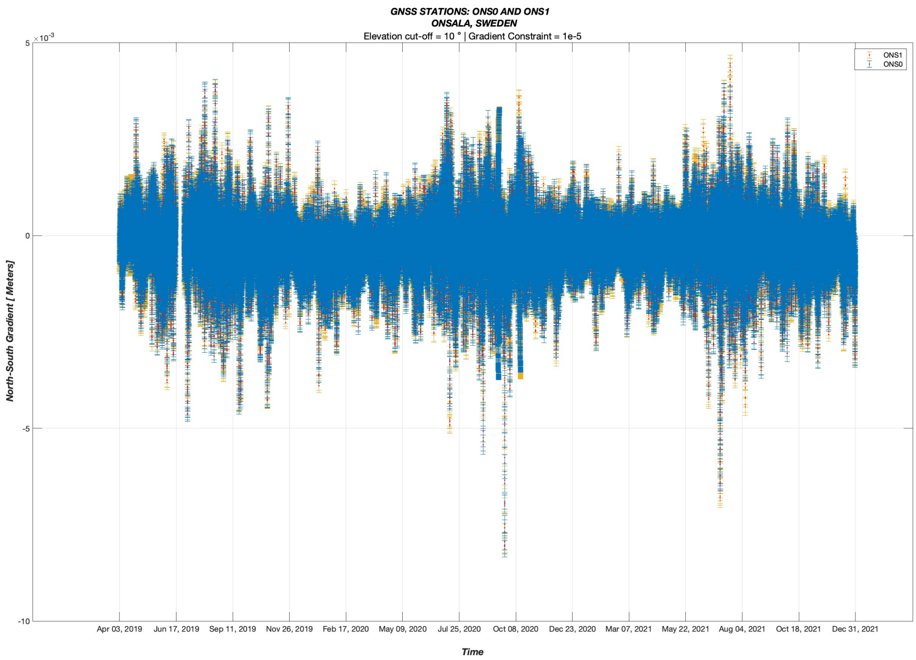

(b) North-South gradient estimated for stations ONS0 and ONS1

Figure B.3: Gradients time series of the East-West gradient (B.3a) and North-South gradient (B.3b) estimated for stations ONS0 and ONS1. Gradient constraint: 1e-5, Elevation cut-off: 10°

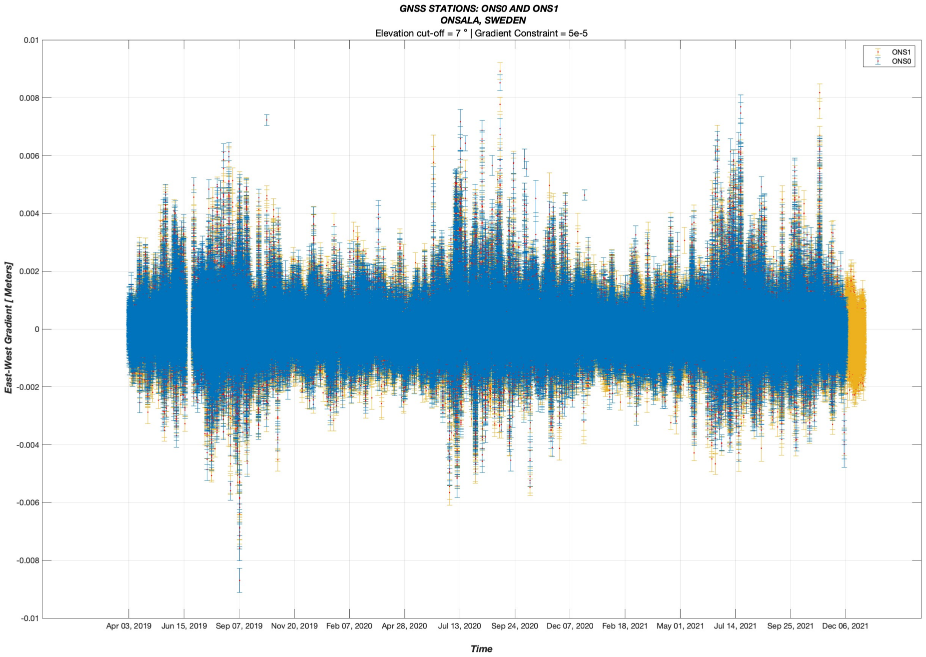

(a) East-West gradient estimated for stations ONS0 and ONS1

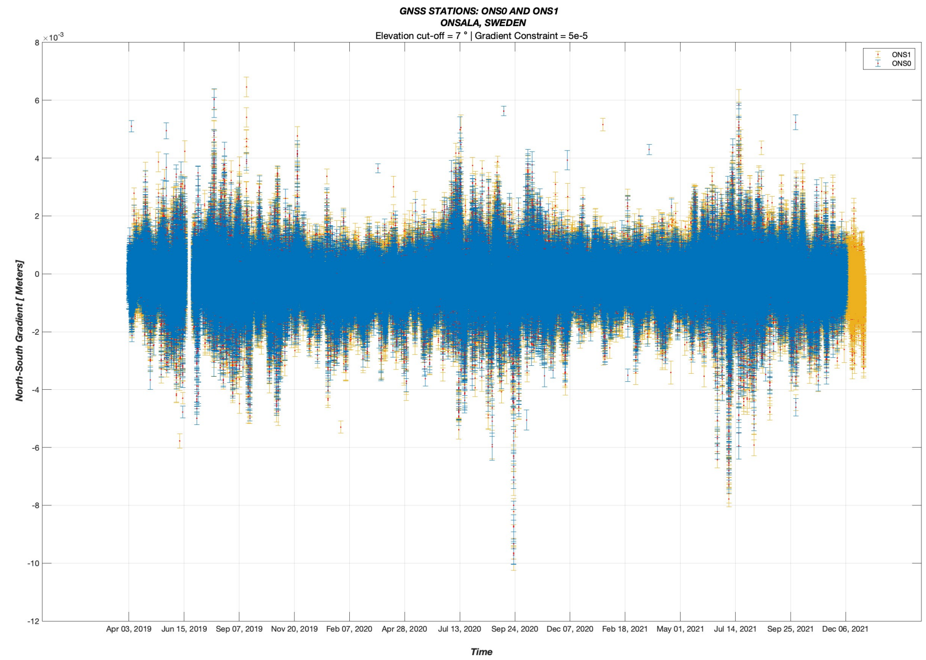

(b) North-South gradient estimated for stations ONS0 and ONS1

Figure B.4: Gradients time series of the East-West gradient B.3a) and North-South gradient (B.3b) estimated for stations ONS0 and ONS1. Gradient constraint: 5e-5, Elevation cut-off: 7°

C

Verification Strategy: The international Stations (GODN, GODE, and GODS, USA)

This section contains additional results for July 29th to the 31st Estimated for the (GOD) international stations.

C.0.1 Zenith Total Delay

Figure C.1: The Time series of the ZTD estimated for the Goddard stations. Gradient constraint: 5e-5, Elevation cut-off: 10°

C.0.2 Tropospheric Gradients

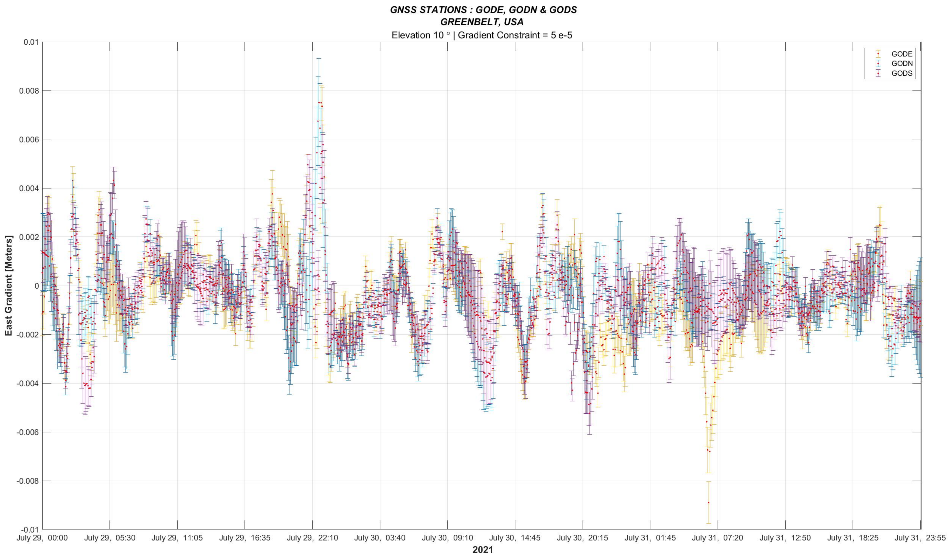

(a) East-West gradient estimated for stations GODN, GODS, and GODE

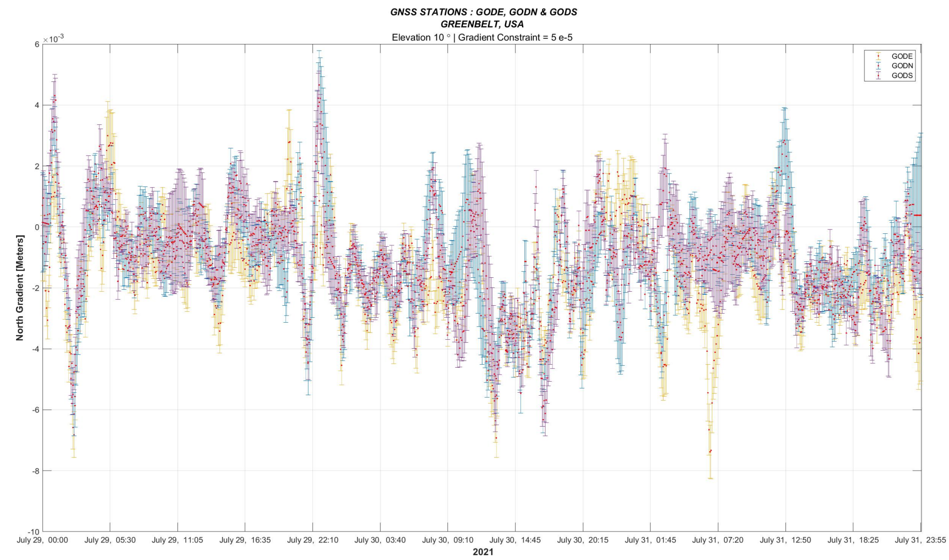

(b) North-South gradient gradient estimated for stations GODN, GODS, and GODE

Figure C.2: Gradients time series of the East-West gradient (C.2a) and North-South gradient (C.2b) estimated for stations GODN, GODS, and GODE. Gradient constraint: 1e-5, Elevation cut-off: 10°

D

Antenna Calibration Techniques: Antenna-Specific vs Model-Specific

This section contains additional results for Febreuary 2nd to the 7th of March Estimated for ONS1, and the OTT stations. In the section only the optimal constraint were used, i.e., 6e-5 and elevation 7°.

D.0.1 Zenith Total Delay

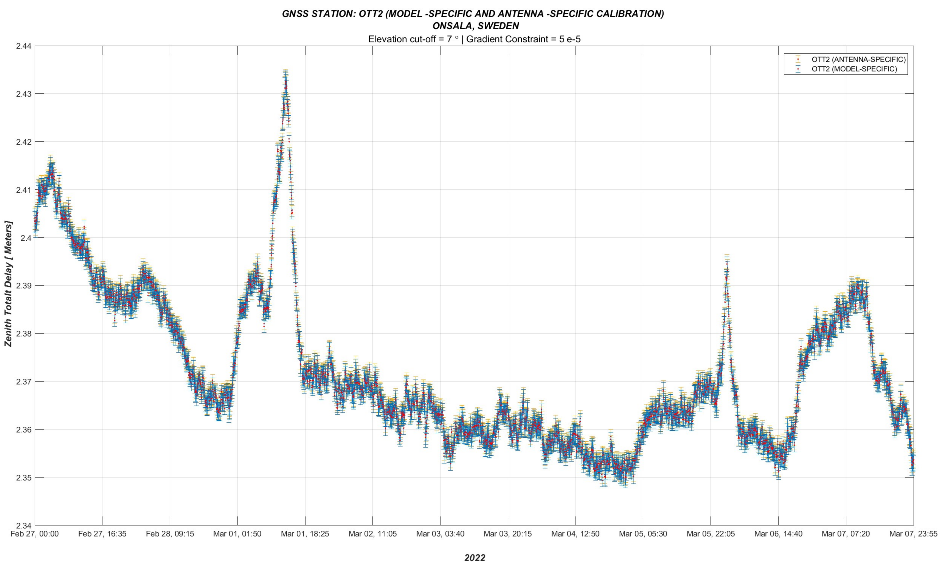

Figure D.1: The time series for the ZTD estimated for station OTT2 using model-specific and antenna-specific calibration techniques

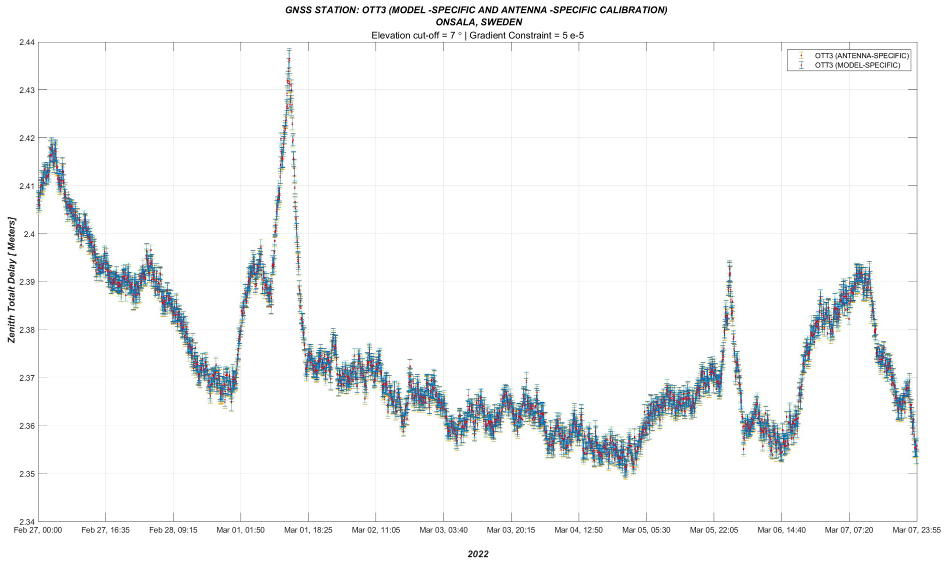

Figure D.2: The time series for the ZTD estimated for station OTT3 using model-specific and antenna-specific calibration techniques

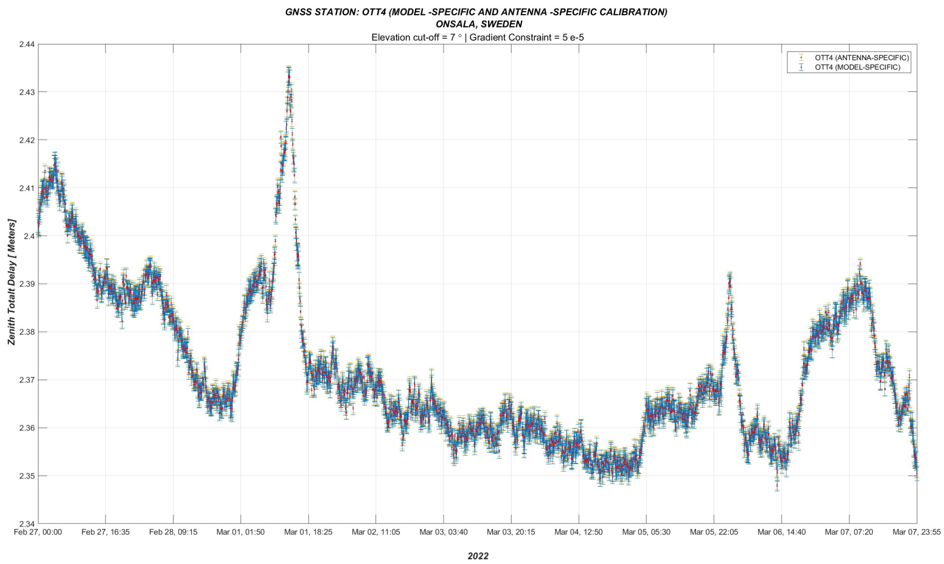

Figure D.3: The time series for the ZTD estimated for station OTT4 using model-specific and antenna-specific calibration techniques

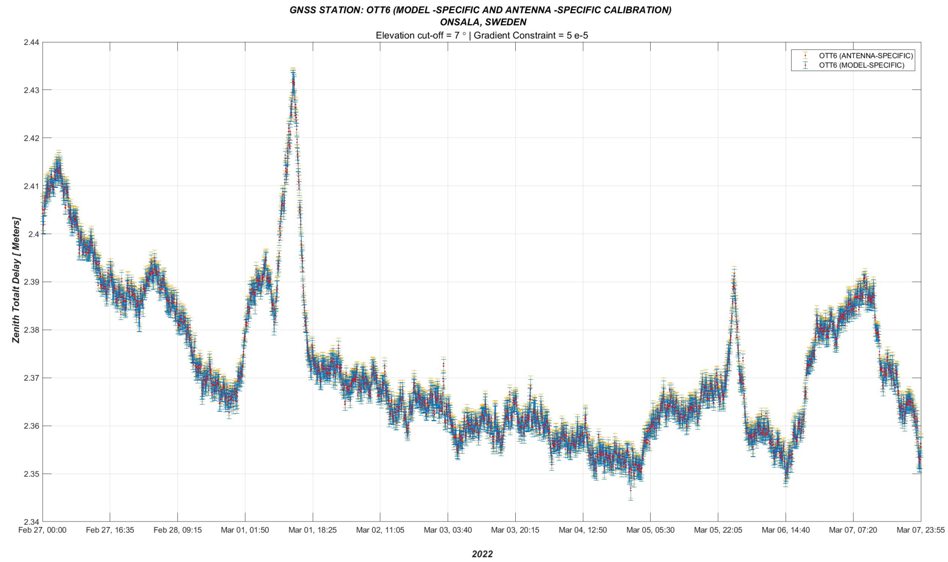

Figure D.4: The time series for the ZTD estimated for station OTT6 using model-specific and antenna-specific calibration techniques

D.0.2 Tropospheric Gradients

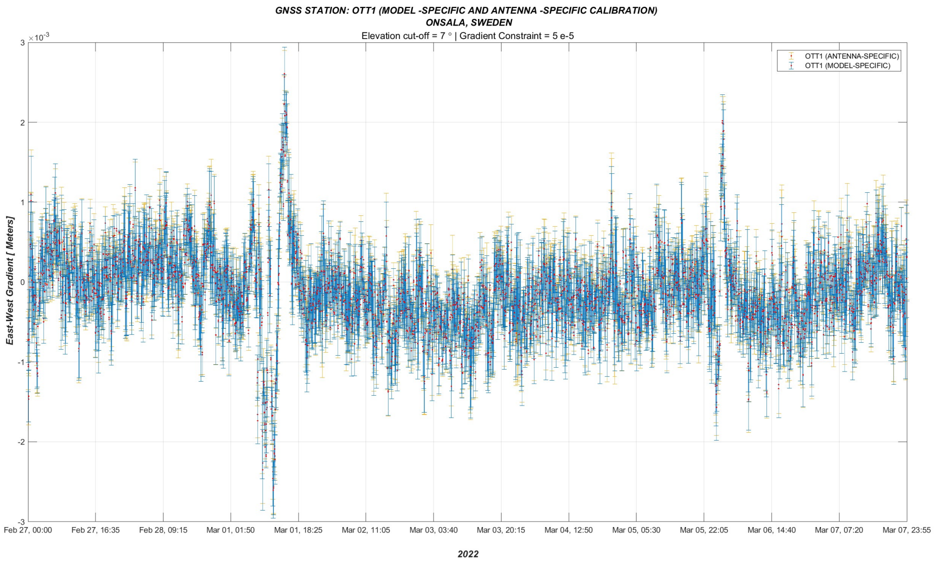

(a) East-West gradient estimated for stations OTT1

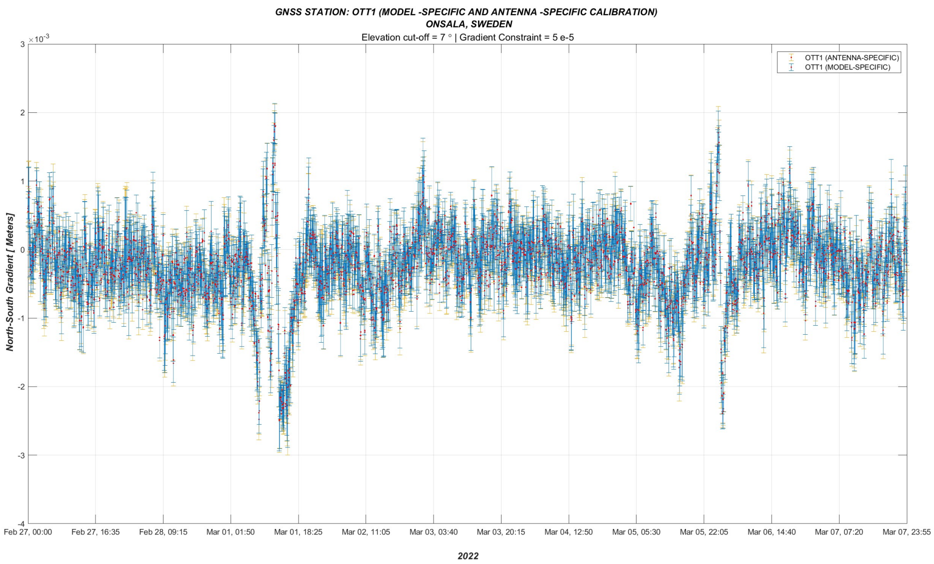

(b) North-South gradient estimated for stations OTT1

Figure D.5: Gradients time series of the East-West gradient (D.5a) and North-South gradient (D.5b) estimated for station OTT1 using model-specific and antenna-specific calibration techniques

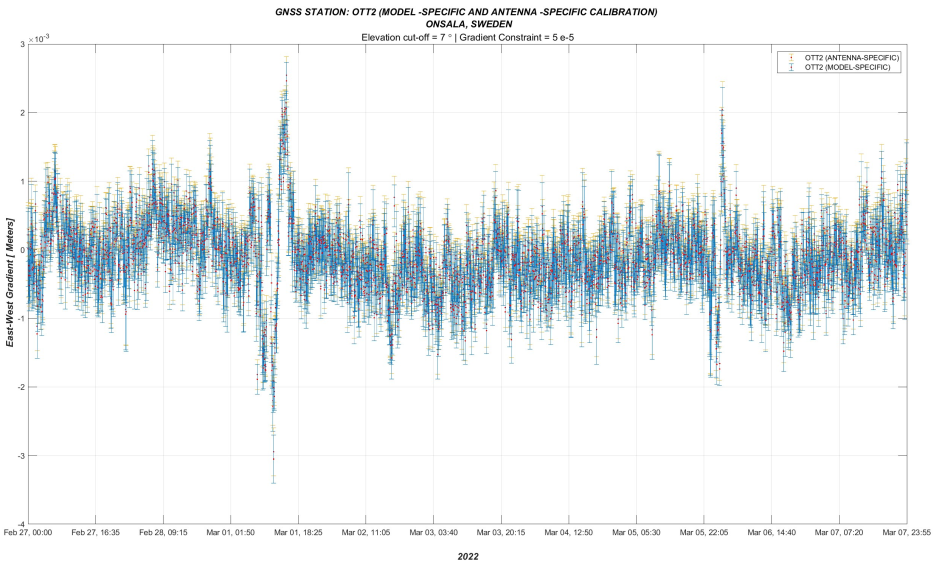

(a) East-West gradient estimated for stations OTT2

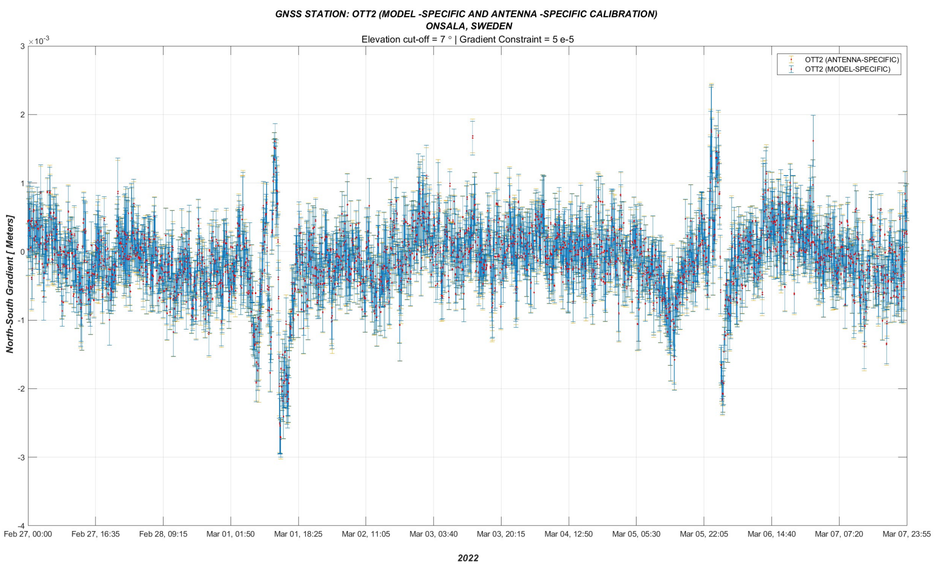

(b) North-South gradient estimated for stations OTT2

Figure D.6: Gradients time series of the East-West gradient (D.6a) and North-South gradient (D.6b) estimated for station OTT2 using model-specific and antenna-specific calibration techniques

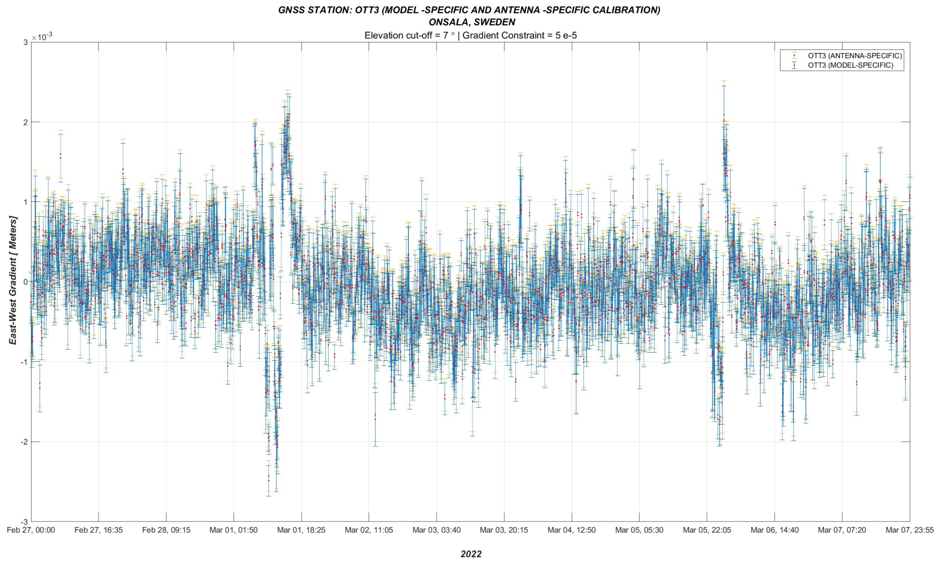

(a) East-West gradient estimated for stations OTT3

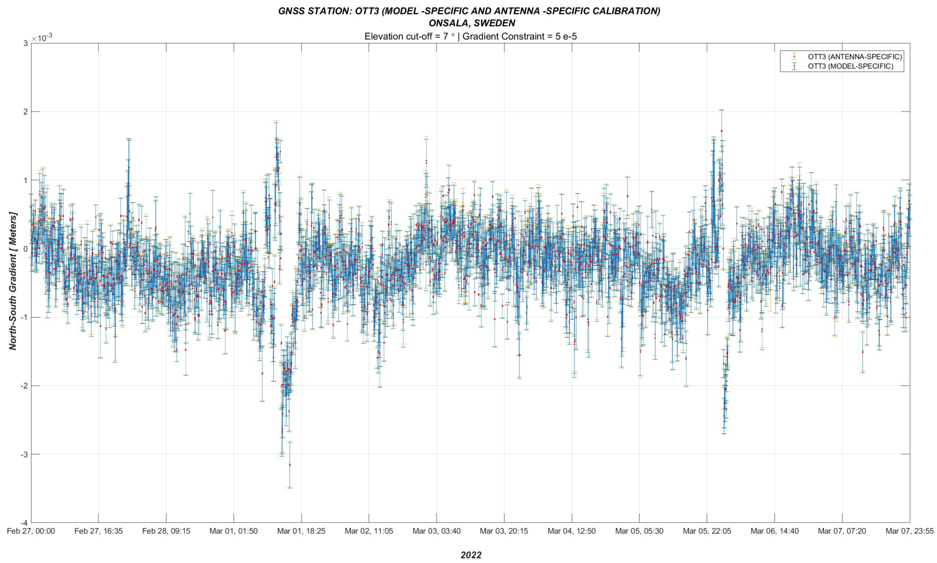

(b) North-South gradient estimated for stations OTT3

Figure D.7: Gradients time series of the East-West gradient (D.7a) and North-South gradient (D.7b) estimated for station OTT3 using model-specific and antenna-specific calibration techniques

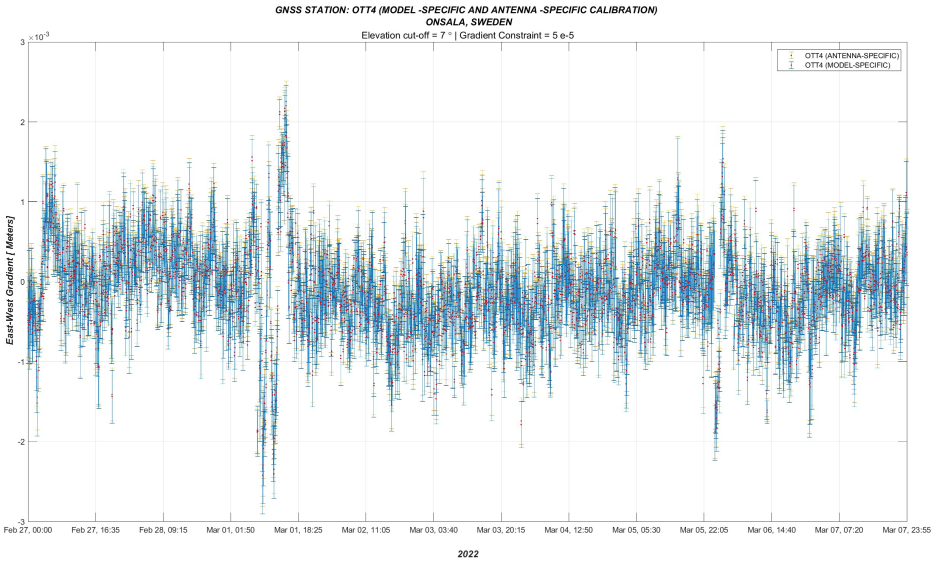

(a) East-West gradient estimated for stations OTT4

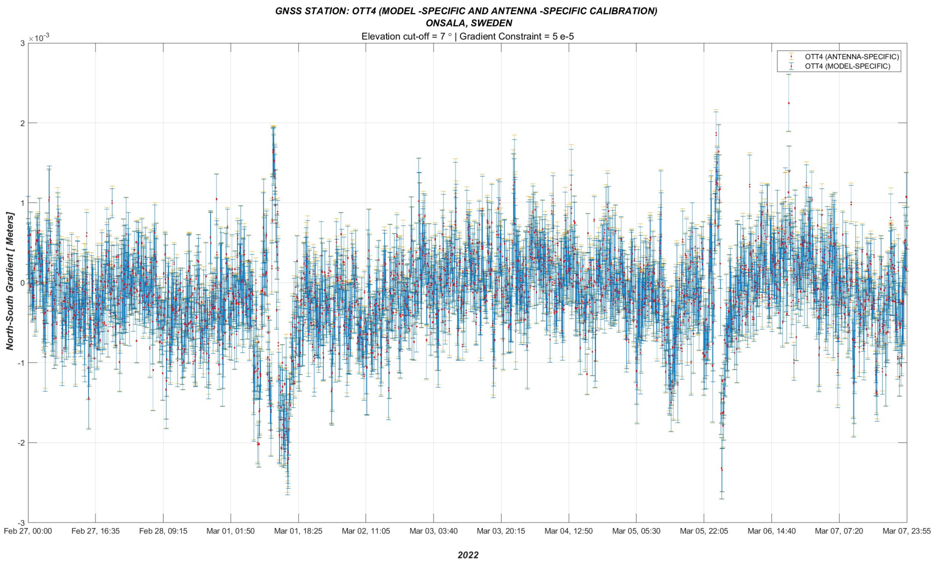

(b) North-South gradient estimated for stations OTT4

Figure D.8: Gradients time series of the East-West gradient (D.8a) and North-South gradient (D.8b) estimated for station OTT4 using model-specific and antenna-specific calibration techniques

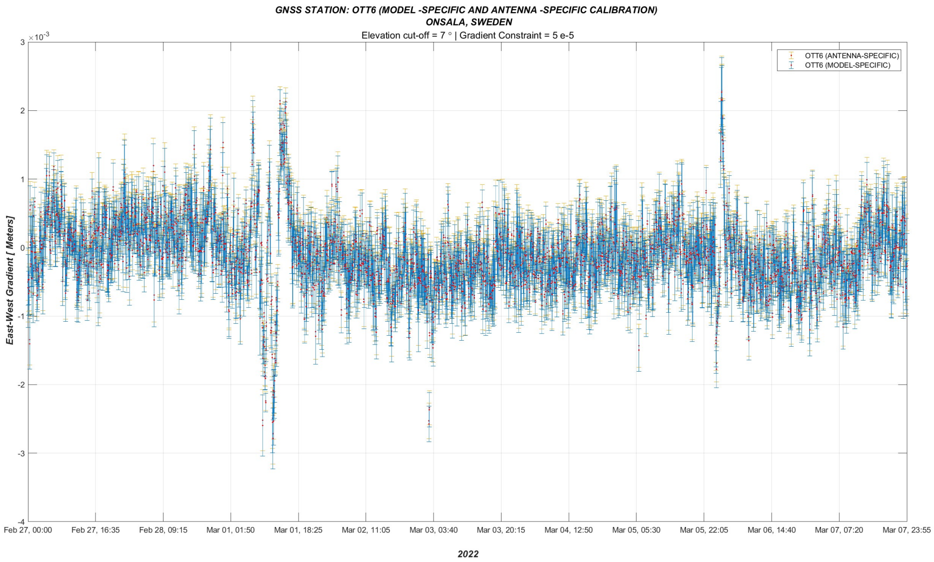

(a) East-West gradient estimated for stations OTT6

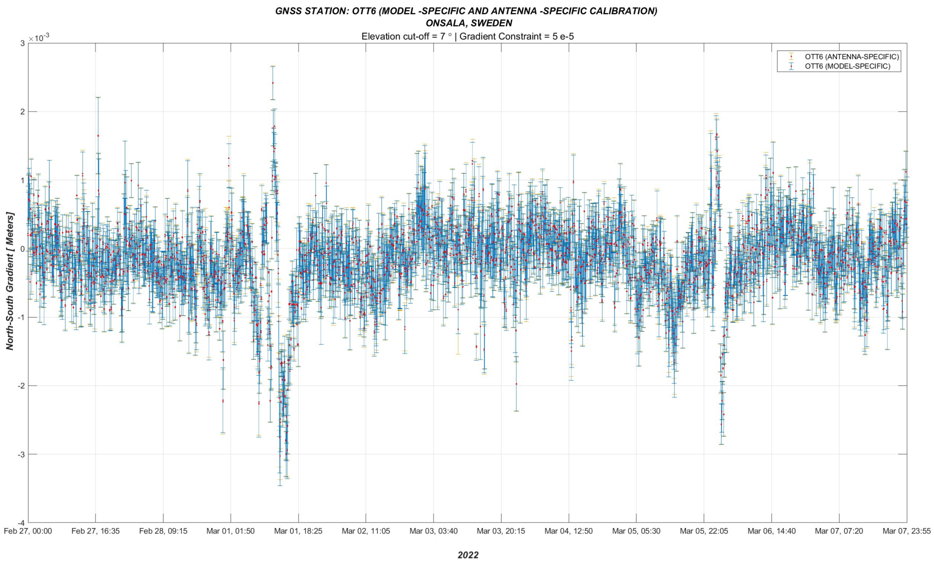

(b) North-South gradient estimated for stations OTT6

Figure D.9: Gradients time series of the East-West gradient (D.9a) and North-South gradient (D.9b) estimated for station OTT6 using model-specific and antenna-specific calibration techniques

E

Receiver-related Error: GRE vs GE

This section contains comparison of the ZTD and gradients estimated on 27 February to 8 March, for ONS0 and ONS1 with the OTT1 station also foor OTT1 station using the GRE combination and the GE constellations. In the section only the optimal constraint were used, i.e., 6e-5 and elevation 7°.

E.0.1 Zenith Total Delay

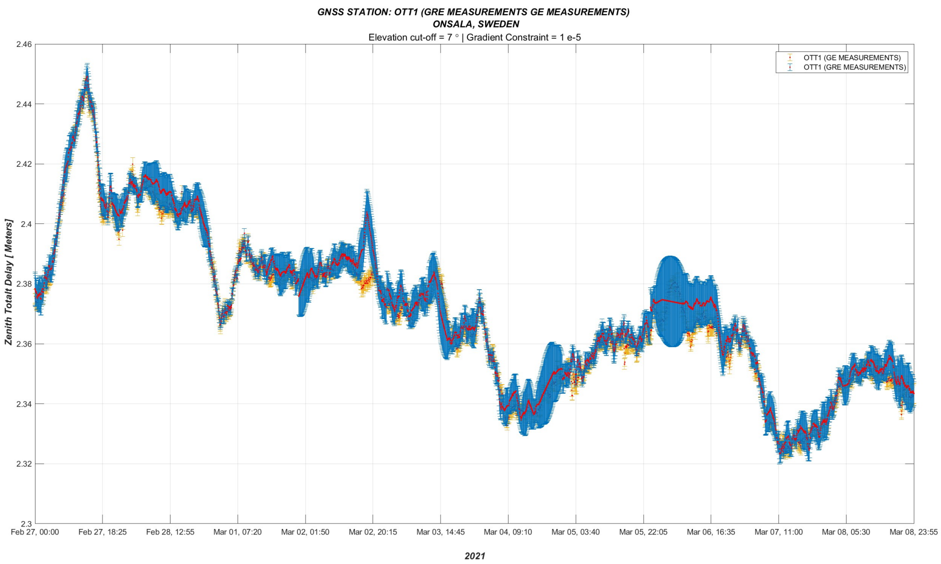

Figure E.1: The time series for the ZTD estimated for station OTT1 using GRE (Yellow) and GE (Blue) GNSS constellations

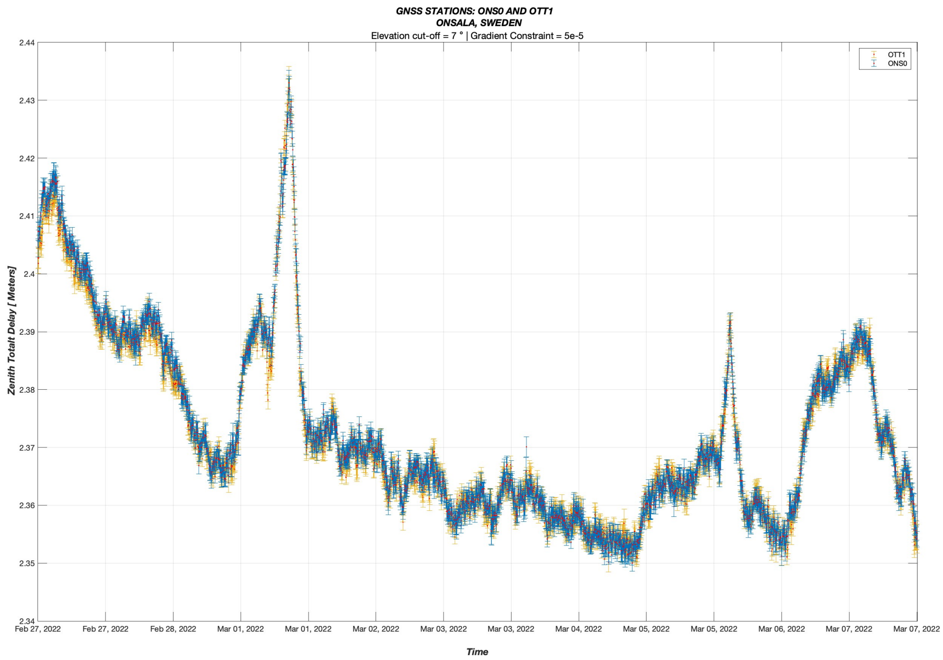

Figure E.2: The time series for the ZTD estimated for stations ONS0 and OTT1 using GRE (after replacing the OTT receivers)

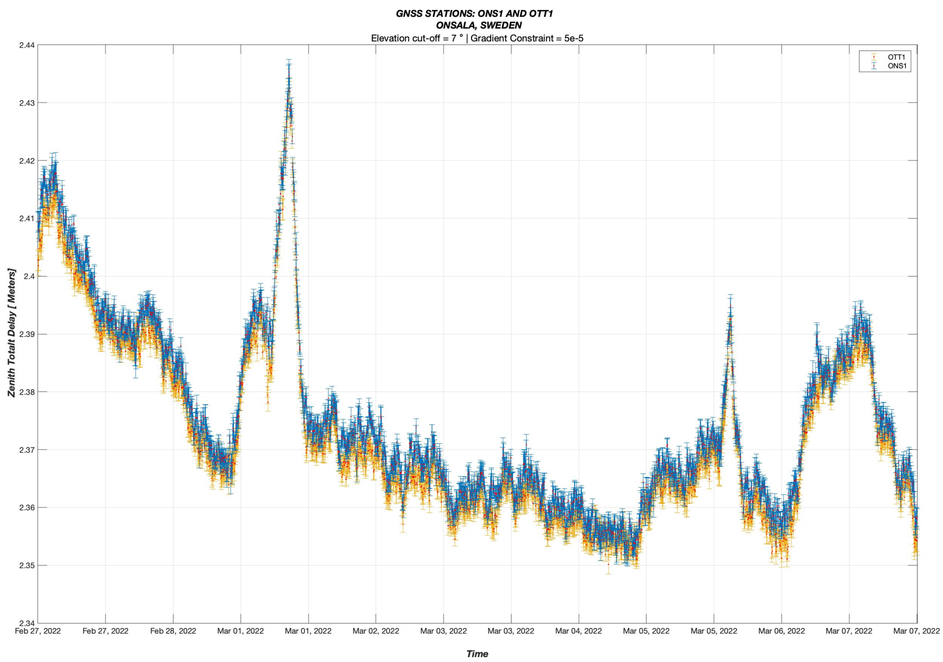

Figure E.3: The time series for the ZTD estimated for stations ONS1 and OTT1 using GRE (after replacing the OTT receivers)

E.0.2 Tropospheric Gradients

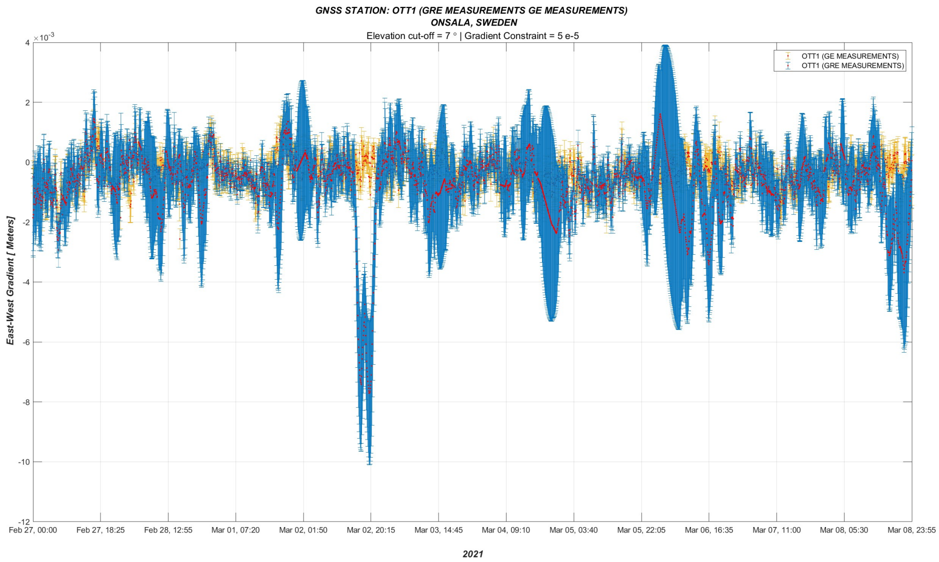

(a) East-West gradient estimated for station OTT1

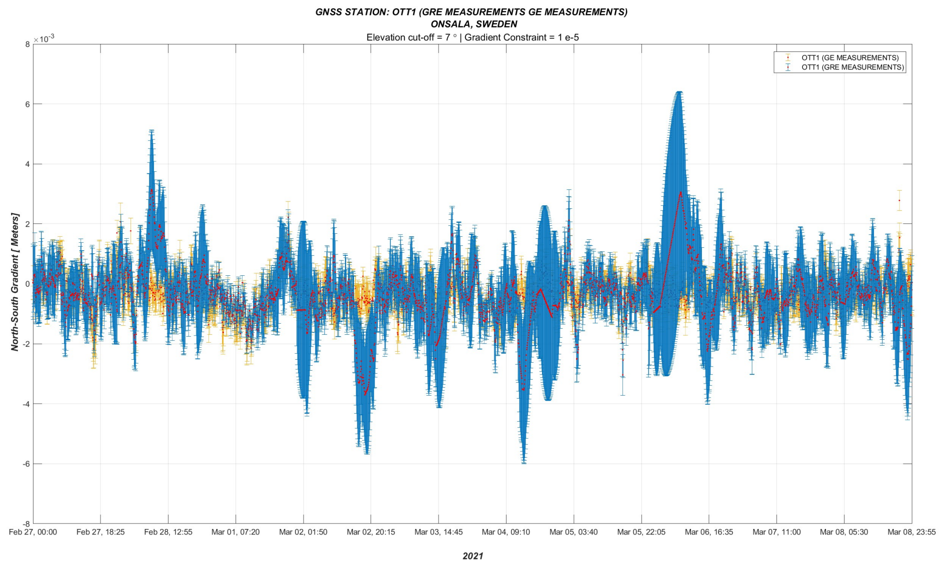

(b) North-South gradient estimated for station OTT1

Figure E.4: Gradients time series for the of the East-West gradient (E.4a) and North-South gradient (E.4b) estimated for station OTT1 using GRE (Yellow) and GE (Blue) GNSS constellations

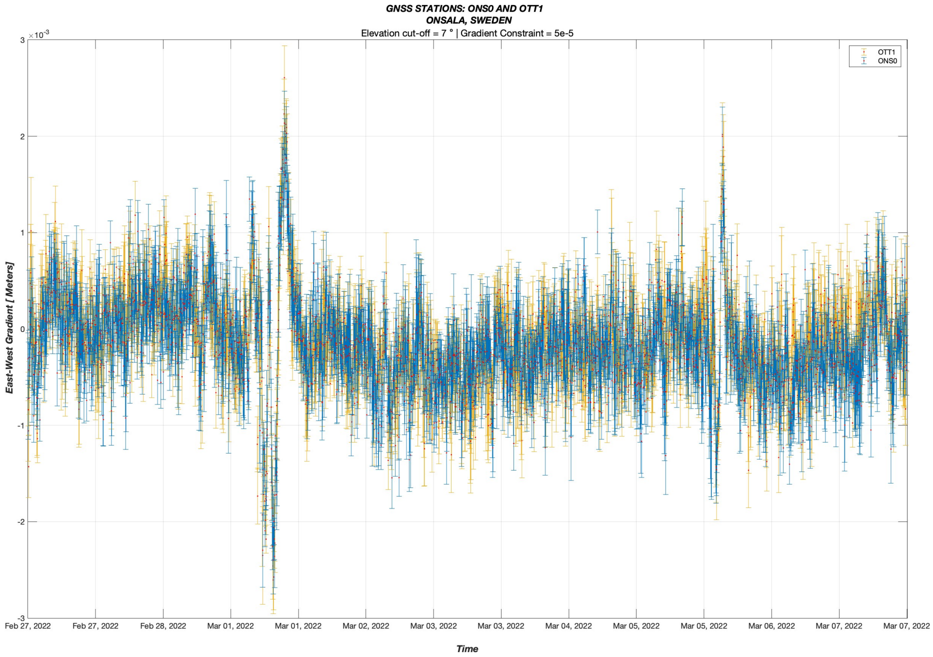

(a) East-West gradient estimated for stations ONS0 and OTT1

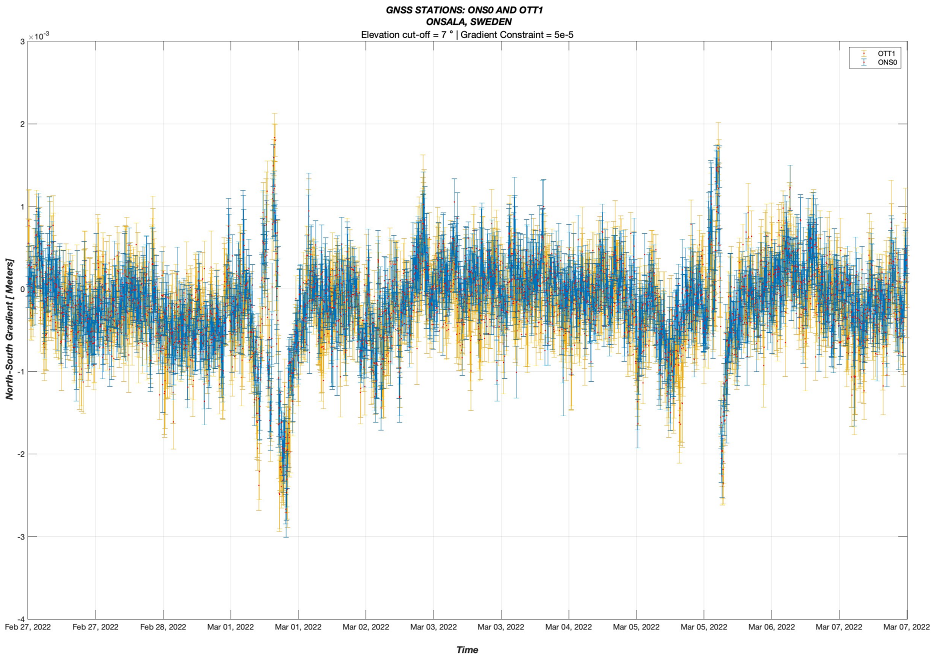

(b) North-South gradient estimated for stations ONS0 and OTT1

Figure E.5: Gradients time series for the of the East-West gradient (E.5a) and North-South gradient (E.5b) estimated for stations ONS0 and OTT1 using GRE (after replacing the OTT receivers)

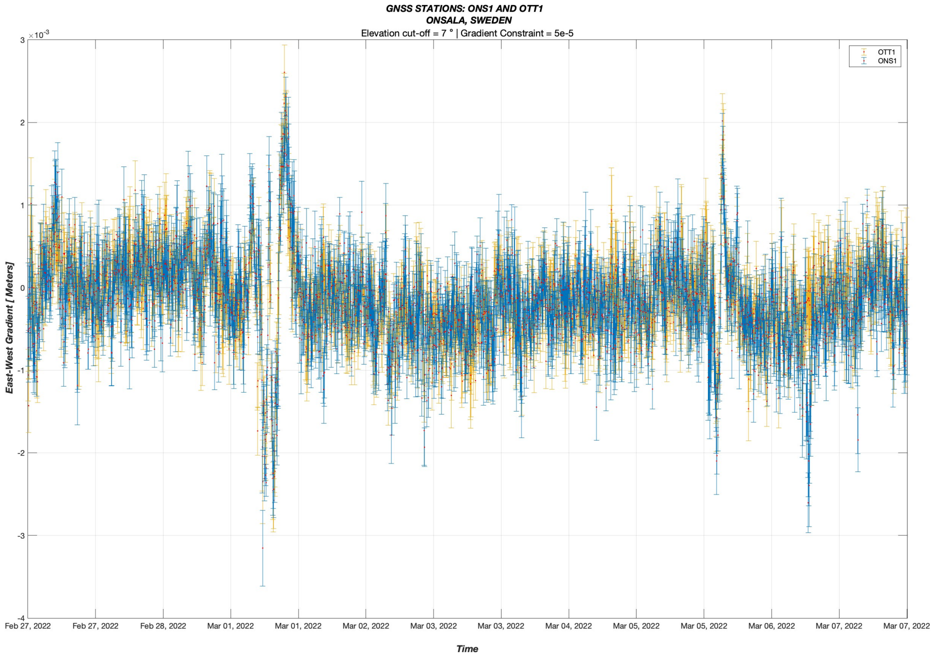

(a) East-West gradient estimated for stations ONS1 and OTT1

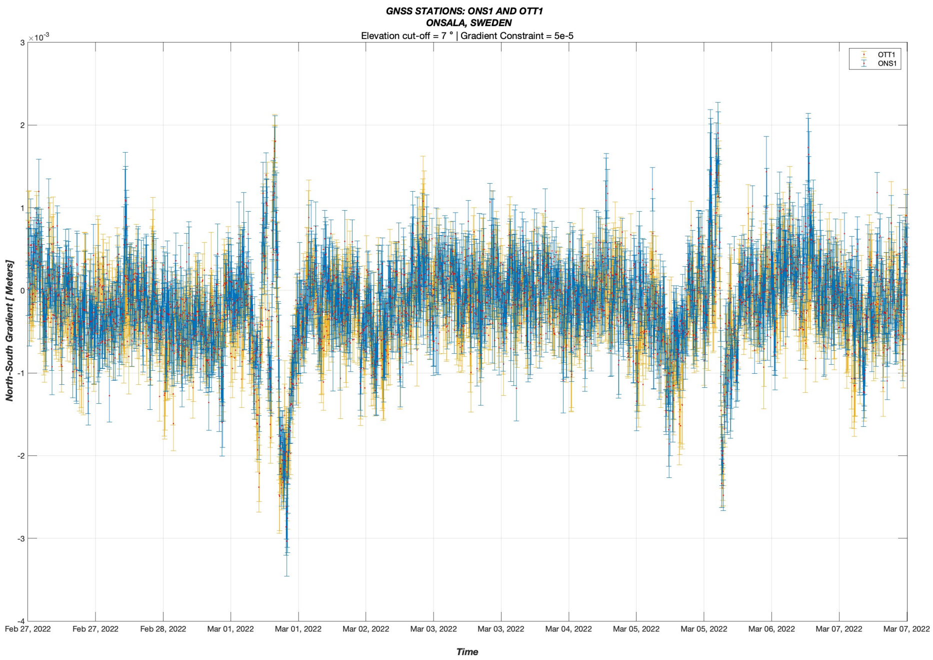

(b) North-South gradient estimated for stations ONS1 and OTT1

Figure E.6: Gradients time series for the of the East-West gradient (E.6a) and North-South gradient (E.6b) estimated for stations ONS0 and OTT1 using GRE (after replacing the OTT receivers)

DEPARTMENT OF SPACE, EARTH AND ENVIRONMENT
CHALMERS UNIVERSITY OF TECHNOLOGY
Gothenburg, Sweden
www.chalmers.se

CHALMERS
UNIVERSITY OF TECHNOLOGY